RETRIEVAL OF STRATOSPHERIC OZONE DENSITY PROFILES FROM OSIRIS SCATTERED SUNLIGHT OBSERVATIONS

Christian von Savigny

A THESIS SUBMITTED TO THE FACULTY OF GRADUATE

STUDIES IN PARTIAL FULFILLMENT OF THE REQUIREMENTS

FOR THE DEGREE OF

DOCTOR OF PHILOSOPHY

GRADUATE PROGRAM IN EARTH AND SPACE SCIENCE

YORK UNIVERSITY

TORONTO, ONTARIO

April 2002

Abstract

A major Canadian contribution to Global Change research involves a novel satellite instrument for monitoring stratospheric ozone concentrations. The instrument, known as OSIRIS (the Optical Spectrograph and InfraRed Imager System), was designed to measure ozone densities using a powerful new technique based on measurements of sunlight scattered by the atmosphere. It is expected that this technique will provide ozone concentration measurements with significant improvements compared to conventional methods. These improvements are urgently required by the international research community in order to explain observed ozone trends and to make reliable predictions for the future. On February 20, 2001, OSIRIS was launched on the Swedish Odin satellite from Svobodny, Russia. This dissertation reports the first global distributions of ozone obtained from the OSIRIS measurements made during the first few months of operation.

The method used to retrieve the ozone densities from the OSIRIS observations follows that of *Flittner et al.* [2000] and *McPeters et al.* [2000]. These authors used this method to analyze limb scattered sunlight observations made in 1997 with the SOLSE/LORE instrument (Shuttle Ozone Limb Sounding Experiment/Limb Ozone Retrieval Experiment) on the NASA space shuttle mission STS-87. The method is based on the analysis of normalized limb radiance profiles measured at

wavelengths in the centre and the wings of the Chappuis-Wulf absorption bands of ozone. As part of this thesis work a non-linear Newtonian iteration version of Optimal Estimation [*Rodgers*, 1976; 1990] has been coupled with the LIMBTRAN multiple scattering radiative transfer model described by *Griffioen and Oikarinen* [2000] in order to analyze the OSIRIS limb radiance measurements.

An extensive set of OSIRIS limb observations was collected during August 2001, when Odin started normal operation and was observing in the northern hemisphere. The analysis of all limb scans that are available for August has yielded stratospheric ozone density profiles that are in excellent agreement with the current knowledge of the global morphology of ozone. The tropospheric ozone column densities have been inferred from the OSIRIS stratospheric ozone densities using a residual approach and the total ozone columns measured by the Total Ozone Mapping Spectrometer (TOMS) on the Earth Probe (EP) satellite. These tropospheric estimates are in reasonable agreement with those derived by *Fishman et al.* [1990]. The OSIRIS ozone density profiles have been partially validated with the POAM III solar occultation measurements made on the SPOT-4 satellite. A total of 43 near coincidences between OSIRIS and POAM III were identified for the period of August 2001. The OSIRIS and the POAM III ozone densities between 15 and 35 km agree to within about 5 % with the OSIRIS ozone densities systematically lower than the POAM densities. The OSIRIS ozone densities have also been compared with ozone densities predicted by the Canadian Middle Atmosphere Model

(CMAM) [*Beagley et al.*, 1997]. The OSIRIS zonally averaged densities are found to be in reasonable agreement with the CMAM predictions. However, the model seems to overestimate the ozone densities at the peak altitude by as much as 20 % and underestimate the densities above 35 km by about 15 %.

At the end of October 2001 OSIRIS was able to make observations in the southern hemisphere in the Antarctic ozone hole region. The first extensive observations of the ozone profile in the ozone hole are presented and it is shown, from November 2001 data, that OSIRIS is capable of accurately monitoring the evolution of the 3-dimensional structure of the Antarctic ozone hole.

It is concluded that satellite based limb scattered sunlight measurements, made with a high-performance spectrometer, when combined with state-of-the-art radiative transfer models, provide a powerful and reliable technique for the remote sensing of stratospheric ozone. The analysis of the OSIRIS observations has shown that global ozone profiles with high accuracy and high vertical resolution (1-2 km) can be obtained using this new technique.

Contents

List of Tables

List of Figures

Acknowledgements

A satellite project always involves the dedicated and continuous effort of many people.
I would like to thank

- Ian McDade for giving me the chance to contribute to a very exciting new satellite project
- Jack McConnell and Wayne Evans for helpful comments
- Gordon Shepherd, without whom I would not have come to York
- Chris Sioris and Craig Haley for many, many fruitful discussions and our joint efforts to make the OSIRIS data analysis work
- Erik Griffioen and Chris McLinden, whose RT models I used extensively
- Brian Solheim and Alain Soltesz for all the help in the incomprehensible jungles of our computers
- The OSIRIS team, particularly Ted Llewellyn, Doug Degenstein and Nick Lloyd. Without their hard work on the instrument this study would not have been possible
- Jean de Grandpré for making CMAM ozone fields available
- Emilio Cuevas from the Izaña station (Tenerife) and Peter van der Gathen as well as Andreas Herber from the Alfred Wegener Institut for providing ozone sonde data
- David Flittner for very helpful comments

- NASA for the accessibility of EP-TOMS and POAM III data
- All the merry inhabitants of Petrie for three enjoyable years at York
- Dave, Sébastien and Ana-Luisa for reading this thesis
- Special thanks also to Brian. B., Neil D., W. E., Kyle's mum, and Caroline

Chapter 1

Introduction

Ozone is an atmospheric trace constituent of great importance. It has played a major role in the evolution of life on earth, since it protects biological organisms from harmful solar UV radiation that has the potential of damaging organic macromolecules vital for life. Evolution of life on land is thought to have become possible only because of ozone formation caused by the release of molecular oxygen produced by cyanobacteria (blue-green algae) through oxygenic photosynthesis [*Warneck*, 1988; *Wayne*, 1991].

Ozone also has important implications for the vertical structure of the Earth's atmosphere. The absorption of solar radiation by ozone, leading to its dissociation, causes a peak in the atmospheric temperature profile at about 50 km - defining the stratopause - and the stratosphere's stable stratification.

Ozone is one of the most extensively studied and best understood atmospheric

trace constituents and has thus played an important role in the development of atmospheric chemistry. Atmospheric ozone has been the object of scientific inquiry for over 150 years, starting with Schönbein's notion of some atmospheric constituent with a peculiar odour[1] [*Schönbein*, 1840]. Houzeau proved the existence of ozone in 1858 using chemical methods. The next important milestone was Hartley's realization that absorption of solar radiation by ozone may be responsible for the sharp cutoff in the transmitted solar spectrum at about 300 nm [*Hartley*, 1881]. *Strutt*[2] [1918] concluded from long-path transmission experiments employing a mercury line at 253.7 nm, that the bulk of the atmospheric ozone cannot be located at the Earth surface, but must occur higher up in the atmosphere. In the early nineteen twenties Dobson began to measure the column amount of atmospheric ozone, starting the famous *Arosa* time series, a continuous record of ozone column densities over Arosa (Switzerland) [e.g., *Dobson*, 1968] from 1926 to-date. Only a few years later the first photochemical model explaining the existence and the shape of the stratospheric ozone layer was proposed by Chapman in 1930. With the advent of absorption spectrometers aboard Earth orbiting satellites (particularly SBUV[3] and TOMS[4]) enabling scientists to infer global maps of different

[1] ozein: *Greek*, to smell

[2] the fourth Lord Rayleigh, also known as "airglow Rayleigh".

[3] Solar Backscatter Ultraviolet Spectrometer on Nimbus 7 (11/1978 - 1990), NOAA-9, NOAA-11, and NOAA-14 (1984 - present) [*Heath et al.*, 1975]

[4] Total Ozone Mapping Spectrometer on Nimbus 7 (11/1978 - 05/1993), Meteor 3 (08/1991 - 11/1994), and Earth-Probe (07/1996 - present) [*Heath et al.*, 1975]

minor constituents including ozone on a daily basis, our knowledge has greatly improved in terms of the global morphology of ozone, its dependence on latitude and season and its interaction with other chemical compounds, particularly those containing halogens.

Ozone has also been a spectacular example of the unpredictability of the consequences of human behaviour when the ozone destruction potential of chloroflourocarbons (CFCs) became obvious with the discoveries of *Molina and Rowland* [1974].

Partly because of the availability of replacement products for CFCs, an international agreement on the ban of ozone depleting compounds was reached in 1989 with the "Montreal Protocol on Substances that Deplete the Ozone Layer" [*UNEP*, 2000], and has been adjusted and/or amended in London (1990), Copenhagen (1992), Vienna (1995), Montreal (1997) and Beijing (1999). The Protocol regulates the phase out of production and trade of CFCs, Halons, halogenated CFCs and other halogen compounds for the parties of the protocol. The urgency of the ozone problem was dramatically emphasized by the discovery of the Antarctic ozone hole by *Farman et al.* [1985] and subsequent confirmation with TOMS observations [*Stolarski et al.*, 1986], which made the true extent of the phenomenon apparent.

Satellite-based remote sensing experiments to study the chemical composition of the atmosphere have traditionally been of two types: (a) nadir viewing spec-

trometers (TOMS, GOME[5]) capable of producing global maps of the total ozone column on a daily basis, but they provide either no information on the vertical ozone profile, or vertical profiles with poor vertical resolution (7 - 10 km) [e.g., *Hasekamp and Landgraf*, 2001; *Hoogen et al.*, 1999]; (b) solar Occultation experiments, e.g. HALOE[6], POAM[7], and SAGE[8] yielding vertical ozone density profiles with better vertical resolution (about 2 km), but suffer from poor geographical coverage, since the occultation condition has to be met. For typical satellite orbit parameters only about 15 sunset and 15 sunrise occultation measurements can be obtained with a solar occultation experiment per day.

A new technique, i.e. limb scatter of sunlight, that combines the advantages of the other techniques, provides vertical profiles of ozone density with (near) global coverage on a daily basis. One of the instruments applying this technique is the Canadian Optical Spectrograph and InfraRed Imager System (OSIRIS) [*Llewellyn et al.*, 1997; *Warshaw et al.*, 1996] aboard the Swedish-led Odin satellite that has been orbiting the Earth since February 2001. The optical part of OSIRIS consists of a grating spectrometer and the nodding of the satellite enables OSIRIS to scan the Earth's limb. Other instruments also capable of limb scanning or limb imaging

[5]Global Ozone Monitoring Experiment on ERS-2 (04/1995 - present) [*Burrows et al.*, 1999]

[6]HALogen Occultation Experiment aboard UARS (09/1991 - present) [*Russell et al.*, 1993]

[7]Polar Ozone and Aerosol Measurement on Spot-3 (POAM II, 09/1993 - 11/1996) and on Spot-4 (POAM III, 03/1998 - present) [*Lucke et al*, 1999]

[8]Stratospheric Aerosols and Gas Experiment on ERBS (SAGE II, 10/84 - present) and Meteor 3M (SAGE III, launch 12/2001)

are SCIAMACHY[9] and GOMOS[10]. The limb scatter technique has already been successfully applied to limb radiance profiles measured by the LORE/SOLSE[11] instruments flown on NASA's space shuttle mission STS-87 in 1997 and yielded ozone profiles that agreed to within 10% with ozonesondes [*Flittner at al.*, 2000; *McPeters et al.* 2000].

It must be mentioned that the limb scatter technique has been discussed since the early 1970s [*Cunnold et al.*, 1973], and has already been applied by *Rusch et al.* [1984] to retrieve ozone in the mesosphere, and by *Mount et al.* [1984] to retrieve NO_2 in the upper stratosphere.

The present dissertation describes the application of a method to recover vertical profiles of ozone density from spectra of limb scattered sunlight obtained with OSIRIS.

1.1 Structure of the thesis

The structure of the thesis is as follows. An overview of the most important characteristics of the stratospheric ozone layer and its chemistry is given in Chapter 2. Chapter 3 gives a detailed description of the OSIRIS instrument, providing all the

[9]SCanning Imaging SpectroMeter for Atmospheric CHartographY aboard ENVISAT-1, launched on March 1, 2002 [*Bovensmann et al.*, 1999]

[10]Global Ozone Measurement by Occultation of Stars aboard ENVISAT-1 [*Bertaux et al.*, 1991]

[11]Limb Ozone Retrieval Experiment/Shuttle Ozone Limb Sounding Experiment

information necessary for ozone density profile recoveries. The method applied in the present study to infer vertical ozone profiles from OSIRIS observations of limb radiance spectra is described in Chapter 4. Since the limb radiance profiles employed depend not only on the ozone density profile, but also on several geophysical and instrumental parameters including, *e.g.*, ground albedo, clouds, stratospheric aerosols and the polarization of the detected radiation, a comprehensive sensitivity study has been carried out to establish the systematic uncertainties introduced into the recovered ozone density profiles if some of those factors are unknown or not known with sufficient accuracy. The results of this sensitivity study are presented in Chapter 5.

Chapter 6 presents a comparison of OSIRIS ozone density profiles with ozone profiles measured with the POAM III occultation instrument. Over 40 spatio-temporal coincidences were identified during August 2001. The analysis of OSIRIS observations in the northern hemisphere (NH) during August 2001 and in the southern hemisphere (SH) during November 2001 is described in Chapter 7. It is shown that the NH ozone densities derived from OSIRIS limb scans are in excellent agreement with the known characteristics of the global morphology of ozone. Moreover, OSIRIS is capable of monitoring the evolution of the 3-D structure of the Antarctic ozone hole. This Chapter also includes a comparison of stratospheric ozone columns derived from OSIRIS observations with total ozone columns measured with EP-TOMS (Earth Probe TOMS). Furthermore, in Chapter 8 the

zonally and temporally averaged northern hemisphere ozone density field for August 2001 as retrieved from OSIRIS data is compared to the 10 year mean ozone density field for August determined with the Canadian Middle Atmosphere Model (CMAM). Chapter 9 presents the major conclusions and gives an outlook on possible future work and improvements.

Chapter 2

Stratospheric ozone

The first section (2.1) of this Chapter is an overview of the most important aspects of stratospheric ozone chemistry, i.e. the *Chapman mechanism* and the *catalytic ozone destruction cycles.* Section 2.2 presents a brief introduction to the main characteristics of the global morphology of stratospheric ozone. It is demonstrated in Chapter 7 that all of the principal features of the global distribution of ozone are easily identified in the OSIRIS data set. Finally, section 2.3 describes the absorption spectrum of ozone.

2.1 Overview of stratospheric chemistry

2.1.1 The Chapman cycle

Chapman [1930] proposed that the photodissociation of molecular oxygen was responsible for the formation of O_3. His theory stated that atomic oxygen is formed by photolysis of O_2

$$O_2 + h\nu \longrightarrow O + O \qquad (\lambda < 242nm) \tag{2.1}$$

The highly reactive oxygen atoms recombine with O_2 to form O_3

$$O_2 + O + M \longrightarrow O_3 + M \tag{2.2}$$

with N_2 or O_2 as the third body M required for the simultaneous conservation of energy and momentum. O_3 is photolyzed by

$$O_3 + h\nu \longrightarrow O_2 + O \tag{2.3}$$

with the resulting atomic oxygen most likely being in the electronically excited $O(^1D)$ state for $\lambda < 310$ nm [*Wayne*, 1987]. For 310 nm $< \lambda <$ 1100 nm the oxygen atom is in its ground state $O(^3P)$. Since the O atoms have a very short lifetime[1], O_3 is reformed very quickly, and reaction 2.3 cannot be considered a loss mechanism for O_3. Chapman proposed that the loss mechanism for "odd oxygen"

[1]The lifetime of O is about 1 s at 40 km, and about 10^{-2} s at 20 km

(O_x) , *i.e.* O and O_3, is

$$O_3 + O \longrightarrow O_2 + O_2 \tag{2.4}$$

Although the Chapman cycle was an important step towards a better understanding of stratospheric ozone chemistry, it is incomplete for several reasons: (a) if it were correct the ozone columns should be the highest in the tropics, where SZAs (solar zenith angles) are small, whereas they assume a maximum at moderate to high latitudes; (b) the Chapman cycle leads to predictions of ozone densities that are a factor of 2 higher than observed densities in the tropics[2]; and (c) at polar latitudes the predictions of the Chapman model are too low. Those inconsistencies disappear if additional odd oxygen loss mechanisms, i.e. catalytic ozone destruction cycles involving halogen, hydrogen and nitrogen compounds, as well as the Brewer-Dobson circulation, a slow stratospheric equator-to-pole motion, are considered.

2.1.2 Catalytic gas phase reactions

Stratospheric chemistry and particularly the chemistry of catalytic ozone destruction cycles, has become a complex field involving a great number of chemical species and both gas phase and heterogeneous reactions. A complete description of these processes is beyond the scope of the present thesis, and only the most important

[2]Chapman's model produces a globally averaged total ozone column of 790 DU [*Newman*, 2000], whereas the actual total column is about 300 DU

reactions are described. A more detailed description is given by *Wayne* [1991].

The catalytic cycles can be summarized schematically in the following way

$$X + O_3 \longrightarrow XO + O_2 \tag{2.5}$$

$$XO + O_{2n+1} \longrightarrow X + (n+1)O_2 \tag{2.6}$$

$$\text{net} \qquad O_3 + O_{2n+1} \longrightarrow (n+2)O_2 \tag{2.7}$$

with X = H, OH, NO, Cl, belonging to the three families HO_x, NO_x and ClO_x, and $n = 0, 1$. The importance of the HO_x family on stratospheric ozone was already established in the 1960s, whereas the NO_x cycle was established in the early seventies by *Crutzen* [1971] and *Johnston* [1971].

Only a few years later *Stolarski and Cicerone* [1974] proposed the existence of another catalytic cycle involving the ClO_x family in the context of HCl released by solid rocket boosters used for Shuttle launches. *Molina and Rowland* [1974] suggested that photolysis of CFCs in the stratosphere could be a significant source of stratospheric ClO_x.

According to *Wayne* [1991], the catalytic HO_x cycle is the most important single odd oxygen loss mechanism above about 45 km. At around 45 km the ClO_x cycle is the most important single odd oxygen loss mechanism, and below 40 km catalytic ozone destruction by NO_x dominates. Note that the fractional contribution of the Chapman reaction O + O_3 to the total odd oxygen loss rate is less than 20 % at all altitudes.

It is important to realize that the schematic reactions 2.5 - 2.7 present a simplified picture of the actually more complex stratospheric chemistry. Even within individual families, reaction chains occur that do not fit within the above scheme, but catalytically destroy ozone. For example,

$$OH + O \longrightarrow H + O_2 \tag{2.8}$$

$$H + O_2 + M \longrightarrow HO_2 + M \tag{2.9}$$

$$HO_2 + O \longrightarrow OH + O_2 \tag{2.10}$$

$$\text{net} \quad O + O + M \longrightarrow O_2 + M \tag{2.11}$$

i.e., destroying O_x. This cycle is of importance above 40 km. Furthermore, the catalytic families also interact, therefore the total effect of all families is not identical to the sum of the effects of individual families. For example, calculations with ClO_x, or $HO_x + ClO_x$ alone lead to more O_3 destruction than in the case including NO_x. This is due to the following reactions

$$HO_2 + NO \longrightarrow OH + NO_2 \tag{2.12}$$

$$ClO + NO \longrightarrow Cl + NO_2 \tag{2.13}$$

which produce NO_2 which may be considered an odd oxygen source due to

$$NO_2 + h\nu \longrightarrow NO + O \tag{2.14}$$

Apart from reactions between the three catalytic families there are also *null cycles* and *holding cycles* competing with the catalytic ozone destruction cycles.

Null cycles interconvert X and XO without loss of O_x, e.g.

$$NO + O_3 \longrightarrow NO_2 + O_2 \tag{2.15}$$

$$NO_2 + h\nu \longrightarrow NO + O \tag{2.16}$$

$$\text{net} \quad O_3 + h\nu \longrightarrow O_2 + O \tag{2.17}$$

The net effect of this cycle corresponds to the photolysis of ozone, without loss of O_x. Holding cycles, on the other hand, involve the production of an unreactive *reservoir* compound from reactive members of the family. These cycles lead to a reduction of "active" material. They can involve more than one catalytic family, e.g. the formation of nitric acid

$$OH + NO_2 + M \longrightarrow HONO_2 + M \tag{2.18}$$

Subsequently, $HONO_2$ is photolyzed and OH and NO_2 are released again. Nitric acid contains more than half of the stratospheric NO_x load. In terms of the ClO_x family the most important reservoir species is HCl, representing about 70 % of the stratospheric ClO_x.

All the reactive families (NO_y[3], Cl_y, H_2O, and Br_y) involved in the catalytic ozone destruction cycles have their origin in the troposphere and were also present in the preindustrial atmosphere, yet at lower concentrations. The precursor species

[3] NO_y or "odd nitrogen" includes NO_x, N_2O_5, HNO_3, HNO_4, $ClONO_2$ and other nitrogen compounds. It is the sum of NO_x and all oxidized nitrogen species that act as sources and sinks of NO_x on relatively short time scales. Similar definitions apply to ClO_y, and BrO_y.

enter the stratosphere mainly through the tropical tropopause where they are brought by the upward branch of the tropical Hadley cell. The main net sources of OH radicals in the stratosphere are reactions of electronically excited $O(^1D)$ with H_2O and CH_4; the first reaction yielding 2 OH and the latter OH and CH_3. Stratospheric NO_x (*i.e.*, NO and NO_2) is predominantly produced from nitrous oxide (N_2O) via reaction with $O(^1D)$. The only natural precursor of ClO_y is thought to be CH_3Cl (methyl chloride). The sink mechanism for the catalytic families involves transport of the reservoir species across the tropopause into the troposphere, where they are thought to dissolve in water and are consequently rained out.

For more information on the stratospheric chemical reactions involving the HO_x, NO_x and ClO_x families see appendix B.

2.2 Global distribution of stratospheric ozone

2.2.1 The vertical profile of ozone

The vertical ozone density profile exhibits a maximum in the lower stratosphere, and the altitude of the ozone density peak as well as the maximum density are dependent on geographic latitude and season. The shape of the stratospheric ozone layer (*i.e.* a Chapman layer [*e.g.*, *Wayne*, 1991]) can be well described with the Chapman mechanism already described in section 2.1. The ozone density peak in the tropics is higher in altitude compared to mid- and high-latitudes, a consequence

of the higher tropical tropopause. Typical tropical ozone density peak altitudes are about 27 km. When going from tropical to higher latitudes the ozone density peak descends, most significantly within the stratospheric surf zone, broadens and assumes an altitude of about 20 km at polar latitudes. Fig. 2.1 shows the latitudinal dependence of zonally averaged ozone density profiles, retrieved from OSIRIS limb scans. The data set consists of all ozone density profiles retrieved from OSIRIS observations carried out during August 2001 (about 3900 profiles in total). The latitudinal variation of both the ozone peak altitude and peak density in Fig. 2.1 is in excellent agreement with the current knowledge of the global morphology of ozone. The retrieval algorithm and its error budget is discussed in detail in subsequent Chapters.

Tropical ozone profiles are generally smoother than profiles at higher latitudes where ozone laminae occur frequently. A statistical analysis of northern hemisphere ozone data [*Dobson*, 1973] showed that laminated structures in the ozone layer occur most frequently in spring for latitudes greater than 30°N, when the poleward transport associated with the Brewer-Dobson circulation is the strongest.

Generally, the peak densities are greatest at low latitudes and decrease with increasing latitude, yet the total ozone column increases with increasing latitude (for latitudes up to about 60°). The latitudinal dependence of both the ozone peak altitude and the total ozone column can be explained through the Brewer-Dobson circulation, first proposed by Brewer (1949)[4] and Dobson (1953). The

[4]Brewer suggested rising air in the tropics as an explanation for the low water vapor con-

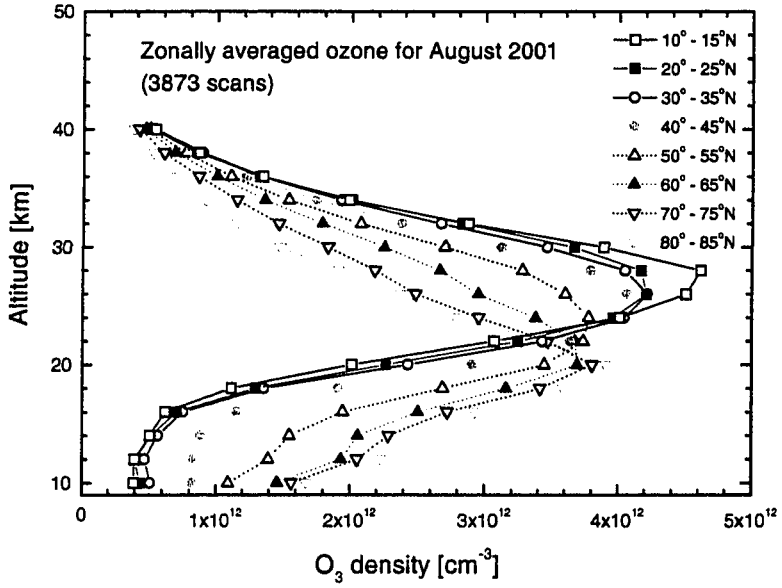

Figure 2.1: The latitudinal dependence of the August 2001 mean zonally averaged ozone density profiles as retrieved from OSIRIS limb spectra observations. The retrieval method is described in subsequent Chapters.

Brewer-Dobson circulation qualitatively corresponds to rising motion in the tropics, followed by poleward transport, leading to a reduction of ozone densities at low latitudes. At high latitudes, sinking motion lowers the altitude of the ozone peak and leads to an accumulation of ozone, in agreement with higher total ozone columns at higher latitudes. The Brewer-Dobson circulation is most efficient in the winter hemisphere, whereas meridional transport in the summer stratosphere is weakened partly by stable and strong easterly winds [e.g., *Roedel*, 1992].

centrations in the stratosphere. Vertical motion causes dehydration due to condensation and precipitation of water, *i.e.* water vapor is essentially "freeze dried" out.

2.2.2 The global distribution of the total ozone column

Fig. 2.2 shows a contour plot of the annual variation of zonally averaged total ozone columns from April 1970 to June 1972 (*i.e.* pre-ozone hole conditions) as measured with the Backscatter Ultraviolet Spectrometer (BUV) on board the Nimbus 4 spacecraft. Apparent are low ozone columns at tropical latitudes with values between 250 and 270 Dobson Units[5] (DU). Furthermore, the annual variation of ozone columns is relatively small at tropical latitudes. In contrast, high northern and southern latitudes experience a significant annual variation of the total ozone columns with maxima occurring in spring (i.e., April in the northern hemisphere and October in the southern hemisphere), with maximum columns typically being larger in the northern hemisphere. It is important to note that the Antarctic ozone hole, occurring from August until the end of November since the early 80s, leads to systematically lower total ozone columns at southern hemisphere polar latitudes during austral spring, yet there is still a local maximum in the so-called "collar" regions around 50-60°S. The collar is formed by poleward moving air-masses carrying ozone from the tropical source region. Due to the stable polar vortex further poleward meridional transport is prevented leading to an accumulation of ozone.

The general picture of increasing ozone columns with increasing latitude can

[5]One DU corresponds to an O_3 column of 10^{-2} mm under standard conditions (*i.e.*, 1013.25 hPa and 0° C). Thus, typical vertical O_3 columns of about 300 DU correspond to a total O_3 column of 3 mm under standard conditions.

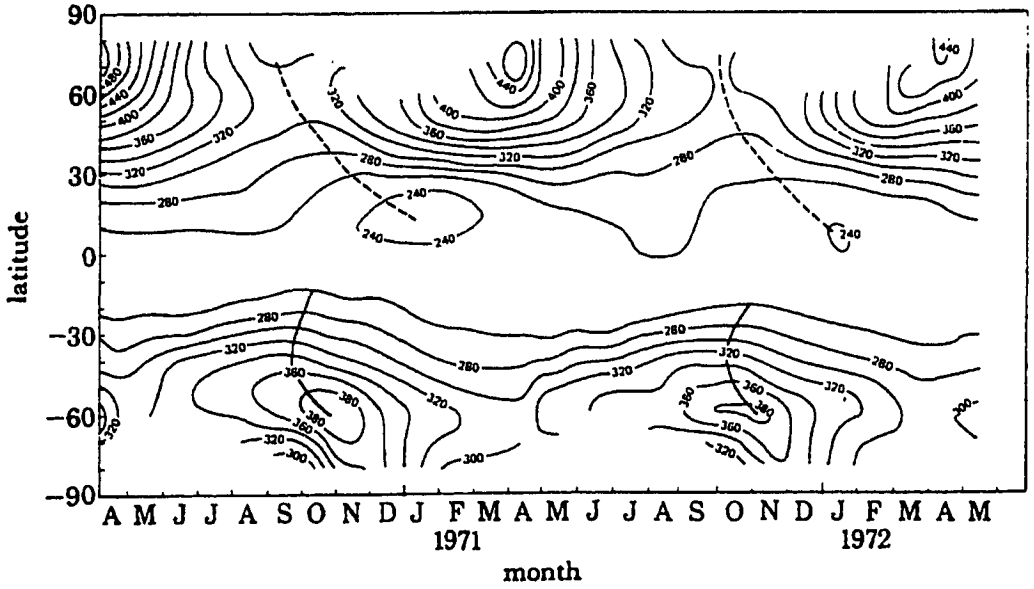

Figure 2.2: The annual variation of the global ozone column field as observed with BUV on Nimbus 4. Low latitudes exhibit little annual variability, whereas high northern latitudes show the typical spring maximum.

again be qualitatively explained by the Brewer-Dobson circulation. The Brewer-Dobson circulation, strongest during winter and spring in each hemisphere is also responsible for the appearance of the spring-time maximum.

It is noteworthy that the tropospheric ozone column corresponds to 10-15% of the total atmospheric ozone column. Only a few percent of the total column resides in the mesosphere.

2.2.3 The Antarctic ozone hole

The Antarctic ozone hole corresponds to a temporally and spatially limited event of significant reductions of the total ozone column over the Antarctic continent dur-

ing austral spring. Starting in late August, the temporal ozone depletion reaches its maximum in October, and disappears entirely by the end of November. Dramatic losses of total ozone over Antarctica were first observed in the early 80s, when *Farman et al.* [1985] published the first paper on the sudden formation of what is now called the "ozone hole", observed with a ground-based Dobson spectrophotometer operated by the British Antarctic Survey at Halley Bay (76° S, 27° W). *Stolarski et al.* [1986] subsequently analyzed TOMS data of the vertical ozone column in the southern hemisphere and found that the sudden ozone depletion in southern spring extends over most of the Antarctic continent, and is centered over the south pole.

Different theories were invoked to explain the sudden stratospheric ozone loss over Antarctica, some of them being of dynamical nature and some of chemical nature. The Nitrogen Oxide Theory, proposed by *Callis and Natarajan* [1986], hypothesized that huge amounts of NO_x were produced as a consequence of the solar maximum in 1979. Enhanced NO_x would be photochemically produced by increased intensities of solar UV radiation. NO_x would then catalytically destroy O_3 through $NO + O_3 \Longrightarrow NO_2 + O_2$ and $NO_2 + O \Longrightarrow NO + O_2$ yielding a net reaction $O_3 + O \Longrightarrow 2O_2$. Yet observations reported by *Farmer et al.* [1976] and *Coffey and Mankin* [1989] indicate low NO_2 densities at high latitudes during the ozone hole event.

The generally accepted theory now involves heterogeneous reactions occur-

ring on the surface of PSCs (polar stratospheric clouds, *i.e.* particles consisting of ternary mixtures of nitric acid, sulphuric acid and water) that convert reservoir compounds to catalytically active species or their precursors. The formation of PSCs requires extremely low temperatures (below 195 K) that occur more frequently in the Antarctic polar stratosphere than in the Arctic polar stratosphere.

Of particular importance in this context is chlorine that is usually stored in the reservoir compounds HCl and $ClONO_2$ (see also appendix B). Those two reservoir species can react with each other on the surface of PSCs through

$$ClONO_2 + HCl \longrightarrow Cl_2 + HNO_3 \tag{2.19}$$

whereby chlorine is released as a gas. Once solar photons reach the polar stratosphere in the southern hemisphere spring, molecular chlorine is photolyzed

$$Cl_2 + h\nu \longrightarrow Cl + Cl \tag{2.20}$$

to chlorine atoms. Due to the low atomic oxygen concentrations when the sun first reaches the polar stratosphere the rapid ozone destruction cannot be explained by the catalytic cycle described by reactions 2.5 - 2.7. Of principal importance in this context is thought to be the catalytic cycle involving ClO but not oxygen atoms:

$$ClO + ClO + M \longrightarrow (ClO)_2 + M \tag{2.21}$$

$$(ClO)_2 + h\nu \longrightarrow Cl + ClOO \tag{2.22}$$

$$ClOO + M \longrightarrow Cl + O_2 + M \tag{2.23}$$

$$2(Cl + O_3 \longrightarrow ClO + O_2) \tag{2.24}$$

$$\text{net} \quad 2O_3 + h\nu \longrightarrow 3O_2 \tag{2.25}$$

Also important is the bromine - chlorine synergism via the reactions

$$BrO + ClO \longrightarrow Br + Cl + O_2 \tag{2.26}$$

$$Br + O_3 \longrightarrow BrO + O_2 \tag{2.27}$$

$$Cl + O_3 \longrightarrow ClO + O_2 \tag{2.28}$$

$$\text{net} \quad O_3 + O_3 \longrightarrow O_2 + O_2 + O_2 \tag{2.29}$$

2.3 Absorption cross section of Ozone

The absorption spectrum of ozone in the UV to NIR (near infrared) spectral region is divided into four different absorption bands. The smooth Hartley bands extend from about 200 to approximately 310 nm, followed by the more structured Huggins bands, ranging from about 310 nm to 360 nm. The visible part of the spectrum is covered by the Chappuis bands between 400 and 650 nm which partly overlap with the Wulf bands, ranging from about 600 nm to 1100 nm.

Fig. 2.3 shows the ozone absorption cross section between 240 and 800 nm for temperatures ranging from 202 K to 293 K as measured in the laboratory with the GOME FM (Flight model) [*Burrows et al.*, 1997]. The spectral resolution of the GOME FM is wavelength dependent and ranges from 0.2 nm to 0.4 nm.

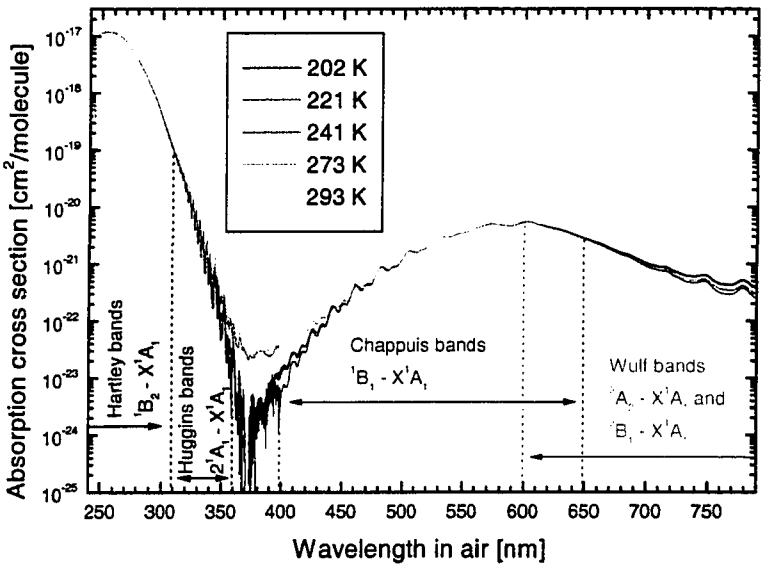

Figure 2.3: The absorption cross section of ozone for different temperatures as measured with the GOME Flight Model [*Burrows et al.*, 1997].

Apparently the Hartley as well as the Chappuis bands are rather insensitive to temperature, an advantage when ozone absorption structures in those bands are employed for absorption spectroscopy and remote sensing. The Huggins bands, on the other hand, exhibit significant variation with changing temperatures, and the temperature sensitivity increases with increasing wavelength. Also, the Wulf bands are more temperature sensitive than the Chappuis bands.

The molecular transitions associated with the absorption bands of ozone are still somewhat unknown. According to *Wayne* [1987] the Hartley bands are probably caused by the $^1B_2 \leftarrow X^1A_1$ transition. The Huggins bands may be due to the $2^1A_1 \leftarrow X^1A_1$ transition. The Chappuis bands are probably caused by the

$^1B_1 \leftarrow X^1A_1$ and the Wulf bands seems to be almost exclusively caused by the $(^3A_2 \leftarrow X^1A_1)$ and $(^3B_1 \leftarrow X^1A_1)$ transitions [*Wayne*, 1987].

Chapter 3

The OSIRIS Instrument on the Odin Satellite

3.1 The Odin satellite

OSIRIS, the Optical Spectrograph and InfraRed Imager System is one of two instruments on board the Swedish/Canadian/Finish/French Odin satellite. The second instrument is a Submillimeter and Millimeter Radiometer (SMR) designed for both astronomy and aeronomy studies. Odin was launched on February 20, 2001 from Svobodny (about 128°E, 51°N) in eastern Siberia with a Russian Start-1 (converted SS-25) InterContinental Ballistic Missile (ICBM) into a near-terminator sun-synchronous orbit with ascending/descending nodes at 18:00/6:00 LST (Local Solar Time), respectively. See Fig. 3.1 for a depiction of the launch vehicle and the

launch.

Odin is a relatively small satellite with a total mass of 235 kg, and a total energy consumption of 260 Watts. The satellite's overall height is about 2 m, its width is 1.1 m, and 3.8 m when solar panels are deployed. A picture of Odin in the laboratory during the mass property tests in Toulouse in May 2000 is shown in Fig. 3.2

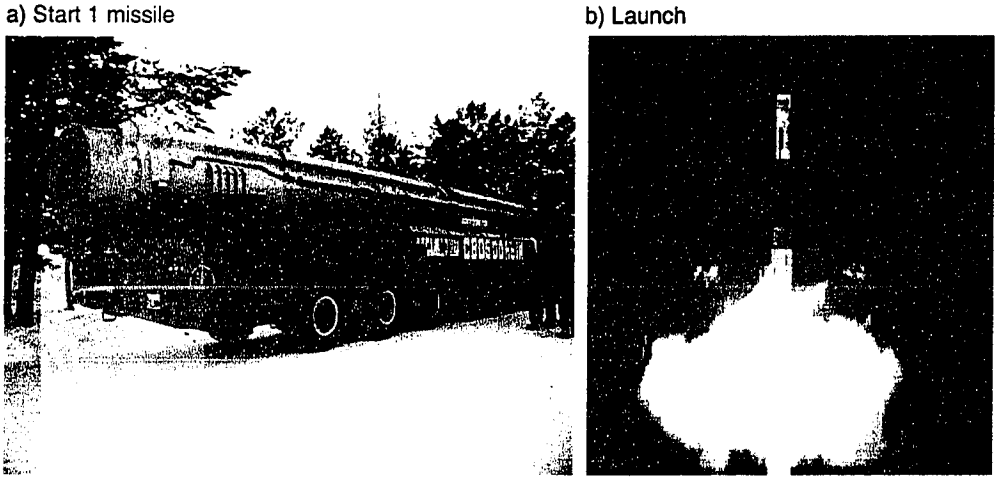

Figure 3.1: The mobile launcher carrying the Start-1 missile and the launch on February 20, 2001 from the Cosmodrome at Svobodny.

The nominal viewing direction of OSIRIS and SMR in aeronomy mode is in the orbit plane, but it can be directed anywhere between $\pm$ 32.0° out of plane. Odin's

period is 96 minutes, and the satellite will cross a certain latitude circle always at the same LST, while the longitude will change by 24° between two consecutive orbits. The inclination of Odin's orbit is 97.8° leading to a precession period of 365 days, and limiting the maximum latitudinal coverage of OSIRIS from 82.2°N to 82.2°S when viewing is in the orbit plane. The geographical coverage is of course further limited, since limb spectra can only be taken with the Optical Spectrograph on the sunlit side of the Earth.

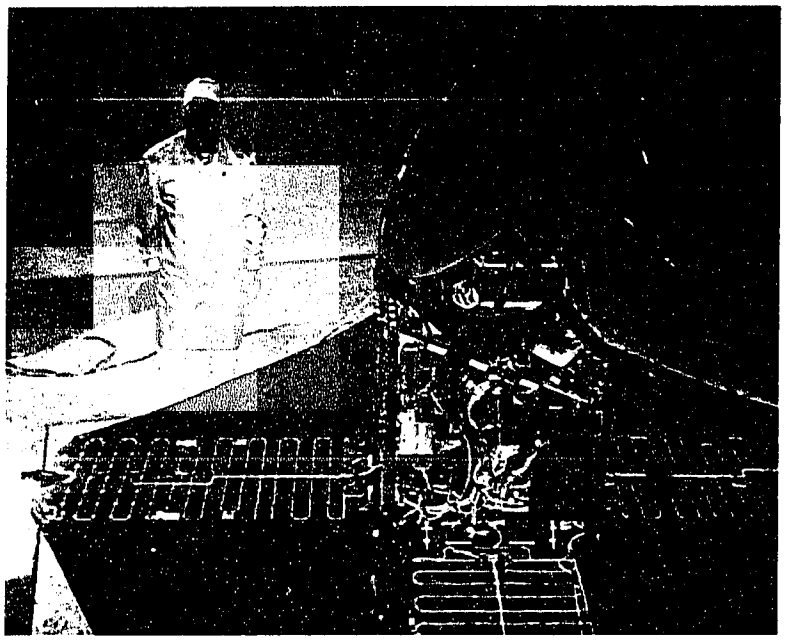

Figure 3.2: Odin with solar panels deployed and covers removed. OSIRIS is located in the right back corner of the spacecraft, below the SMR antenna.

Unlike other satellite based scanning spectrometers (*e.g.*, GOME, TOMS) OSIRIS does not have a movable mirror to perform the limb scanning. Rather the entire satellite nods continuously. This enables OSIRIS and SMR to scan the

Earth's limb within tangent height (TH) ranges of nominally 7 to 70 km in stratospheric mode, 7 to 100 km in strato-mesospheric mode and 70 to 110 km in mesospheric mode. The limb observation geometry and important parameters (*e.g.*, solar zenith angle (SZA) and change in azimuth angle ($\Delta\phi$)) are illustrated in Fig. 3.3. Due to the near terminator orbit and the fact that OSIRIS and SMR are looking in the flight direction, the scattering angles associated with the OSIRIS viewing geometry fall within the range $\theta \in [57.8°, 121.3°]$.

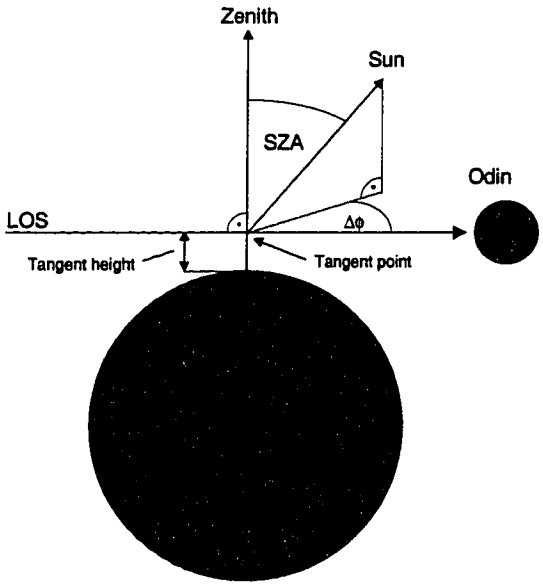

Figure 3.3: Illustration of the limb observation geometry (LOS: Line of Sight, SZA: Solar Zenith Angle).

The Odin orbit parameters have important implications for the geographical coverage achievable with OSIRIS (see Fig. 3.4). On the terminator days, *i.e.* October 12, and February 28, Odin flies along the terminator and the SZA, $\Delta\phi$ and the

scattering angle theoretically are all 90° throughout the orbit (panel b) in Fig. 3.4). Between October 12 and February 28 only the southern hemispheric part of the tangent point's trajectory is sunlit, and observations in the northern hemisphere are not possible with the optical spectrograph (panel c) in Fig. 3.4).

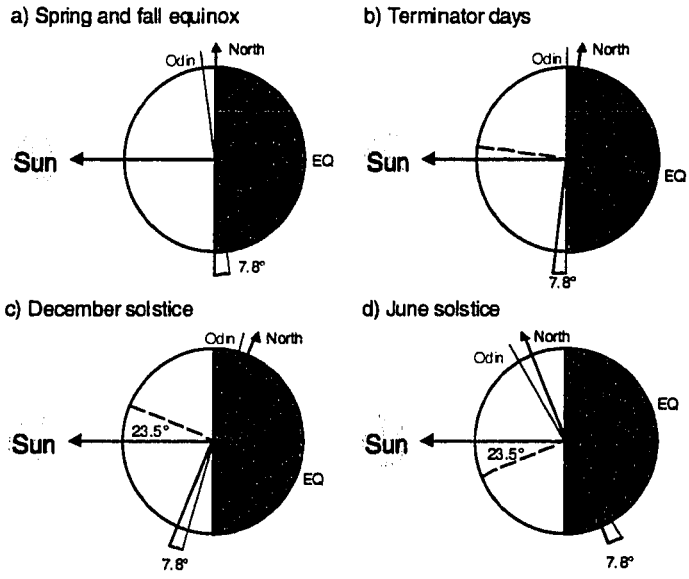

Figure 3.4: The orientation of Odin's orbit throughout the year (adapted from *Infante* [2001]).

Between February 28 and October 12 observations can be performed in the northern hemisphere only, since the southern hemispheric part of the tangent point trajectory is in darkness. This period includes the NH (northern hemisphere) spring and fall equinoxes as well as the NH summer solstice (panels a and d) in Fig. 3.4). A disadvantage of Odin's orbit is that the Antarctic ozone hole region cannot be observed before October 12, which leaves only approximately 6 weeks of observa-

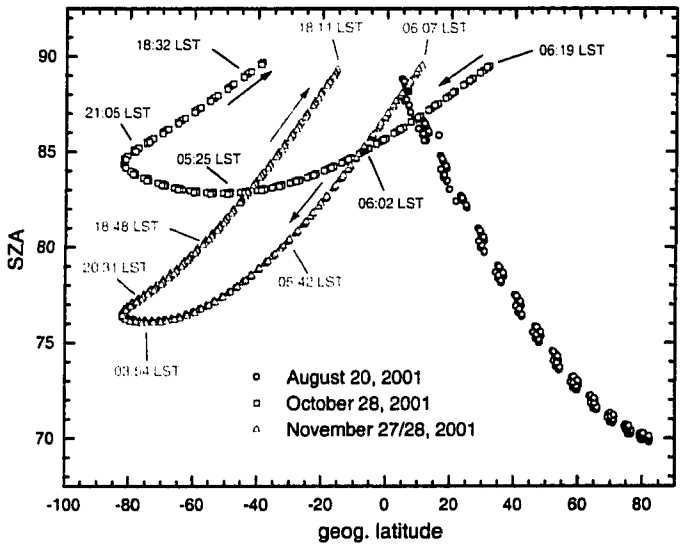

Figure 3.5: The dependence of the tangent point SZA on latitude for three days in summer and autumn 2001. Also indicated are the local solar times (LST) of some scans.

tion before the break-up of the polar vortex which usually occurs at the end of November. Fig. 3.5 shows the SZA variation as a function of geographic latitude for three selected days in summer and fall of 2001. Apparently, there are small deviations from an exact sun-synchronous orbit. On August 20, 2001, the SZAs for the up-leg and down-leg scans are almost equal for a certain latitude, indicative of equator crossing times of close to 6:00 and 18:00 LST. This is not the case on the other two days. Apart from slightly altering the geographical coverage, these deviations do not have negative consequences for the aeronomy mission.

3.2 The Optical Spectrograph

A detailed and comprehensive description of the Optical Spectrograph and the Infrared Imager has been given by *Warshaw et al.* [1996], therefore, only a brief summary is presented here. The Optical Spectrograph is a grating spectrograph covering the spectral range between 280 and 800 nm with a resolution of about 1 nm. The infrared imager consists of three channels, two of which have filters designed to select the O_2 infrared atmospheric band ($a^1\Delta_g \leftarrow X^3\Sigma_g^-$) at 1.27 μm. These two filters have Gaussian passbands with 10 nm FWHM and are centered at 1.263 μm and 1.273 μm [*Warshaw et al.*, 1996]. Channel 3 measures the OH Meinel (4-2) and (3-1) bands at 1.520 μm and has an approximate top-hat passband with 40.0 nm FWHM [*Warshaw et al.*, 1996]. The infrared imager observations will be employed for a tomographic recovery of the 2-dimensional structure of the observed airglow emissions [*Degenstein*, 1999].

3.2.1 The Optical Spectrograph design

Fig. 3.6 illustrates schematically the Optical Spectrograph (OS) design. The OS has a 36 mm × 36 mm square aperture with truncated corners. Radiation enters the UV/Vis entrance port, goes through a set of baffles and vanes, and is then reflected by an off-axis parabolic objective mirror onto a flat folding mirror. Then, the radiation passes through the slit and is reflected by a second off-axis parabolic mirror that illuminates a blazed aspheric reflective grating. The first order light

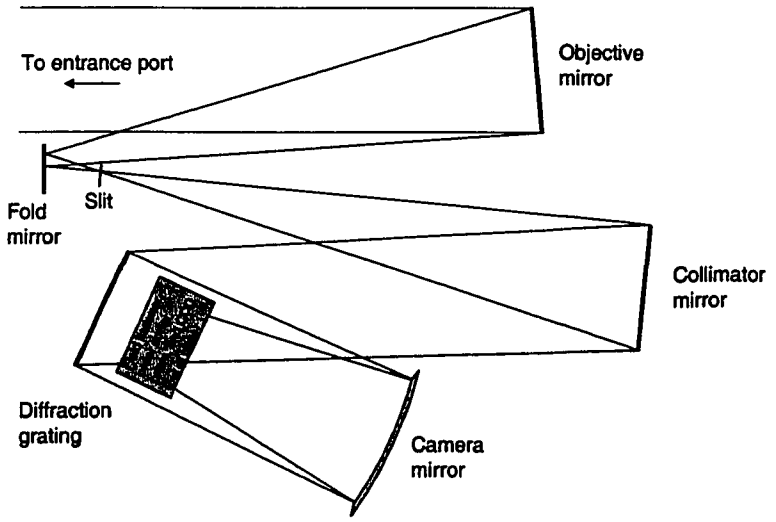

Figure 3.6: Layout of the Optical Spectrograph design (top view; adapted from *Warshaw et al.* [1996].

reflected off the grating is directed out of the main optical plane by a camera mirror through a combination of field-flattener, order sorter and prism (FOP) onto a CCD detector. The aspheric reflection grating, produced by Instruments SA/Jobin-Yvon, has a density of 600 lines/mm and operates in first order. Second order radiation that overlaps with the first order is removed with a filter that blocks radiation with wavelengths longer than 455 nm incorporated into the FOP between the prism and the exit lens, and positioned starting at the location of 480 nm dispersed light. The CCD detector has an active imaging area of 1353 × 143 pixels each having a size of 20 × 27 μm. The CCD is passively cooled to a nominal temperature of -20° C in orbit. The dispersed image of the slit is projected onto

Wavelength range	280 - 800 nm
Spectral Resolution	$\approx$ 0.9 nm, for $\lambda \in$ [280 nm,470 nm]
	$\approx$ 1.2 nm, for $\lambda \in$[530 nm,800 nm]
Slit orientation	horizontal
Vertical FOV	nominally 1 km
Horizontal FOV	nominally 40 km
Dynamic Range	> 3000
A/D converter	14 bits

Table 3.1: Technical parameters for the Optical Spectrograph

the CCD as a rectangle of 1353 by 44 pixels. The sampling ratio, *i.e.* the number of pixels per FWHM of the instrument function, is about 2.4. *Evans and Alfred* [2001] characterized the internal scatter and spectral cross talk of the Optical Spectrograph and also devised an algorithm to correct for contamination due to internal scattering (see section 5.1.7 for further information).

3.2.2 A sample limb scan

Fig. 3.7 shows a limb scan measured with the Optical Spectrograph on July 30, 2001 when the tangent point passed over Spitsbergen (78° N, 20° E), Norway. Interesting features are the O_2 *A* band between 7594 Å and 7621 Å appearing in absorption at lower tangent heights and in emission at higher tangent heights. The O_2 *B* band between 6976 Å and 6884 Å on the other hand, can only be seen in absorption since quenching of the *B* band upper state is stronger than for the

A band. Also noteworthy is the fact that the H_2O absorption band around 7250 Å can be identified even at the highest THs. This can be explained by multiply scattered photons carrying the absorption signature from the lower atmosphere to high THs. In many scans, although not in the present one, the Na doublet

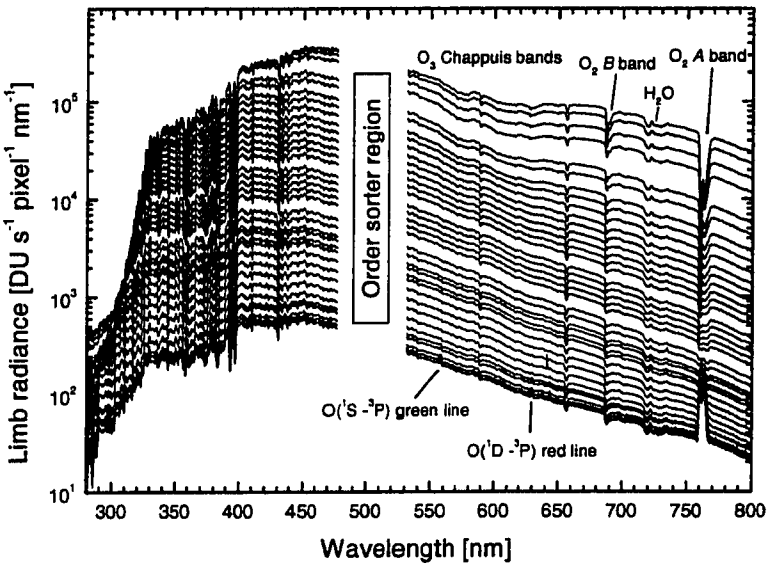

Figure 3.7: Example of the limb radiance spectra measured during an OSIRIS limb scan.

at 5896 Å and 5890 Å ($Na(^2P_{1/2,3/2} \rightarrow {}^2S)$) appearing as the D Fraunhofer line near the center of the ozone Chappuis absorption bands, can be identified as an airglow emission line at high THs. If sufficiently high THs are covered then the "green oxygen line" emission at 5577 Å, corresponding to the forbidden $O(^1S \leftarrow {}^3P)$ transition, as well as the "red oxygen line" at 6300 Å ($O(^1D \leftarrow {}^3P)$) can be observed.

Of great importance for the present thesis are of course the ozone absorption features that are easily identified in the spectra shown in Fig. 3.7. Absorption in the Huggins bands of ozone is responsible for the sharp gradient in the limb spectra at about 320 nm. At lower THs absorption in the Chappuis bands of ozone centered around 600 nm can be clearly identified in the limb spectra. The impact of the ozone Chappuis absorption bands on the observed limb radiance spectra is employed in the method described in Chapter 4 to retrieve vertical ozone density profiles from OSIRIS limb scans.

3.3 Main scientific objectives of the Odin aeronomy mission

Murtagh et al. [1993; 2002] identified the following topics as the main scientific objectives of the Odin aeronomy mission:

- *Stratospheric O_3 science*: Study of the geographical extent of and mechanisms responsible for ozone depletion in the ozone hole region and possible heterogeneous chemistry even outside of polar regions due to sulphate aerosols (OS and SMR).
- *Mesospheric O_3 science*: Establish the relative role of odd hydrogen chemistry and effects of transport and radiation (IRIS[1] and SMR).
- *Summer mesospheric science*: Establish the variability of mesospheric water vapor including an assessment of the required fluxes for aerosol formation in the polar

[1]Infrared Imager System

mesosphere (SMR and OSIRIS).

- *Coupling of atmospheric regions*: Downward transport of aurorally enhanced NO from the MLT (Mesosphere/Lower Thermosphere) region into the stratosphere and its impact on stratospheric O_3 photochemistry, as well as downward transport of NO during polar night [e.g., *Siskind and Russell*, 1996] (SMR).

OSIRIS has the potential to contribute to the first three items.

The main scientific goals of the optical spectrograph are the determination of vertical density profiles of stratospheric O_3, NO_2, OClO and possibly BrO. All those species are potentially retrievable with DOAS (Differential Optical Absorption Spectroscopy) [*Platt*, 1994] and their column amounts were in the past retrieved with ground-based [*Eisinger et al.*, 1997; *Frieß et al.* 1999] and satellite-based spectrometers, e.g. GOME [*Burrows et al.*, 1999]. Furthermore, PMCs (Polar Mesospheric Clouds) have already been detected and mapped using limb spectra observed with the optical spectrograph [*Petelina et al.*, 2001; *Evans et al.*, 2001], and PSCs (Polar Stratospheric Clouds) may be detected as well immediately after the end of the polar night. Furthermore, the OSIRIS limb radiance spectra contain information on stratospheric sulphate aerosols.

The main goal of the Infrared Imager is the tomographic reconstruction of 2-D airglow emission rate fields. Densities of mesospheric ozone can be determined from the IR *A* band emission at 1.27 μm caused by the ozone photolysis product $O_2(^1\Delta_g)$ [*Evans and Llewellyn*, 1972]. Moreover, the combination of mesospheric

O_3 profiles and OH volume emission rates observed with the 1.53 μm channel of the infrared imager will provide atomic hydrogen density profiles [*Evans and Llewellyn*, 1973]. The infrared imager channels can also be used for PMC and PSC detection.

3.4 Methods to retrieve stratospheric ozone density profiles from Odin

Three different methods are applied to OSIRIS limb spectra to retrieve stratospheric ozone density profiles: (a) the method based on normalized and paired limb radiance profiles discussed in the following Chapters of the present thesis, (b) limb DOAS, and (c) Modified Onion Peeling (MOP). The following subsections briefly introduce the limb DOAS and MOP techniques.

Furthermore, the SMR is also capable of measuring stratospheric ozone density profiles. The availability of 4 different methods to retrieve stratospheric ozone density profiles from measurements of both instruments on Odin offers the advantage of cross comparison and consistency checks.

3.4.1 DOAS with OSIRIS limb spectra

Differential Optical Absorption Spectroscopy (DOAS) [*Platt*, 1994] may also be applied to recover vertical profiles of ozone density from OSIRIS limb spectra. The

method is capable of yielding vertical density profiles of other minor species, *e.g.* NO_2, OClO and maybe BrO as well. The difficulty of DOAS in limb scattering geometry, compared to occultation measurements, is that the inversion process from profiles of apparent absorber column densities to vertical absorber density profiles requires forward modelling with a multiple scattering RT model that takes all important physical processes into account. *McDade et al.* [2002] demonstrated that recovery of ozone density profiles from DOAS analysis of limb spectra and subsequent inversion is possible with a linear inversion scheme in a single scattering (SS) atmosphere. *Infante* [2001] showed that recovery of vertical absorber density profiles from multiple scattering limb radiance spectra requires a nonlinear retrieval scheme, *e.g.* a Newtonian iteration version of optimal estimation [*Rodgers*, 1976]. *Haley et al.* [2001b] and *Sioris et al.* [2001] applied DOAS to OSIRIS limb spectra and obtained vertical profiles of O_3 and NO_2 using optimal estimation.

3.4.2 Modified Onion Peeling

Auvinen et al. [2001a] describe an algorithm developed to analyze OSIRIS limb spectra. It is a modified onion peel (MOP) method that uses a non-linear Levenberg-Marquard [*e.g.*, *Press et al.*, 1992] algorithm to determine the O_3 and NO_2 density, background density and aerosol number density profiles from many spectral points for each atmospheric shell assuming a typical aerosol size distribution and ground albedo. The iterative algorithm works its way down from the top

of the model atmosphere to the surface. Initial results indicate that the method yields very reasonable ozone density profiles [*Auvinen et al.*, 2001b].

Chapter 4

Methodology

4.1 Retrieval of ozone density profiles from limb scatter observations

This section describes the method used in subsequent sections to retrieve ozone density profiles from limb radiance profile observations made with the optical spectrograph. It starts with an introduction of the fundamental characteristics of limb radiance profiles and their dependence on ground albedo (section 4.1.1), followed by a discussion of the application of limb radiance measurements for attitude determination (section 4.1.2).

The method employed for ozone profile retrieval is introduced in the sections 4.1.4 and 4.1.5 and follows the method described by *Flittner et al.* [2000] and *McPeters et al.* [2000] who applied it to limb radiance profiles measured with

the LORE/SOLSE experiment. It essentially consists of the application of optimal estimation (OE) [*Rodgers*, 1976; 1990] (discussed in section 4.2) to a retrieval vector derived from the limb radiance profiles which is very sensitive to ozone, but has little sensitivity to all other parameters. OE iteratively adjusts the estimate of the ozone density profile by comparing the observed retrieval vector with a retrieval vector simulated with the forward model LIMBTRAN [*Griffioen and Oikarinen*, 2000] described in section 4.3.

4.1.1 General characteristics of limb radiance profiles

In the context of the OS measurements limb radiance corresponds to the solar radiation that is Rayleigh and Mie-scattered along the line of sight (LOS) and transmitted into the field of view (FOV) of the observer. Airglow emissions also contribute to limb radiances at different wavelengths, but they do not contaminate limb radiances at the wavelengths used for the retrieval of ozone density profiles with the method applied here. The sources of the scattered radiation are (a) the direct solar beam typically from above (for SZA $< 90°$) and (b) diffuse radiation that mainly comes from the denser atmosphere below the tangent point. Component (a) is the single scattering (SS) contribution, and component (b) the multiple scattering (MS) contribution to the total limb radiance. The fraction of MS radiation depends on SZA, the change in azimuth angle $\Delta\phi$, the atmosphere's aerosol loading, the presence of clouds and ground albedo. It changes rather slowly with

$\Delta\phi$, but more rapidly with SZA. For example, for $\lambda = 500$ nm and TH = 20 km the fraction of MS radiation decreases with increasing SZA from about 50 % at SZA = 0° to approximately 15-20 % at SZA = 90° [*Oikarinen et al.*, 1999]. These simulations were carried out with stratospheric background aerosols and a ground albedo of A = 0.3.

Scattering along the LOS into the FOV of the instrument competes with the attenuation along the LOS due to extinction by scattering out of the LOS and by absorption. If the atmosphere is optically thin (the LOS optical depth is $\tau_{\mathrm{LOS}} \ll 1$) then the limb radiance is approximately proportional to the number of scatterers along the line of sight. Due to the exponential increase in neutral density the limb radiance will therefore increase exponentially with decreasing TH. This is illustrated in Fig. 4.1 which shows limb radiance profiles at several wavelengths between 280 and 750 nm. Above about 65 km the limb radiance profiles at all wavelengths approximately decrease exponentially with increasing TH. In the optically thin case most of the scattered photons will originate from within an air volume at or near the tangent point.

If the LOS optical depth is $\tau_{\mathrm{LOS}} > 1$ then the transmission from the tangent point to the observer is reduced leading to a slower increase of limb radiance with decreasing TH and the majority of the photons will not have experienced the last scattering event at the tangent point, but somewhere between the tangent point and the observer. For sufficiently low THs the limb radiance "saturates" and does

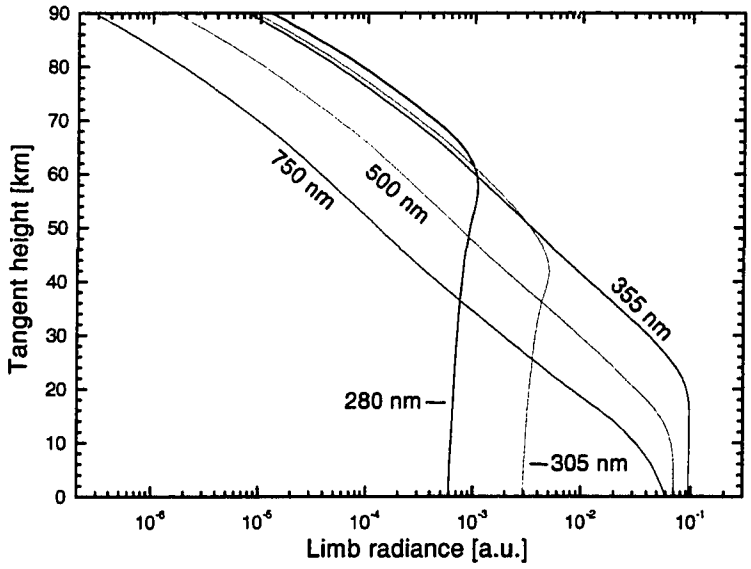

Figure 4.1: Examples of limb radiance profiles (in arbitrary units) at different wavelengths determined for a tropical atmosphere, stratospheric background aerosol (MODTRAN) and ground albedo A = 0.3 using LIMBTRAN. The viewing geometry parameters are: SZA = 70°, $\Delta\phi$ = 90°. The larger the extinction coefficients, the higher the "knee" altitude.

not increase further. Depending on observation geometry and wavelength the limb radiance profile can even assume a peak. As illustrated in Fig 4.1 the saturation occurs at higher TH for shorter wavelengths, a consequence of greater molecular absorption (by ozone at 280 and 305 nm) and due to greater Rayleigh and Mie-extinction coefficients (at 355 nm).

4.1.2 Attitude determination with the "knee"

During the initial period of OSIRIS observations attitude data was either not available or was of poor quality. As a consequence the shape of limb radiance profiles

at certain wavelengths was used for attitude determination. *Janz et al.* [1996] used the "knee" of the limb radiance profile at 355 nm to determine the attitude of a limb imaging instrument with the RSAS (Rayleigh Scattering Attitude Sensor) flown on NASA's space shuttle. 355 nm was considered a suitable wavelength, since it is mainly affected by Rayleigh scattering, making it insensitive to potentially highly variable minor constituent density profiles. Further investigation [*Sioris et al.*, 2001] using the radiative transfer model MODTRAN 3.5 [*Berk et al.*, 1989] showed that 355 nm is not a suitable wavelength for satellite attitude determination, since, depending on albedo, stratospheric aerosols and the presence of clouds, the knee may appear anywhere between about 0 and 25 km. For the initial ozone recoveries from OSIRIS limb spectra we used the limb radiance profile at a wavelength of 305 nm, which assumes a knee at altitude 44 km (see Fig. 4.1). The estimated accuracy is < 1 km. The ozone profiles used for this test are the MODTRAN profiles for both tropical and polar latitudes. Excellent agreement was achieved between the retrieved ozone density profiles and ozone sonde profiles [*Savigny et al.*, 2001] (see also Fig. 4.9 in section 4.4) as well as between the retrieved NO_2 profiles and POAM NO_2 profiles [*Sioris et al.*, 2001] indicating that the limb radiance profile at 305 nm allows for an accurate attitude determination. The extinction of solar radiation at a wavelength of 305 nm is dominated by ozone, whereas it is dominated by Rayleigh scattering at 355 nm. The main reasons why the position of the knee of the limb radiance profile at 305 nm is a more reliable

attitude indicator than at 355 nm are: (a) due to the strong absorption by ozone, limb radiances at 305 nm are very insensitive to albedo, clouds and stratospheric aerosols; and (b) ozone densities are not very variable above 40 km [*Sioris et al.*, 2001].

It is also noteworthy that the Student Nitric Oxide Explorer (SNOE) [*Solomon et al.* 1998], measuring nitric oxide in the MLT (Mesosphere/Lower Thermosphere) region by detecting solar UV radiation resonantly scattered in the (1,0) and (0,1) γ-bands of NO with an ultraviolet spectrometer (UVS), employs the knee of the limb radiance profile at $\lambda = 237$ nm [*D. K. Mankoff*, private communication, 12/2001] for attitude determination.

4.1.3 Line of sight optical depth

In order to estimate the lower boundary of the TH range that is sensitive to ozone density, the dependence of the LOS optical depth τ_{LOS} (from the tangent point to the observer) on TH was studied. τ_{LOS} was calculated with MODTRAN 3 [*Berk et al.*, 1989] for (a) a tropical atmosphere, and (b) an arctic atmosphere with background stratospheric aerosols in both cases. The different atmospheres were considered, because the significant latitudinal dependence of the ozone profile may introduce a latitudinal variation of the altitude range for which ozone densities can be retrieved. MODTRAN calculates the transmission and LOS optical depth in a spherical atmosphere. It is important to note that the retrieval method described

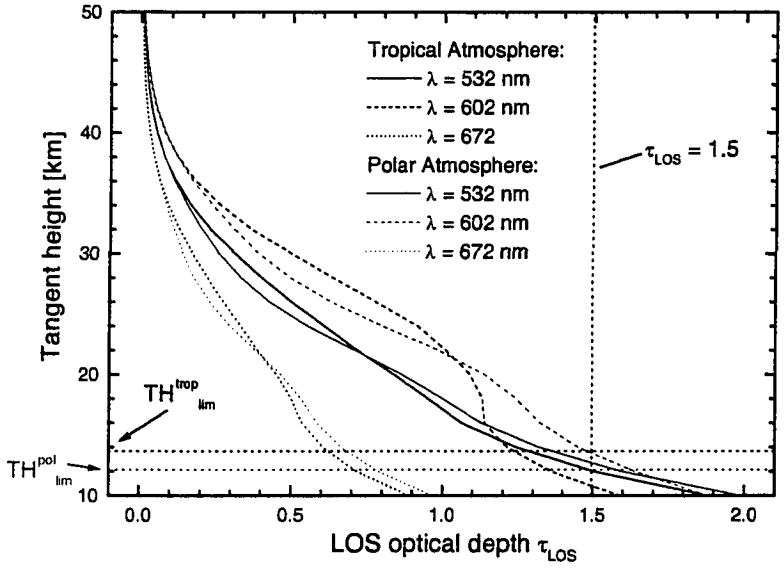

Figure 4.2: The LOS optical depth τ_{LOS} at the three wavelengths employed for the ozone retrievals is shown for (a) a tropical and (b) a polar atmosphere as calculated with MODTRAN 3 in a spherical shell atmosphere.

in subsequent sections works well in the optically thin case, *i.e.* if the τ_{LOS} is small, *i.e.* $\tau_{\mathrm{LOS}} \ll 1$. In this case a significant fraction of the detected photons will experience the last scattering event at or near the tangent point. That also implies that the optical depth between the sun and the tangent point must be small. For large SZAs the altitude range that can be "seen" with OSIRIS is limited further, since the transmission of radiation from the sun to the tangent point is reduced.

Figure 4.2 shows the LOS optical depth τ_{LOS} as a function of tangent height at the three wavelengths that are used for the ozone profile recoveries in the Chappuis-Wulf absorption bands of ozone (see section 4.1.5). At $\lambda = 532$ nm and $\lambda = 672$ nm τ_{LOS} is dominated by Rayleigh extinction, whereas absorption by ozone

dominates the extinction at $\lambda = 602$ nm. Fig. 4.2 indicates that the lower limit of the TH range sensitive to ozone is about $TH_{lim}^{trop} = 14$ km in the tropics and $TH_{lim}^{pol} = 12$ km at polar latitudes, if a LOS optical depth threshold of 1.5 is assumed. For higher latitudes this is well above the tropopause, i.e. interference with tropospheric clouds appearing in the FOV does not occur. At low latitudes the penetration depth is further limited by the frequent occurrence (40-50 %) of cirrus clouds at the tropical tropopause, most of which are subvisible [*Wang et al,* 1996]. *Peter et al.* [2001] reported the detection of subvisible cirrus clouds with a vertical extension of 100-300 m, but a horizontal extension of several thousand square kilometers and at altitudes up to 17 km. Furthermore, cumulonimbus clouds may reach or even penetrate the tropopause if the equivalent temperature of the rising air volumes is large enough [e.g., *Rödel,* 1992]. The impact of clouds on the ozone retrievals is investigated in section 5.1.6.

Fig. 4.3 shows a contour plot of the optical depth τ for a slant path to space as a function of the altitude of the lowest point of the path and zenith angle. Note, that for ZA = 90° the altitude corresponds to the TH and the optical depth τ then corresponds to the OSIRIS LOS optical depth τ_{LOS}. Clearly, the optical depth τ increases with increasing zenith angle. The zenith angle dependence of τ is important, because the solar photons have to reach the tangent point before they can be scattered into the FOV of the observer. For SZA $\ll 90°$ τ is apparently very small and the transmission from the sun to the scattering point is high. For

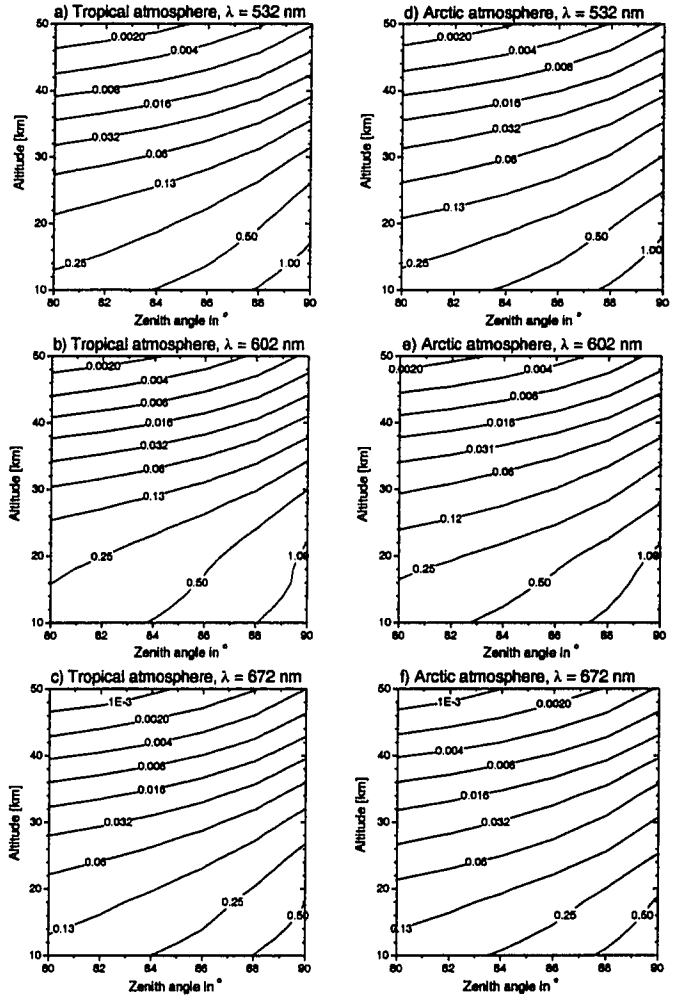

Figure 4.3: The optical depth for a slant path to space as a function of the altitude of the lowest point of the path and ZA (zenith angle) for the three wavelengths used for the ozone retrieval. For ZA = 90° the altitude is identical to the TH. Panels a - c correspond to a tropical background atmosphere and ozone profile. Panels d - f are for an arctic atmosphere and ozone profile. The simulations were performed with MODTRAN 3 [*Berk et al.*, 1989].

example, if SZA < 87° then τ < 1.0 for all three wavelengths employed in the ozone retrievals. As discussed in section 3.1, SZAs close to 90° in terms of the OSIRIS viewing geometry, occur at low latitudes throughout the year and at all latitudes near the terminator days.

4.1.4 Step I: Normalization of radiance profiles

The first step in the retrieval scheme consists of normalizing the individual limb radiance (LR) profiles using the radiance at a reference tangent height (TH_{ref}) to produce LR_N, the normalized limb radiance as

$$LR_N(TH_i, \lambda) = \frac{LR(TH_i, \lambda)}{LR(TH_{ref}, \lambda)}, \qquad i = 1, \ldots, N_{TH} \tag{4.1}$$

where N_{TH} is the total number of tangent heights used. The effect of this normalization is twofold: (a) it reduces the dependence on albedo and clouds while preserving the sensitivity to ozone and (b) it renders the absolute calibration of the instrument unnecessary, similar to the self-calibration feature of solar occultation measurements [*e.g.*, *Chu et al.*, 1989]. The reference TH used for all the ozone profile retrievals employing the Chappuis-Wulf system presented in the following Chapters is $TH_{ref} = 50$ km. It is important to realize that normalization does not entirely remove the albedo sensitivity of limb radiances, but reduces it significantly.

The combination of several wavelengths discussed in section 4.1.5 and appendix D further reduces the sensitivity to ground albedo, aerosols and clouds. Fig. 4.4 shows absolute and normalized limb radiance profiles at 532 nm for SZAs of 60° and 80° with albedos changing from 0.0 to 1.0 in steps of 0.2. The limb radiance profiles were calculated with LIMBTRAN for an azimuth angle of $\Delta\phi = 90°$ and stratospheric background aerosol. The following conclusions can be drawn from the figures:

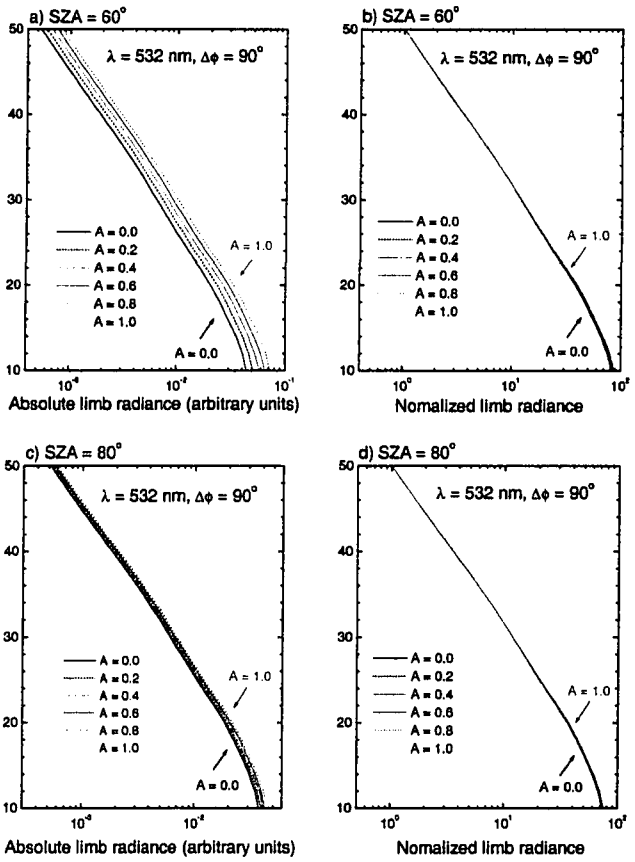

Figure 4.4: Illustration of the effect of normalization on the albedo dependence of limb radiance profiles for $\lambda = 532$ nm, SZA = 60° (panels a and b) and SZA = 80° (panels c and d). The reference tangent height is $TH_{ref} = 50$ km. The albedo sensitivity of limb radiances obviously decreases with increasing SZA.

- Absolute limb radiances are very sensitive to ground albedo and albedo affects the limb radiance at all THs, not only those close to the Earth's surface
- The albedo dependence of limb radiance decreases with increasing SZA, which is a consequence of increasing LOS optical depth
- Normalization significantly reduces the impact of albedo on the limb radiance

profiles

4.1.5 Step II: Wavelength pairing

Lower stratospheric Ozone from Chappuis-Wulf band absorption

Due to the large optical depths in the Huggins bands of ozone in limb geometry the lower stratosphere is inaccessible for their use. Therefore, for ozone retrievals at altitudes below approximately 25 km the Chappuis-Wulf absorption bands of ozone have to be employed. Following *Flittner et al.* [2000] we use limb radiance profiles at three wavelengths: 602 nm, which is in the center of the Chappuis bands ($^1A_2 \leftarrow X^1A_1$ and $^1B_1 \leftarrow X^1A_1$ transitions), 532 nm in the wing of the Chappuis bands and 672 nm in the Wulf bands ($^3A_2 \leftarrow X^1A_1$ and $^3B_1 \leftarrow X^1A_1$ transitions) of ozone. The normalized limb radiance profiles are then combined to form the *Chappuis retrieval vector* $\mathbf{y}_C(TH)$, a column vector containing the combined limb radiances for different THs:

$$\mathbf{y_C}(TH_i) = \frac{LR_N(TH_i, \lambda = 602 \text{ nm})}{\exp\left(\frac{1}{2}\left[\ln LR_N(TH_i, \lambda = 532 \text{ nm}) + \ln LR_N(TH_i, \lambda = 672 \text{ nm})\right]\right)} \tag{4.2}$$

$$= \frac{LR_N(TH_i, \lambda = 602 \text{ nm})}{\sqrt{LR_N(TH_i, \lambda = 532 \text{ nm}) \times LR_N(TH_i, \lambda = 672 \text{ nm})}}, \qquad i = 1, \ldots, N_{TH}$$

Figure 4.5 shows simulated and observed retrieval vectors $\mathbf{y_C}(TH_i)$ for different albedos and stratospheric aerosol loadings. The open squares, solid circles and

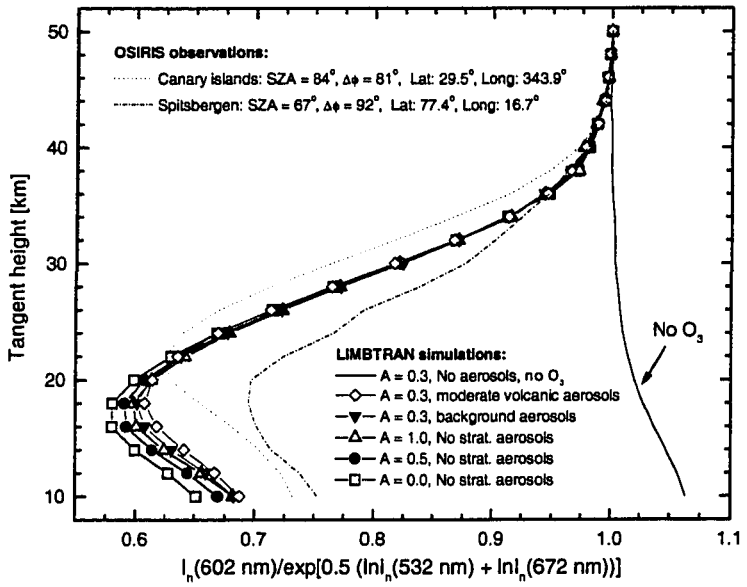

Figure 4.5: Sample Chappuis retrieval vectors $\mathbf{y}_C(TH_i)$ as modelled with LIMBTRAN (SZA = 80°, $\Delta\phi = 90°$, high latitude ozone profile) and as observed with OSIRIS for different scenarios. The height of the minimum is correlated with the height of the stratospheric ozone peak. The black solid line corresponds to a stratosphere without ozone.

open triangles correspond to an aerosol free stratosphere and ground albedos of A = 0.0, 0.5, 1.0 and the same atmospheric ozone profile. Obviously the retrieval vectors differ, but the difference is relatively small. For comparison the vector for an ozone free atmosphere (solid line) is also shown in Fig. 4.5. The apparent difference between the vector without ozone and the other vectors comprises the "signal" used to recover ozone profiles. The vectors indicated by solid inverted triangles and open diamonds correspond to retrieval vectors for different stratospheric aerosol loadings and an albedo of A = 0.3. Again, the retrieval vectors are not entirely insensitive to aerosols, but the sensitivity is rather small. A quantitative characterization of the

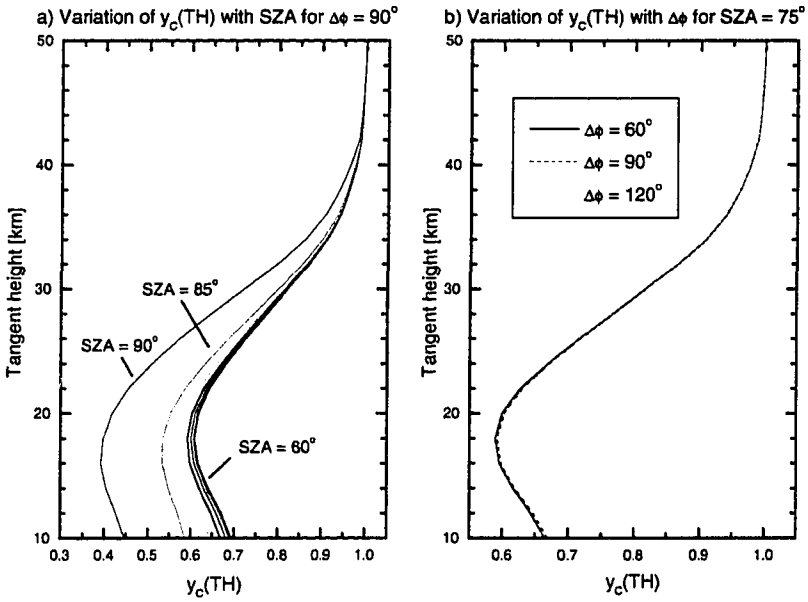

Figure 4.6: The dependence of the Chappuis retrieval vector $\mathbf{y_C}(TH_i)$ on SZA (panel a) and azimuth angle $\Delta\phi$ (panel b).

sensitivity of recovered ozone profiles to albedo, stratospheric aerosols and other important geophysical and instrumental parameters is given in Chapter 5.

Fig. 4.5 also shows two retrieval vectors derived from OSIRIS measurements. The first corresponds to a limb scan performed during an Odin overpass over the Canary Islands (about 29° N, 26° W) off the Atlantic coast of Africa on August 22, 2001 at 18:48 UTC. The second vector was derived from a limb scan on August 08, 2001 at about 7:32 UTC over Spitsbergen (about 79° N, 17° E) in the Arctic Sea. Those observations were chosen, because ozone sondes were launched from Santa Cruz on Teneriffa (Canary Islands) and from Koldewey station on Spitsbergen on the corresponding days. The fact that the minimum of the vector occurs at a lower

TH for the Spitsbergen scan compared to the Canary Island scan is indicative of lower altitudes of the peak of the stratospheric ozone layer at higher latitudes as compared to lower latitudes.

The Chappuis retrieval vector $\mathbf{y_C}(TH_i)$ is quite insensitive to the azimuth angle $\Delta\phi$. Panel b in Fig. 4.6 shows the $\mathbf{y_C}(TH_i)$ for $\Delta\phi = 60°$, 90° and 120° and SZA = 75°. The values of $\mathbf{y_C}(TH_i)$ for all tangent heights between 10 and 50 km vary by less than 0.7 % if $\Delta\phi$ is changed from 90° to 60° and 120°. For tangent heights greater than 30 km the change is less than 0.1 %. As illustrated in panel a of Fig. 4.6 the retrieval vector is more sensitive to SZA, particularly for smaller SZAs.

As mentioned above, the basic idea behind the ozone density profile recoveries is to use optimal estimation (OE) [*Rodgers*, 1976] together with the radiative transfer model LIMBTRAN [*Griffioen and Oikarinen*, 2000] to adjust a modelled Chappuis retrieval vector to the observed vector. Optimal estimation and LIMBTRAN is described in the following sections 4.2 and 4.3. A method employing limb radiance profiles in the Huggins absorption bands of ozone is described in Appendix D.

4.2 Optimal estimation

4.2.1 The linear case

Optimal estimation is based on the weighted combination of two independent measurements x_1 and x_2 with standard deviations σ_1 and σ_2 as weights:

$$\hat{x} = \left(\frac{1}{\sigma_1^2} + \frac{1}{\sigma_2^2}\right)^{-1} \left(\frac{x_1}{\sigma_1^2} + \frac{x_2}{\sigma_2^2}\right) \tag{4.3}$$

If the measurement consists of vector quantities $\mathbf{x}_1$ and $\mathbf{x}_2$ instead of scalar quantities the above equation can be generalized using covariance matrices $\mathbf{S_1}$ and $\mathbf{S_2}$ instead of standard deviations (vectors are denoted by lowercase boldface letters and matrices appear as uppercase boldface letters):

$$\hat{\mathbf{x}} = \left(\mathbf{S_1^{-1}} + \mathbf{S_2^{-1}}\right)^{-1} \left(\mathbf{S_1^{-1}}\mathbf{x}_1 + \mathbf{S_2^{-1}}\mathbf{x_2}\right) \tag{4.4}$$

The covariance matrix of $\hat{\mathbf{x}}$ is given by

$$\mathbf{S}_{\hat{x}} = \left(\mathbf{S_1^{-1}} + \mathbf{S_2^{-1}}\right)^{-1} \tag{4.5}$$

In terms of retrieval of atmospheric composition one usually has an *a priori* constraint (*e.g.*, a climatological or modelled profile), which will be referred to as a *virtual* measurement $\mathbf{x_0}$ and a real measurement $\mathbf{y}$. In the linear case the measurement vector $\mathbf{y}$ is related to the quantity $\mathbf{x}$ to be retrieved by $\mathbf{y} = \mathbf{Kx}$, with $\mathbf{K}$ being the weighting function matrix. Thus, one obtains

$$\hat{\mathbf{x}} = \left(\mathbf{S}_{x_0}^{-1} + \mathbf{K}^T\mathbf{S}_y^{-1}\mathbf{K}\right)^{-1} \left(\mathbf{S}_{x_0}^{-1}\mathbf{x}_0 + \mathbf{K}^T\mathbf{S}_y^{-1}\mathbf{y}\right) \tag{4.6}$$

with the covariance matrix

$$\mathbf{S}_{\hat{x}} = \left(\mathbf{S}_{x_0}^{-1} + \mathbf{K}^T\mathbf{S}_y^{-1}\mathbf{K}\right)^{-1} \tag{4.7}$$

where $\mathbf{S}_{x_0}$ and $\mathbf{S}_y$ are the covariance matrices of $\mathbf{x_0}$ and $\mathbf{y}$, respectively. $\mathbf{K}^T$ denotes the transpose of the weighting function matrix.

The equations 4.6 and 4.7 are equivalent to the following equations (as shown in Appendix A) which are generally used for retrievals:

$$\hat{\mathbf{x}} = \mathbf{x_0} + \mathbf{S}_{x_0}\mathbf{K}^T \left(\mathbf{K}\mathbf{S}_{x_0}\mathbf{K}^T + \mathbf{S}_y\right)^{-1} (\mathbf{y} - \mathbf{K}\mathbf{x_0}) \tag{4.8}$$

$$\hat{\mathbf{S}} = \mathbf{S}_{x_0} - \mathbf{S}_{x_0}\mathbf{K}^T \left(\mathbf{K}\mathbf{S}_{x_0}\mathbf{K}^T + \mathbf{S}_y\right)^{-1} \mathbf{K}\mathbf{S}_{x_0} \tag{4.9}$$

4.2.2 The nonlinear case

Many atmospheric retrieval problems are nonlinear and the linear retrieval theory is not directly applicable. In particular, the retrieval of stratospheric ozone density profiles from OSIRIS limb radiance spectra applying the limb radiance method described in the present Chapter poses a nonlinear problem for the following reasons:

- A linear approach would assume linearity between the Chappuis retrieval vector $\mathbf{y}_C$ and the ozone density profile $\mathbf{x}$: $\mathbf{y}_C = \mathbf{K}\mathbf{x}$, i.e. in particular $\mathbf{y}_C = \vec{0}$ if $\mathbf{x} = \vec{0}$. As is illustrated in Fig. 4.5 this is not the case here. If there is no ozone in the atmosphere, then the Chappuis retrieval vector does not vanish.

- For non optically thin conditions, absorption, e.g., by ozone, is an intrinsically nonlinear process (Beer's law), as is extinction by scattering. Hence, for example, the doubling of the ozone profile does not double the retrieval vector $\mathbf{y}_C$. Even an affine relation $\mathbf{y} = \mathbf{a} + \mathbf{K}\mathbf{x}$ is not appropriate.

If the retrieval problem is nonlinear a *Newtonian Iteration* method [*e.g.*, *Rodgers*, 1976] can be applied. It is based on the Taylor-expansion of the forward model $\mathbf{F}(\mathbf{x})$ about a profile $\mathbf{x}_n$:

$$\mathbf{y} = \mathbf{F}(\mathbf{x}) \approx \mathbf{F}(\mathbf{x}_n) + \partial\mathbf{F}/\partial\mathbf{x}(\mathbf{x} - \mathbf{x}_n) \tag{4.10}$$

where only the first order term is taken into account.

One obtains (for details see *Rodgers* [1976])

$$\mathbf{x}_{n+1} = \mathbf{x}_0 + \mathbf{S}_{x_0}\mathbf{K}_n^T \left(\mathbf{K}_n\mathbf{S}_{x_0}\mathbf{K}_n^T + \mathbf{S}_y\right)^{-1} ((\mathbf{y} - \mathbf{y}_n) - (\mathbf{K}_n(\mathbf{x}_0 - \mathbf{x}_n)) \tag{4.11}$$

The covariance matrix of the solution is given by:

$$\hat{\mathbf{S}} = \left(\mathbf{S}_{x_0}^{-1} + \hat{\mathbf{K}}^T\mathbf{S}_y^{-1}\hat{\mathbf{K}}\right)^{-1} \tag{4.12}$$

where $\hat{\mathbf{K}}$ is $\mathbf{K}$ evaluated at $\hat{\mathbf{x}}$, with $\mathbf{x_n} \to \hat{\mathbf{x}}$ for $n \to \infty$.

The above equations 4.11 and 4.12 are employed for the retrieval of ozone density profiles from OSIRIS limb radiance profiles. In this specific application, $\mathbf{x_0}$ corresponds to the natural logarithm of the *a priori* ozone density profile vector, $\mathbf{x_n}$ is the nth estimate of natural logarithm of the ozone density profile vector, $\mathbf{y}$

denotes the natural logarithm of the Chappuis retrieval vector determined from the observed limb radiance profiles and $\mathbf{y_n}$ corresponds to the natural logarithm of the retrieval vector determined with the forward model LIMBTRAN for the ozone density profile $\mathbf{x_n}$.

The use of logarithms instead of the actual ozone density profile and the Chappuis retrieval vector makes the retrieval stable. If non-logarithmic magnitudes are used, then the iterated estimate of the ozone density profile may contain negative values. This can occur due to (a) an inappropriate *a priori* (*i.e.* significant differences between the *a priori* and the actual ozone density profile), and (b) nonlinearity of the retrieval problem. For the initial OSIRIS ozone retrievals an algorithm applying non-logarithmic quantities was used, and the retrievals became unstable in approximately 3 % of all scans. Using logarithmic quantities ozone profiles can be successfully retrieved in 100 % of all scans tested.

The disadvantages of a nonlinear approach are: (a) the weighting function matrix (or Fréchet derivative [*Rodgers*, 1976]) has to be evaluated at the new linearization point $\mathbf{x}_{n+1}$ after every iteration step and (b) precalculation of weighting functions is not possible, which leads to increased computing time.

4.2.3 Weighting functions

The weighting function matrices $\mathbf{K}$ as well as the modelled retrieval vector $\mathbf{y}_n$ required for the retrieval are determined with the pseudo-spherical multiple scat-

tering RT model LIMBTRAN (see section 4.3). The weighting functions are determined numerically by perturbing the ozone density in every altitude bin by 5 % followed by running LIMBTRAN to calculate the perturbed limb radiance profiles at 532 nm, 602 nm and 672 nm from which the perturbed retrieval vector is calculated. The elements of the weighting function matrix are then simply obtained by

$$K_{nm} = \frac{\partial y(m)}{\partial x(n)} \approx \frac{\Delta y(m)}{\Delta x(n)} \tag{4.13}$$

where $\mathbf{x}$ again denotes the vector corresponding to the ln of the vertical ozone profile. Eqn. 4.13 indicates that the elements of the ideal weighting function matrix correspond to the partial derivatives of the ln of the retrieval vector element m with respect to the ln of the ozone profile vector element n. The rows of the weighting function matrix are also called weighting functions and their shape is indicative of the vertical resolution of the retrieval method. High vertical resolution cannot be achieved by narrow weighting functions alone, but also by a sharp cutoff.

Fig. 4.7 shows Chappuis weighting functions for SZAs increasing from 60° to 90° in increments of 10° both for a polar ozone profile (80°N, panels a to d) and a tropical ozone profile (10°N, panels e to h). The ozone profiles employed are the zonally averaged 10 year mean ozone profiles for August determined with the Canadian Middle Atmosphere Model [*de Grandpré et al.*, 2000]. The weighting functions are negative because an increased ozone density leads to enhanced absorption (i.e., smaller limb radiances at 602 nm relative to 532 nm and 672 nm).

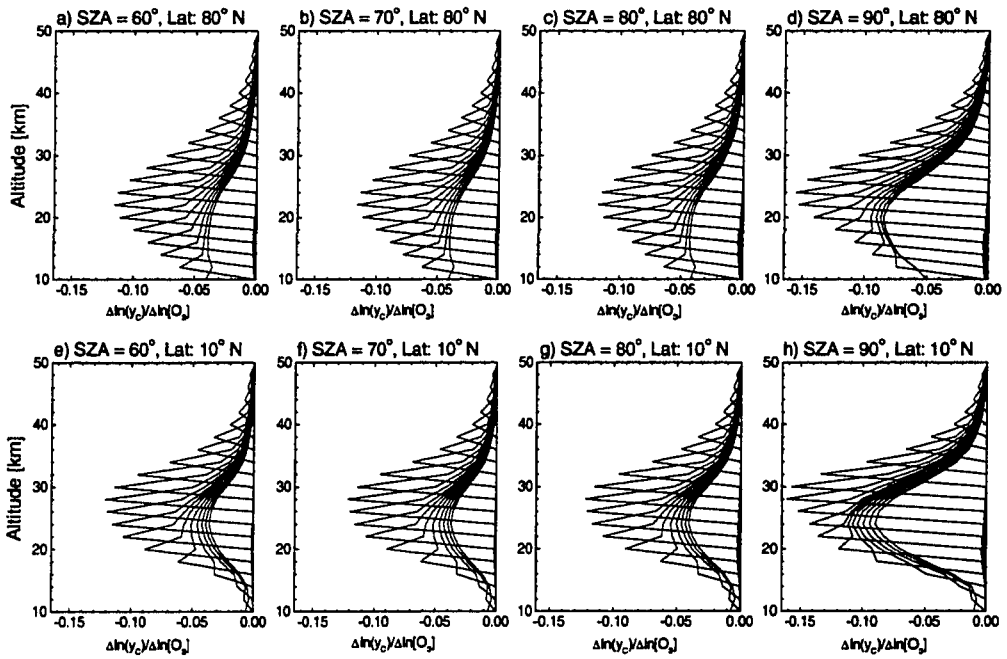

Figure 4.7: Chappuis retrieval weighting functions as a function of SZA for a polar ozone profile (top panels) and a tropical ozone profile (bottom panels). The large gradient below the peak is indicative of high vertical resolution.

Therefore, the value of the Chappuis retrieval vector becomes smaller, and so does its logarithm. Every line in Fig. 4.7 corresponds to a single TH and within the optically thin regime every weighting function peaks at an altitude equal to its TH. The sharp gradient of the weighting functions below the peak indicates that it should be possible to obtain high vertical resolution with the inversion process. As indicated in Fig. 4.7 for both tropical and polar latitudes, the weighting functions for SZA = 60°, 70°, and 80° do not differ significantly. This is not unexpected,

since the retrieval vectors $\mathbf{y_C}(TH_i)$ do not vary significantly for SZA $\in [60°, 80°]$ (see Fig. 4.6).

While in the case of the linear inversion problem the weighting function matrix is independent of the profile $\mathbf{x}$ where it is calculated, nonlinearity directly implies a dependence of $\mathbf{K}$ on the linearization point $\mathbf{x}_n$.

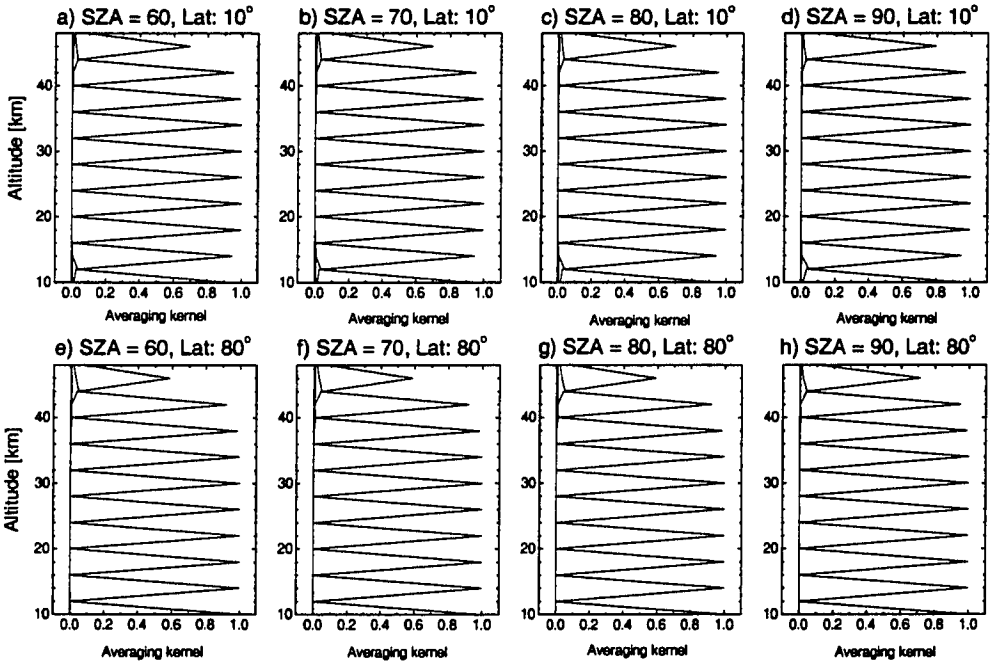

Figure 4.8: Selected averaging kernels for the weighting functions shown in Fig. 4.7. The width of the averaging kernels is a measure of the vertical resolution of the retrieval method.

4.2.4 Contribution functions and averaging kernels

While the weighting functions correspond to the sensitivity of the retrieval vector $\mathbf{y}$ to a change in $\mathbf{x}$, the contribution functions summarized in the contribution function matrix $\mathbf{D_y}$ correspond to the sensitivity of the retrieved vector to $\mathbf{y}$. The contribution function can be determined numerically or can be obtained from

$$\mathbf{D_y} = \mathbf{S_x K}^T \left(\mathbf{K S_x K}^T + \mathbf{S_y} \right)^{-1} \tag{4.14}$$

The correct vertical resolution of the method is inferred from the width of the averaging kernels (i.e., the rows of the averaging kernel matrix $\mathbf{A} = \mathbf{D_y K}$). Fig. 4.8 shows sample averaging kernels corresponding to the weighting functions shown in Fig. 4.7. The sharp shape of the kernels with a FWHM of about 2 km indicate that the vertical resolution of the retrievals is better than 2 km.

4.2.5 Sequential estimation

The solution of the optimal estimation equations does not require the inversion of matrices but can be done sequentially [*Rodgers*, 1976] by treating the measurement vector $\mathbf{y}$ as a set of scalars y_i, where $i = 1, \ldots, M$.

With $\mathbf{S_0} = \mathbf{S_{x_0}}$ the following operations have to be carried out:

$$\mathbf{x}_i = \mathbf{x}_{i-1} + \mathbf{S}_{i-1}\mathbf{k}_i \left(y_i - \mathbf{k}_i^T \mathbf{x}_{i-1} \right) / \left(\mathbf{k}_i^T \mathbf{S}_{i-1} \mathbf{k}_i + \sigma^2 \right) \tag{4.15}$$

$$\mathbf{S}_i = \mathbf{S}_{i-1} - \mathbf{S}_{i-1}\mathbf{k}_i\mathbf{k}_i^T\mathbf{S}_{i-1} / \left(\mathbf{k}_i^T \mathbf{S}_{i-1} \mathbf{k}_i + \sigma^2 \right), \quad \text{for } i = 1, \ldots, M$$

with $\mathbf{k_i}$ being the ith row of $\mathbf{K}$. Each element of $\mathbf{y}$ is treated separately and each step yields a new estimate of $\mathbf{x}$. Note, that the index i does not refer to the number of iterations of the nonlinear OE algorithm. A complete loop from $i = 1, \ldots, M$ yields the next estimate of the ozone density profile $\mathbf{x}_{n+1}$.

In the present work the optimal estimation equations for the ozone retrieval problem were solved sequentially.

4.3 LIMBTRAN

The retrieval of minor species density profiles from satellite based observations of nadir or limb scattered radiance profiles requires forward modelling. The radiative transfer for the limb geometry is more difficult than the nadir geometry, because the spherical shape of the Earth's atmosphere has to be taken into account, whereas it can be neglected in the nadir case if the SZA is sufficiently small. Full spherical models exist (*e.g.*, the Monte Carlo model Siro [*Oikarinen et al.* 1999; *Oikarinen* 2001a] or *Rozanov et al.* [2001], *Herman et al.* [1995]) but they are slower than simplified models and are not suited for many repetitive calculations. LIMBTRAN is a pseudo-spherical scalar RT code [*Griffioen and Oikarinen*, 2001] that solves the radiative transfer equation in an inhomogeneous atmosphere. The radiance observed by a limb scanning or imaging observer can be expressed in the following way

$$I(\Omega) = I_0(\Omega)e^{-\tau_0} + \int_0^{\tau_0} S(\tau)e^{-(\tau_0-\tau)}d\tau \tag{4.16}$$

where $I_0(\Omega)$ is the radiation outside the atmosphere directed at the observer, which is zero in the limb scatter case. τ is the optical depth along the LOS, which is zero at the observer and τ_0 is the total optical depth along the LOS. $S(\tau)$ is the source function that determines the contribution of radiation scattered towards the observer from all air volumes. The source function has two main contributions: (a) solar radiation, and (b) diffuse, *i.e.* multiply scattered solar radiation.

LIMBTRAN treats single scattering in a spherical shell atmosphere, whereas the diffuse contribution to the source function is calculated with a 1-D plane parallel (pp) model based on the finite differences method (FDM).

A spherical atmosphere can be approximated by taking the SZA variation of the MS contribution to the source function into account. The computing time is a linear function of the number of SZAs considered since the 1-D pp model has to be run for every SZA. The variation of the azimuth angle along the LOS is handled in the following way. The 1-D problem is solved by expanding radiances, source functions and phase functions in a Fourier series, which yields RT equations for each Fourier order. Once the Fourier coefficients are calculated the change in azimuth angle is easily determined for each grid point from the Fourier series without significant additional computational load.

The accuracy of the RT model used for the retrievals is important, since the

quality of the retrievals directly depends on it. The absolute accuracy of LIMBTRAN is not easily established with OSIRIS, since the instrument is not optimized for high accuracy of absolute limb radiances. A comparison with other radiative transfer models is easier and LIMBTRAN results were compared with the Monte Carlo RT model SIRO [*Griffioen and Oikarinen*, 2000; *Oikarinen et al.*, 1999] and with several other RT models [*Oikarinen et al.*, 2001b]. *Griffioen and Oikarinen* [2000] report that LIMBTRAN and SIRO agree to within 3 - 4 % for single scattering and within 15 % for multiple scattering in the 10 to 60 km TH range for a variety of SZAs, azimuth angles, Lambertian ground albedo values and wavelengths between 310 and 600 nm. It should be noted, that the agreement in the MS case is generally much better than 15 %.

4.4 Sample recoveries

To illustrate the potential of the method Fig. 4.9 shows sample ozone profiles recovered from the two measured retrieval vectors shown in Fig. 4.5. The recoveries are performed for the altitude range between 10 and 50 km. However, above about 40 km the method becomes insensitive to ozone and the recovered profiles asymptotically approach the *a priori* profile $\mathbf{x_0}$. Furthermore, below about 15 km the LOS optical depth exceeds $\tau = 1.5$, and the lower regions of the stratosphere become increasingly inaccessible with decreasing TH. At those altitudes the weighting functions become very small and no longer peak at the TH (see low THs in Fig.

4.7).

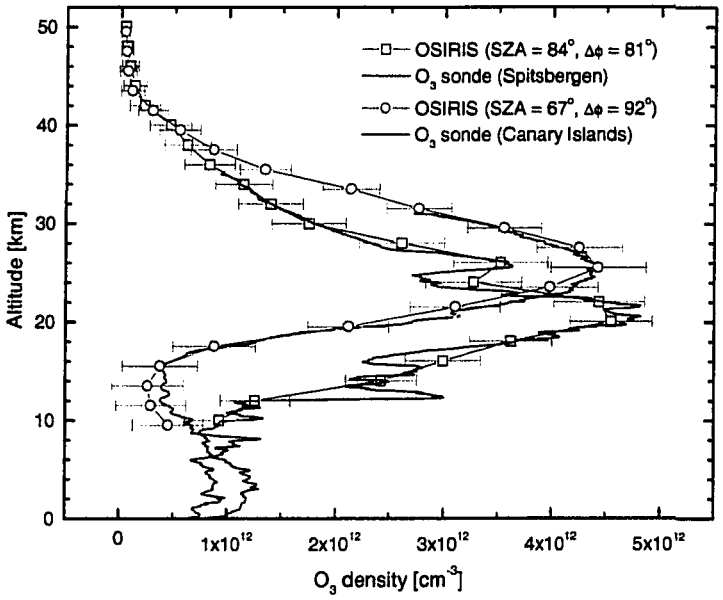

Figure 4.9: Example of retrieved ozone profiles and comparison with ECC sondes launched from the Koldewey station in Spitsbergen (Norway) and Santa Cruz on Teneriffa (Canary Islands). The recoveries are carried out between 10 km and 50 km, but the method is only sensitive to ozone in the 15 - 40 km range.

Fig. 4.9 allows the following conclusions to be made: (a) the general agreement between ozone density profiles derived from OSIRIS observations and measured with ozone sondes is excellent. The shape of the profiles as well as the peak altitudes and densities are almost perfectly retrieved, (b) structures in the ozone profiles with scales of less than several kilometers, *e.g.*, the laminae caused by meridional transport of air masses with higher or lower ozone densities in the stably stratified stratosphere, typical of mid- and high latitudes, cannot be recovered. This is due to (a) the geometrical vertical FOV of about 1 km, leading to an intrinsic smearing,

(b) an additional smearing caused by non negligible integration times, (c) the motion of the tangent point caused by the satellite's motion as well as its scanning, (d) the undersampling problem mentioned in Chapter 3, (e) the averaging kernel width on the order of 2 km, and (f) smearing along the LOS[1].

[1]The slant path segment for, *e.g.*, TH = 20 km between the 22 km altitude points corresponds to about 320 km.

Chapter 5

Error Analysis

The method used to recover vertical ozone density profiles described in Chapter 4 is based on limb radiance profiles at several wavelengths in the visible part of the solar spectrum. Those wavelengths were chosen to obtain the highest sensitivity to ozone possible. However, as has been noted before in Chapter 4, the limb radiance profiles used are not only affected by the stratospheric ozone density profile. Other geophysical parameters (*e.g.*, ground albedo) and instrumental properties (*e.g.* the instrument's polarization sensitivity, and noise) also affect the observed limb radiance profiles and an incorrect or insufficient knowledge of those parameters will interfere with an accurate recovery of the actual stratospheric ozone density profile. In this Chapter potential errors introduced by the most important error sources are estimated. Section 5.1 and associated subsections deal with systematic errors, and section 5.2 with random errors, *i.e.* instrument noise.

5.1 Systematic errors

5.1.1 Ground albedo

Although the normalized limb radiance profiles were shown to be relatively insensitive to ground albedo (section 4.1.4) and the albedo sensitivity is further reduced by combining normalized limb radiance profiles at different wavelengths in the retrieval vector $\mathbf{y_C}$ (section 4.1.5), its impact on the retrieved ozone density profiles has to be investigated for a thorough analysis of systematic errors. Since the impact of albedo on limb radiance profiles decreases with increasing SZA one also expects a decreasing impact of ground albedo on the retrieved ozone profiles with increasing SZA. The fact that the OSIRIS viewing geometry is associated with relatively large SZAs, *i.e.* SZA $> 57°$, can therefore be considered an advantage.

A study was carried out to determine the sensitivity of ozone retrievals using the Chappuis-Wulf system with respect to ground albedo. The "correct" albedo adapted was A = 0.5 and retrievals with simulated limb radiance profiles were carried out with albedos $A \in [0.0, 1.0]$ and SZA $\in [55°, 90°]$, where the albedo was increased in steps of 0.1 and the SZA was increased in steps of 5°.

Fig. 5.1 shows a contour plot of the relative difference between the correct partial vertical ozone column between 15 and 40 km and the retrieved partial ozone column if the assumed ground albedo is wrong. The partial ozone column is shown as a function of assumed albedo and SZA. The following features are obvious: (a)

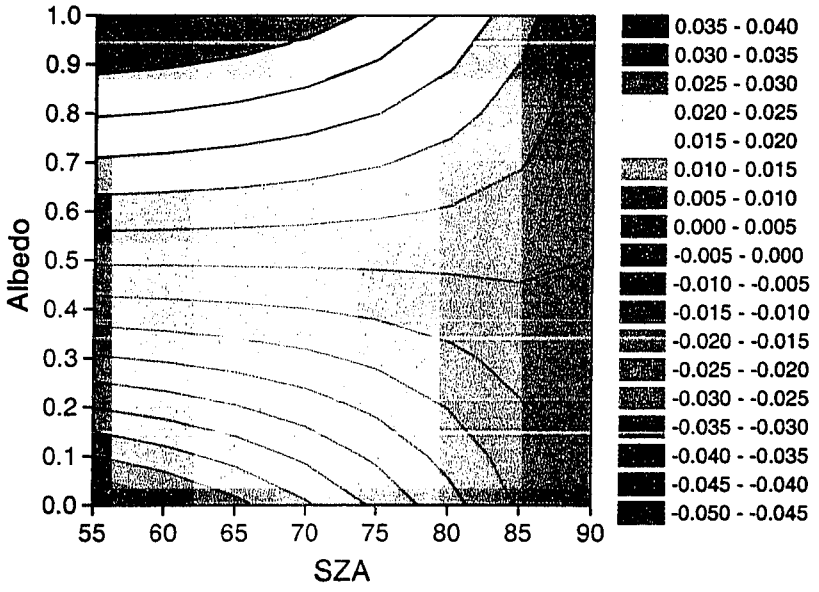

Figure 5.1: Relative retrieval error $([O_3]^{retrieved}\text{-}[O_3]^{true})/[O_3]^{true}$ of the partial ozone column between 15 and 40 km as a function of SZA and assumed albedo for a "true" albedo of A = 0.5. The error decreases with decreasing difference between the assumed and the true albedo and with increasing SZA.

the retrieval error increases with increasing difference between assumed and correct albedo; (b) the errors for a constant assumed albedo decrease with increasing SZA, which is expected from the fact that the impact of albedo on limb radiances decreases with increasing SZA [*e.g.*, *Oikarinen et al.*, 2000].

Fig. 5.2 shows the relative error in retrieved ozone density for altitudes between 10 and 38 km if the assumed albedo differs from the true albedo A = 0.5, as a function of assumed albedo and SZA. The largest errors occur as expected at the lowest altitudes, where the method is rather insensitive to ozone and the impact of disturbing parameters is greater. Above 15 km the error is smaller than about

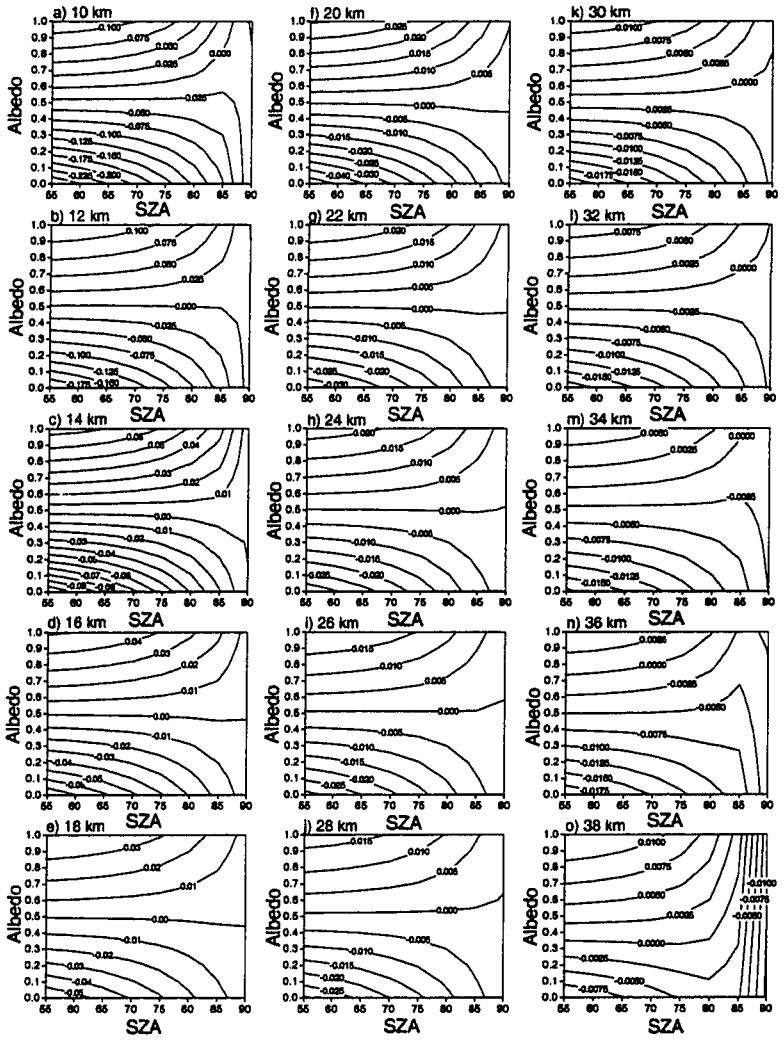

Figure 5.2: Relative retrieval error for a true albedo of A = 0.5 as a function of albedo and SZA and altitudes ranging from 10 to 38 km.

1.5 % for all SZA > 57° if the albedo is known to ± 0.15. With increasing altitude the resulting relative error decreases slightly. In the worst case, when the actual albedo is 0 or 1 and assumed to be A = 0.5, the error is less than 7% for altitudes ≥ 16 km, less than 5 % for altitudes ≥ 20 km, and less than 2 % for altitudes ≥ 30 km, if SZA ≥ 60°.

It can be assumed that ground albedo can be estimated from existing databases of global albedo [*e.g.*, *Matthews*, 1983] that include seasonal dependence to within $\pm$ 0.15, assuming the sensed air volumes are cloud free. Therefore, the sensitivity study presented in this section leads to the conclusion that the systematic errors in total ozone column introduced by an incorrect albedo are smaller than about 1.5 % between 15 and 40 km.

The insensitivity of the recovered ozone density profiles to ground albedo is a consequence of (a) normalization of the limb radiance profiles used in the retrieval, and (b) the use of a ratio of normalized limb radiance profiles for wavelengths that are affected by ground albedo in a similar way, to a first approximation.

5.1.2 Number of SZA used in interpolation

As already mentioned in section 4.3 the RT model LIMBTRAN employed for the ozone recoveries is not a fully spherical model. SS is treated in a spherical shell atmosphere, but the MS contribution to the source function is determined with a 1-D plane parallel model. Yet, the spherical atmosphere can be interpolated by taking the variation of SZA along the LOS into account, and the accuracy of the model depends on the number of SZAs used for the interpolation. Since the computational load is approximately a linear function of the number of SZAs considered (the 1-D pp MS model is run for each SZA separately) [*Griffioen and Oikarinen*, 2000] a compromise has to be found between speed and accuracy.

The variation of SZA along the LOS is a function of the azimuth angle $\Delta\phi$ and the tangent point SZA. In the special case of $\Delta\phi$ = SZA = 90° (e.g., on the terminator days) the SZA does not change at all along the LOS. In all other cases the SZA will vary along the LOS. For example, for $\Delta\phi$ = 121.3° and SZA = 90.0° at the tangent point, the SZA changes from about 95.0° to about 85.0° along the LOS for scattering altitudes below 100 km.

To estimate the impact of using only a few SZAs in the retrievals Chappuis retrieval vectors were determined for 41 SZAs and tangent point SZAs of 80°, 85° and 90°. The recoveries were then performed with 1, 3, 5, and 7 SZAs. The albedo was A = 0.3 for all cases and the simulations were performed for a pure Rayleigh scattering atmosphere. Four iterations of the OE algorithms were carried out.

Fig. 5.3 shows the vertical dependence of retrieval errors in percent for all cases and the altitude range 10 km to 40 km. Several aspects are obvious: (a) the retrieval error decreases with increasing number of SZAs used in the interpolation, which is easily explained, since the more SZAs are taken into account the more accurately the spherical atmosphere is simulated; (b) the retrieval errors for the same number of SZAs is dependent on SZA, and they increase with increasing SZA. This might be expected, since for greater SZAs the spherical correction becomes more important. For SZA = 90° the retrieval errors can be on the order of 20 - 30 % if only one SZA is considered in the interpolation. Large errors can be expected in this case since on the far side of the tangent point the SZA > 90° (*i.e.*, only

partly lit atmosphere and no directly illuminated ground). This has a large impact on the limb spectra but is completely ignored if only the MS contribution from the tangent point is considered. (c) an apparent asymmetry exists about the 0% line between $\Delta\phi = 58.7°$ (panels a, b, and c in Fig. 5.3) and $\Delta\phi = 121.3°$ (panels d, e, and f in Fig. 5.3).

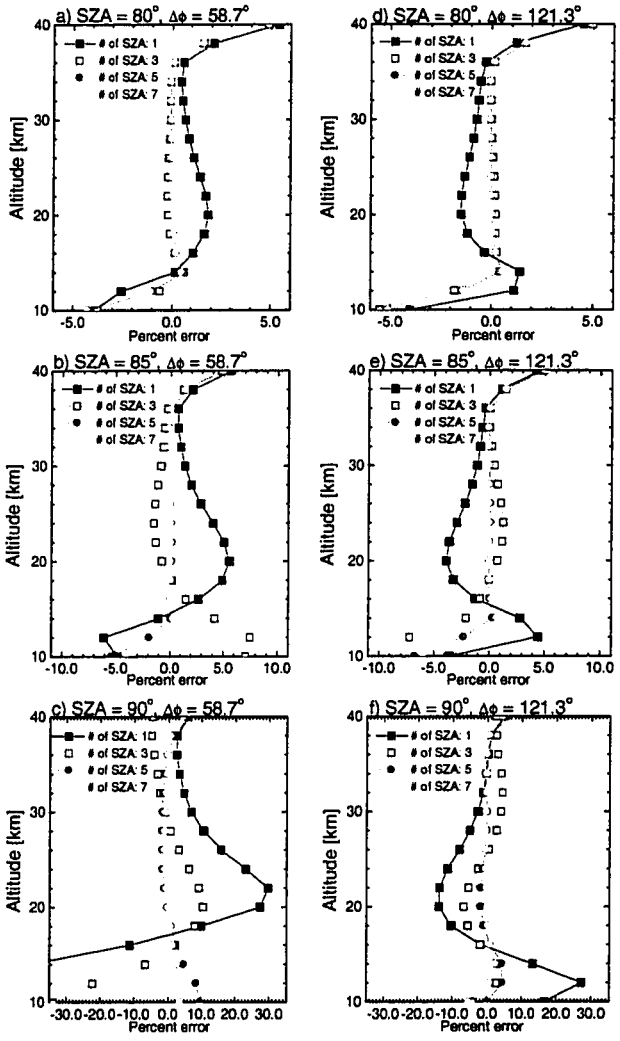

Figure 5.3: Retrieval error if LIMBTRAN is used with different numbers of SZAs (1,3,5, and 7) in the interpolation for SZA = 80°, 85°, and 90° and $\Delta\phi = 58.7°$, and 121.3°.

For SZA = 80° and 3 SZAs used in the interpolation the retrieval errors are smaller than 1 % between 15 and 36 km. For SZA = 85° the same number of SZAs results in retrieval errors of less than 2 % between 15 and 38 km.

To limit the computational time required for the ozone profile retrievals 3 SZAs are used in the interpolation of the SZA variation of the MS contribution to the source function. To limit the retrieval error only observations with SZAs $\leq$ 85° are included in the data analysis presented in the following Chapters. Under these conditions we can conclude that retrieval errors of less than 2 % between 15 km and 38 km can be expected.

It is important to note that additional errors may occur, if the spherical shape of the atmosphere is not correctly modelled with a large number of SZAs used in the interpolation. *Oikarinen et al.* [2001b] indicate that a systematic bias exists between fully spherical models and pseudo-spherical models including LIMBTRAN. The difference between LIMBTRAN and the fully spherical models Siro [*Oikarinen et al.*, 1999] and CDIPI (Combined Differential-Integral approach involving the Picard Iterative approximation) [*Rozanov et al.*, 2001] increases with increasing TH for all three wavelengths studied by *Oikarinen et al.* [2001] (*i.e.*, 325 nm, 345 nm, and 600 nm) and can reach several percent. Due to the combination of limb radiance profiles at different wavelengths, it is likely that the retrieved ozone profiles are relatively insensitive to systematic deviations of the modelled limb radiance profiles from correctly modelled limb radiance profiles. This requires further

study. The exact systematic error introduced can only be studied with a model that allows for both spherical and pseudo-spherical RT.

5.1.3 Stratospheric aerosols

The stratospheric aerosol loading has reached the lowest levels observed by modern instrumentation, due to an extended relaxation period after the last major volcanic eruption (*i.e.*, Pinatubo in 1991) [*e.g.*, *Thomason et al.*, 2001]. The MODTRAN background stratospheric aerosol extinction profile [*Berk et al.*, 1989] originally employed for ozone retrievals from OSIRIS observations therefore overestimates the actual stratospheric extinction. For this reason a mid-latitude aerosol extinction profile observed with the Polar Ozone and Aerosol Measurement III [*Lucke et al.*, 1999] in August 2001 was used instead.

An analysis of all limb scans performed on August 20, 2001 was carried out assuming the POAM III aerosol extinction profile and a Henyey-Greenstein [*e.g.*, *Hansen and Travis*, 1974] phase function with an asymmetry parameter (*i.e.*, average cosine of the scattering angle or $\langle \cos\Theta \rangle$) of $g = 0.7$. To study the impact of stratospheric aerosols on the retrieved ozone density profiles the analysis was repeated with doubled and tripled aerosol extinction coefficient profiles and the same aerosol phase function.

Panel a of Fig. 5.4 shows the dependence of the zonally averaged ozone profiles on August 20, 2001 for the latitude range 60°N to 65°N on the assumed aerosol

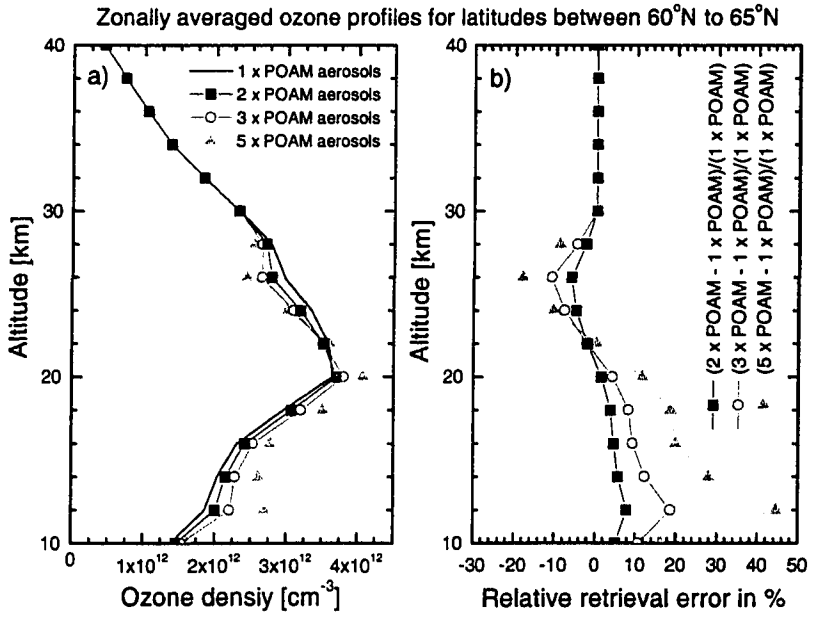

Figure 5.4: The sensitivity of the ozone retrievals to stratospheric aerosols. 1 x POAM corresponds to the stratospheric aerosol extinction profile measured by POAM III on August 20, 2001 at a latitude of 60°N.

extinction profile. An overestimate in the assumed stratospheric aerosol loading will lead to an under-determination of retrieved ozone densities above the peak of the ozone layer and to an over-determination of ozone densities at and below the peak. As panel b of Fig. 5.4 indicates, the ozone retrieval error is smaller than about 5 % between 15 and 40 km if the aerosols extinction profile is known to within a factor of 2. If one assumes that the actual stratospheric aerosol extinction coefficient profile can be estimated to within a factor of 2, then the relative difference between the retrieved ozone densities for 1 × POAM and 2 × POAM can be considered a measure of the systematic errors introduced by incorrect knowledge of the stratosphere's aerosol loading.

A further stratospheric aerosol sensitivity test was performed for enhanced stratospheric or *moderate volcanic* aerosol. This was modelled as 5 × POAM, and an Henyey-Greenstein ($g = 0.7$) phase function. The relative retrieval errors for moderate volcanic aerosols listed in Table 5.2 correspond to the case that the actual stratospheric aerosol loading is moderately volcanic, yet the retrieval is performed assuming stratospheric background aerosol, *i.e.* 1 × POAM. If it is known that the actual aerosol loading is moderately volcanic then the relative retrieval errors are significantly smaller. It should be mentioned that the retrieval error due to insufficient knowledge of the correct stratospheric aerosol loading is negligible above the stratospheric aerosol layer.

Stratospheric aerosols are the most important source of systematic errors of the retrieved ozone density profiles. This is due to the fact that the aerosols appear in the field of view. Roughly speaking, the ozone retrieval method described in Chapter 4 is relatively insensitive to phenomena not appearing in the FOV of the Optical Spectrograph.

5.1.4 Atmospheric density profile

To investigate the sensitivity of ozone retrievals to the background atmosphere two tests were performed, where measurements were simulated with LIMBTRAN for different scenarios (SZA = 55°, 60°, ..., 90°, $\Delta\phi = 90°$, A = 0.5, stratospheric background aerosols (MODTRAN), no clouds) and retrievals were carried out

with an incorrect background atmosphere. By background atmosphere we mean atmospheric profiles of temperature, N_2 and O_2 density. For the first test the atmospheric temperature profile was perturbed by $\pm$ 10 K while the pressure at each altitude was held constant, leading to a background density perturbation. Retrievals were carried out for SZA $\in [55°, 90°]$ and the differences in the ozone column between 15 and 40 km were smaller than 0.5 % for all SZAs. The relative differences $([O_3]^{retrieved} - [O_3]^{true})/[O_3]^{true}$ are smaller than 2 % at all altitudes within the range from 15 to 40 km.

A second sensitivity test was carried out with entirely different background atmospheres. The retrieval vector $\mathbf{y}_C(TH_i)$ was calculated with LIMBTRAN using an equatorial summer (EQ-SU) atmosphere (July 15, 2000, 12:00 LST, Latitude: 0°, Longitude: 0°) obtained from the MSIS 90-E model [*Hedin*, 1991]. A recovery of the ozone density profile was then performed assuming a polar winter (POL-WI) atmosphere (December 21, 2000, 12:00 LST, Latitude: 90°, Longitude: 0°) also obtained from MSIS 90-E. The neutral densities of the EQ-SU and the POL-WI atmospheres differed by up to 50% in the altitude range between 10 km and 40 km. This difference may be unrealistically high, *i.e.*, it presents, if anything, a more stringent test of the method's sensitivity to the background density profile. The maximum error in ozone density for altitudes below 38 km is 3.1 % and the error in the ozone column between 10 km and 38 km is only 0.89%.

This indicates that the ozone profile retrieval method is robust and very insensi-

tive to the background atmosphere. This is again a direct consequence of combining the limb radiance profiles at 602 nm, 532 nm and 672 nm to the Chappuis retrieval vector $\mathbf{y}_C(TH)$. Roughly speaking, limb radiances at all three wavelengths are affected in a similar way by enhanced Rayleigh scatter due to increased density.

5.1.5 Temperature dependence of ozone cross sections

An advantage of the ozone retrieval method applied here is that the ozone absorption cross section in the Chappuis bands is only weakly dependent on temperature. At $\lambda = 672$ nm, a wavelength lying within the Wulf bands, the absorption cross section is slightly more temperature dependent (see Fig. 2.3 in section 2.3). According to *Burrows et al.* [1997], a temperature change from 241 K to 202 K corresponds to an 8.0 % increase of the GOME FM ozone cross section. At $\lambda = 532$ nm and $\lambda = 602$ nm, the cross sections increase by 1.57 % and 1.49 %, respectively, if the temperature changes from 241 K to 202 K. Chappuis retrieval vectors (for SZA = 70°, $\Delta\phi = 90°$) were simulated for (a) an isothermal atmosphere with T = 202 K, (b) a tropical temperature profile and T-dependent ozone cross sections, and retrievals were performed assuming T = 202 K, T = 241 K, and T = 273 K for the cross sections. The relative retrieval error never exceeded 1.0 % for altitudes ranging from 15 to 40 km.

5.1.6 Clouds

Tropospheric clouds affect limb radiance profiles by enhancing the radiance. Similar to the SZA dependence of the impact of ground albedo on limb radiance profiles (see section 5.1.1), the impact of clouds on limb radiance profiles decreases with increasing SZA.

Assume that the impact of clouds on the limb radiance profile $I(TH, \lambda)$ at wavelength λ can be modelled as

$$I_{cloud}(TH, \lambda) = I_{cloud-free}(TH, \lambda) \times C(TH, \lambda) \tag{5.1}$$

where $C(TH, \lambda)$ is the wavelength and TH dependent *cloud correction factor*. The normalization (section 4.1.4) then leads to:

$$I^n_{cloud}(TH, \lambda) = \frac{I_{cloud}(TH, \lambda)}{I_{cloud}(TH_{ref}, \lambda)} = \frac{I_{cloud-free}(TH, \lambda) \times C(TH, \lambda)}{I_{cloud-free}(TH_{ref}, \lambda) \times C(TH_{ref}, \lambda)} \tag{5.2}$$

$$= I^n_{cloud-free}(TH, \lambda) \times C^n(TH, \lambda)$$

With equation 5.2 it is easily shown that the following separation of the cloud-free Chappuis retrieval vector from a *cloud correction vector* $\zeta_{\text{cloud}}(\text{TH})$ is possible:

$$\mathbf{y}_C(TH) = \frac{I^n_{cloud}(\lambda_2, TH)}{\exp[\frac{1}{2}(\ln I^n_{cloud}(\lambda_1, TH) + \ln I^n_{cloud}(\lambda_3, TH))]} \tag{5.3}$$

$$= \frac{I^n_{cloud-free}(\lambda_2, TH)}{\exp[\frac{1}{2}(\ln I^n_{cloud-free}(\lambda_1, TH) + \ln I^n_{cloud-free}(\lambda_3, TH))]} \times \zeta_{\text{cloud}}(TH)$$

with the cloud correction vector $\zeta_{\text{cloud}}(TH) = \frac{C^n(\lambda_2, TH)}{\exp[\frac{1}{2}(\ln C^n(\lambda_1, TH) + \ln C^n(\lambda_3, TH))]}$ having the same form as the cloud-free Chappuis retrieval vector. The wavelengths

are: $\lambda_1 = 532$ nm, $\lambda_2 = 602$ nm, and $\lambda_2 = 672$ nm. The cloud correction vector $\zeta_{\text{cloud}}(TH)$ was determined with MODTRAN 3 for (a) a reference scenario without tropospheric clouds, (b) cumulus clouds (Cu) ranging from 600 to 3000 m, (c) altostratus clouds (As) extending from 2400 to 3000 m and (d) stratus (St) clouds between 300 and 1000 m and SZA of 60° and 85°. At SZA = 60° the limb radiances increase by up to 60 % in the 10 to 50 km altitude range if clouds are present. Fig. 5.5 illustrates the impact of clouds on limb radiance profiles at the three wavelengths used. For SZA = 85° the change in limb radiances is less than 10 % in the same altitude range if clouds are introduced.

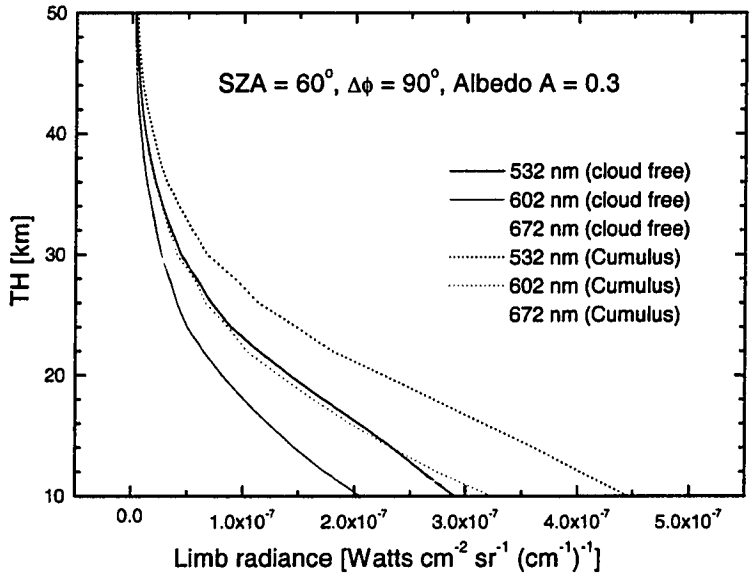

Figure 5.5: The effect of tropospheric clouds on the limb radiance profiles at the wavelengths used for ozone profile retrieval modelled with MODTRAN 3.

The difference in retrieved ozone density between the cloud free reference sce-

nario (a) and a cloudy troposphere is a measure of the systematic impact of clouds on the retrieval, if clouds are entirely ignored. For SZA = 60° the retrieval error is less than 2.5 % at 15 km altitude for all cloud types studied and increases roughly linearly to 4.9 % at 35 km altitude. The retrieved ozone densities are systematically smaller than the true values. At SZA = 85° the retrieved ozone densities underestimate the correct ozone profile by 2.5 % at 15 km and overestimate it by 5.2 % at 35 km. Between 15 and 35 km the change is roughly linear.

We find that tropospheric clouds do not have a major impact on the retrieved ozone density profiles, although the retrieval errors, if clouds are ignored, are greater than the ones reported by *Flittner et al.* [2000] (< 1 %).

A possible way to reduce the systematic error introduced if tropospheric clouds are ignored or incorrectly modelled, would be to use global maps of daily reflectivity (as say measured with EP-TOMS) and assume climatological and latitude-dependent cloud altitudes. This would, however, slow down the ozone profile retrievals significantly. For the ozone density retrievals presented in the following Chapters clouds were not taken into account.

5.1.7 Internal scattering

Internal stray-light arises from the scattering of light inside the optics unit, *i.e.* cross talk between wavelengths that are separated by the spectrograph's grating. Internal scattering is of much greater importance for wavelengths shorter than

about 340 nm, where the limb radiances are limited by the large LOS optical depths at lower THs due to ozone absorption and Rayleigh extinction. For example, at 305 nm the limb radiance profile assumes a maximum at a TH of 44 km, as discussed in section 4.1.2. However, the observed OSIRIS limb radiance profile at this wavelength exhibits a minimum value below a knee at about 35 km, and below the minimum the limb radiances increase with decreasing TH. This can be explained by the internal stray-light from longer, optically thin wavelengths for which the limb radiance continues to increase with decreasing TH. At $\lambda < 300$ nm and TH < 20 km the internal scattering contamination can exceed 100 % of the actual signal. This does not pose a problem for most OSIRIS applications, because the limb radiances do not contain much information at lower THs anyway, due to the large LOS optical depths. Although important for the UV spectral range, simulations showed that the internal scattering contamination corresponds to up to 1 % of the signal in the visible part of the spectrum.

Internal scattering correction algorithm

Evans and Alfred [2001] characterized the internal scattering contamination and spectral cross talk of the Optical Spectrograph and devised an algorithm to correct for contamination due to internal scattering. The algorithm integrates in wavelength over the entire dark current and DC-bias corrected observed spectrum and the internal scatter contamination for each pixel is then determined by multiplying

the resulting integral with a constant value, *i.e.* the so called *internal scattering correction factor* γ:

$$I_{int} = \gamma \times \sum_{i=1}^{1353} I_i \tag{5.4}$$

where I_{int} is the modelled internal scatter contamination received by each pixel and I_i is the dark current and DC-bias corrected, but not responsivity corrected signal in CCD pixel i. Observed spectra are corrected for internal scattering by subtracting I_{int} from each radiance I_i. Obviously the *Evans and Alfred* [2001] algorithm assumes a pixel (*i.e.*, wavelength) independent internal scattering contamination. Furthermore, the algorithm is based on the assumption that the internally scattered photons can be represented by a fixed fraction of the photons received at each CCD pixel and are equally distributed over all pixels. This renders a responsivity correction of the internally scattered photons unnecessary.

Evans and Alfred [2001] obtained a γ-factor that lies within the range 3.0×10^{-6} to 5.0×10^{-6} for the OSIRIS FM (flight model) based on calibration measurements made at the University of Calgary. These values are slightly higher than γ-factors determined with the OSIRIS development model of $(2.4 \pm 0.9) \times 10^{-6}$ [*Marshall*, 1996]. *Haley et al.* [2001a] used in-flight data to determine the γ factor assuming the *Evans and Alfred* [2001] model and obtained a value of $\gamma = (2.51 \pm 0.05) \times 10^{-6}$. This value has been used for the internal scattering correction of all retrievals carried out in this study.

Adding internally scattered light (with $\gamma = 2.51 \times 10^{-6}$) to simulated limb

radiance profiles and performing a retrieval without internal scattering correction resulted in retrieval errors of less than 0.7 % for the 15 - 40 km altitude range.

5.1.8 Polarization

Description of polarized electromagnetic radiation

The most convenient way to treat polarized radiation is to use the *Stokes vector* [*e.g.*, *Stephens*, 1994], $\mathbf{I} = [I, Q, U, V]^T$, a four-element vector. Here, I corresponds to the total radiance, Q is a measure for the radiance linearly polarized parallel and perpendicular to a reference plane, U is a measure for the radiance linearly polarized at 45° and 135° with respect to the same reference plane and V is the circularly polarized radiance[1]. The reference plane for the limb geometry is the meridian plane defined by the local vertical and the LOS. The degree of linear polarization LP is defined by

$$LP = \frac{\sqrt{Q^2 + U^2}}{I} \tag{5.5}$$

Polarization sensitivity of the Optical Spectrograph

Limb scattered solar radiation will generally be linearly polarized and the degree of polarization will be a function of TH. The only cases without linear polarization are forward and backward scattering, *i.e.* scattering angles of $\Theta = 0°$ and $\Theta = 180°$. The polarization of the radiation measured by OSIRIS will affect the retrieved

[1]The fraction of circularly polarized solar radiation is < 1 % [*Hansen and Travis*, 1974]

ozone density profile, if the instrument's radiance response is polarization sensitive. In this case the detected radiances will be altered during the measurement process depending on the polarization state of the radiation and the instrument's polarization sensitivity. The radiance response of the Optical Spectrograph is in fact polarization sensitive and most of the polarization sensitivity is introduced by the diffraction grating. Unlike other satellite-based spectrometers (*e.g.*, SCIAMACHY and GOME) OSIRIS is not equipped with a polarization measurement device (PMD). *McLinden et al.* [2002b] (a) characterized the polarization sensitivity of the Optical Spectrograph based on laboratory measurements performed at the University of Calgary, and (b) devised a polarization correction scheme applicable to minor constituent retrievals using DOAS.

Generally, only the Q-sensitivity of grating spectrographs is considered, yet *McLinden et al.* [2002b] found better agreement with the laboratory measurements if a U-sensitivity is allowed for, particularly at the shortest wavelengths covered by the Optical Spectrograph. The relationship between the true atmospheric Stokes vector $\mathbf{I}_{true}(\lambda)$ (*i.e.*, before the measurement process takes place), and the observed total radiance $I_{obs}(\lambda)$ that includes the measurement process, is given by (the V_{true} component is neglected):

$$I_{obs}(\lambda) = f(\lambda) \begin{bmatrix} 1 \\ g_{12}(\lambda) \\ g_{13}(\lambda) \end{bmatrix} \begin{bmatrix} I_{true}(\lambda) \\ -Q_{true}(\lambda) \\ -U_{true}(\lambda) \end{bmatrix} = f(\lambda) \left[I_{true}(\lambda) - g_{12}(\lambda) Q_{true}(\lambda) - g_{13} U_{true}(\lambda) \right] \tag{5.6}$$

The signs appearing in the true atmospheric Stokes vector are introduced by the $\pi/2$-rotation from the reference plane to a plane parallel to the grating grooves. The wavelength dependent function $f(\lambda)$ corresponds to the instrument's flat-field response, and g_{12} and g_{13} describe the dependence of the instrument's radiance response on the linear polarization Stokes vector elements $Q_{true}(\lambda)$ and $U_{true}(\lambda)$.

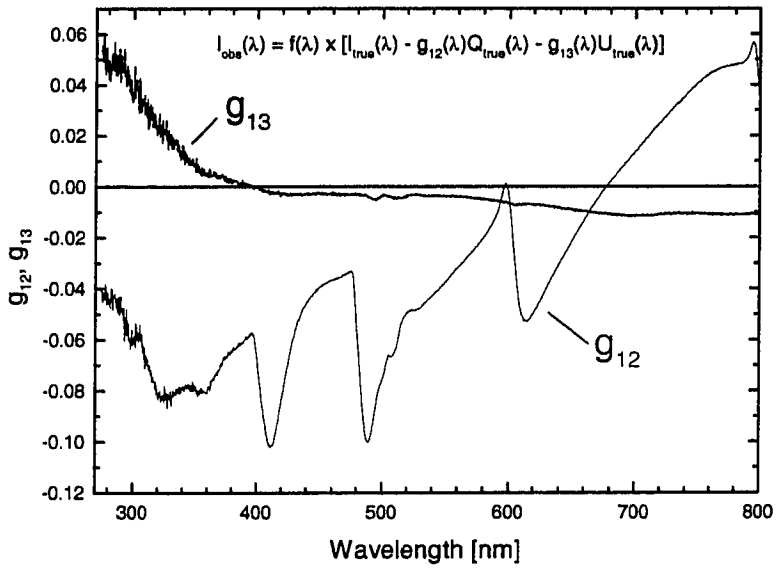

Figure 5.6: The OSIRIS polarization correction coefficients g_{12} and g_{13}.

Figure 5.6 shows the grating efficiency coefficients g_{12} and g_{13} as determined by *McLinden et al.* [2002b]. If $Q_{true}(\lambda)$ and $U_{true}(\lambda)$ can be modelled with reasonable accuracy a polarization correction can be achieved by multiplying the observed radiance spectrum with a correction factor spectrum $C(\lambda)$ given by

$$C(\lambda) = 1 - g_{12} \times \frac{Q_{true}(\lambda)}{I_{true}(\lambda)} - g_{13} \times \frac{U_{true}(\lambda)}{I_{true}(\lambda)} \tag{5.7}$$

As in the case of the impact of clouds on the Chappuis retrieval vector (section 5.1.6) a separation of the observed Chappuis retrieval vector $\mathbf{y}_{obs}(TH)$ into the *true* atmospheric Chappuis vector $\mathbf{y}_{true}$(TH) and a *polarization correction vector* $\zeta_{pol}(TH)$ is possible:

$$\mathbf{y}_{obs}(TH) = \mathbf{y}_{true}(TH) \times \zeta_{pol}(TH) \tag{5.8}$$

with the polarization vector having the same mathematical form as the Chappuis retrieval vector:

$$\zeta_{pol}(TH) = \frac{C^n_{pol}(TH, \lambda_2)}{\exp[\frac{1}{2}(\ln C^n_{pol}(TH, \lambda_1) + \ln C^n_{pol}(TH, \lambda_3))]} \tag{5.9}$$

Here, $C^n_{pol}(\lambda, TH)$ corresponds to the normalized correction factor similar to the one defined in eqn. 5.1.6 for the effect of clouds.

This section presents an estimation of the systematic error introduced if the polarization sensitivity of the instrument's radiance response is ignored. Two different cases are studied: (a) a pure Rayleigh atmosphere and (b) an atmosphere with stratospheric background aerosol.

Since LIMBTRAN is not capable of solving the RT equation for the full Stokes vector the vertical profiles of the degree of linear polarization were determined with the *McLinden et al.* [2002a] model, while the recoveries were carried out using LIMBTRAN.

The polarization state of the detected scattered radiation depends on SZA and $\Delta\phi$, and therefore on the location of the tangent point and on the date. To take pos-

Scenario	Day of year	Location of sub-tangent point	SZA	$\Delta\phi$	Θ
1	June Solstice	Ascending Equator	90.0°	58.7°	58.7°
2	June Solstice	Highest Latitude	58.7°	90.0°	90.0°
3	June Solstice	Descending Equator	90.0°	121.3°	121.3°
4	September Equinox	Ascending Equator	90.0°	82.3°	82.3°
5	September Equinox	Highest Latitude	82.3°	90.0°	90.0°
6	September Equinox	Descending Equator	90.0°	97.7°	97.7°
7	Terminator	Ascending Equator	90.0°	90.0°	90.0°
8	Terminator	Highest Latitude	90.0°	90.0°	90.0°
9	Terminator	Descending Equator	90.0°	90.0°	90.0

Table 5.1: Summary of the scenarios used for the polarization sensitivity study. Θ is the (SS) scattering angle ($\cos(\Theta) = \sin(SZA) \times \cos(\Delta\phi)$ for limb geometry).

sible variations due to different viewing geometries into account, simulations were carried out for three days: June solstice, September equinox and the terminator days (see Table 5.1). On the two terminator days Odin flies along the terminator and the ground track of the tangent point coincides with the terminator throughout the ideal orbit. On each of the three chosen days three satellite positions are considered: (a) when the tangent point crosses the equator from south to north (18:00 LST); (b) at the highest northern latitude of the orbit (12:00 LST); and (c) when the tangent point crosses the equator from north to south (06:00 LST). The parameters of each viewing geometry are listed in table 5.1. The albedo was assumed to be 0.30 for all scenarios.

Pure molecular atmosphere

First, stratospheric aerosols were ignored, and the impact of the instrument's polarization sensitivity was estimated for a pure Rayleigh scattering atmosphere. It was found that the elements of the polarization correction vector were within the range 1 ± 0.00031 for all tangent heights and observation geometry scenarios listed in Table 5.1. The simulated retrieval errors for all scenarios listed in Table 5.1 were less than 0.07 % for the altitude range 15 to 40 km. The impact of the Optical Spectrograph's polarization sensitivity for a pure molecular atmosphere can therefore be neglected. Note that the individual (not normalized) correction factors $C(TH, \lambda)$ partly deviate from 1 by several %. Yet, they exhibit very little TH dependence and thus the normalization of the limb radiance profiles removes the polarization sensitivity almost entirely. This is not true for an aerosol loaded stratosphere, which leads to a more pronounced TH dependence of the $LP(TH, \lambda)$ and therefore the $C(TH, \lambda)$ profile.

Stratospheric background aerosol

For stratospheric background aerosol the linear polarization elements of the Stokes vector exhibit a slightly larger TH dependence than in the case for the pure molecular atmosphere. The associated retrieval errors are smaller than about 0.25 % for all scenarios throughout the 15 to 40 km altitude range. Thus, even for stratospheric background aerosols, the instrument's polarization sensitivity is very small

compared to the dominant error sources and is therefore negligible.

5.1.9 Baffle scattering

Baffle scattered radiation is *external stray light* from outside the instrument's FOV (*e.g.*, from the bright limb of the Earth surface). The required rejection of off-axis radiation is a major challenge in the design of a limb viewing instrument. Considering that limb radiances in the visible part of the electromagnetic spectrum change by more than 3 orders of magnitude (see Fig. 3.7 in Chapter 3) during a limb scan, the off-axis signal rejection has to be very good.

Llewellyn and Gattinger [1998] estimated the OSIRIS in-flight baffle scattering contamination based on laboratory measurements at three wavelengths (*i.e.*, 400 nm, 550 nm and 700 nm) for THs of 25 km, 40 km and 70 km. At longer visible wavelengths and high tangent heights the estimated baffle scattering contamination can reach several 100 % of the true signal, *e.g.*, 440 % at 700 nm and TH = 70 km.

In the following, the impact of baffle scattering on the retrieved ozone density profiles will be estimated based on the findings of *Llewellyn and Gattinger* [1998]. The baffle scatter contamination as a percentage of the true signal increases exponentially with TH at all three wavelengths. Moreover, the wavelength dependence of the baffle scatter contamination at a given TH can be very well fitted with a log-polynomial function. Fig. 5.7 illustrates both the exponentially increasing

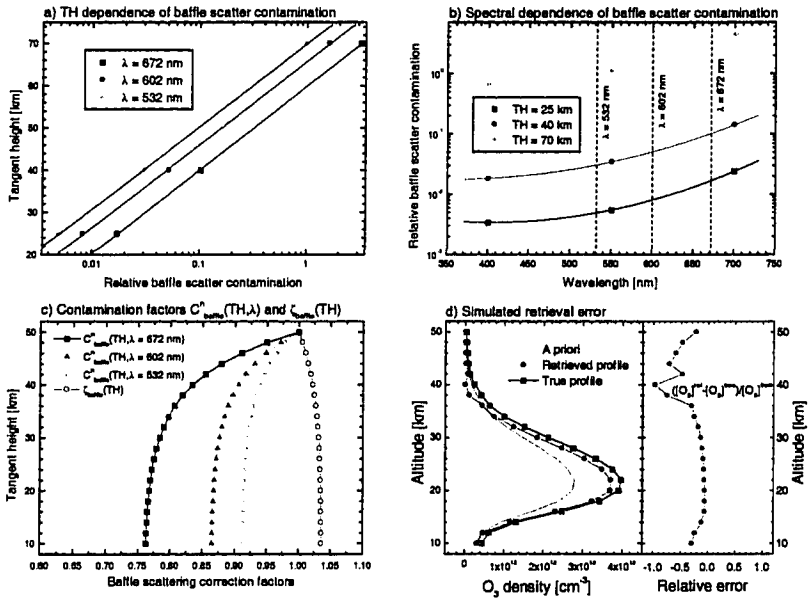

Figure 5.7: Panel a illustrates the exponential dependence of the baffle scatter contamination at the three wavelengths used for the retrievals. The contamination at these wavelengths was obtained by a log-polynomial interpolation (panel b) of the spectral estimated by *Llewellyn and Gattinger* [1998]. The contamination factors $C^n_{\text{baffle}}(TH, \lambda)$ differ quite significantly from 1.0, yet the wavelength pairing leads to a relatively small deviation of $\zeta_{\text{baffle}}(\text{TH})$ from the ideal value, *i.e.* 1.0. Panel d illustrates that the estimated baffle scatter contamination leads to unrealistically large retrieval errors. The simulations were performed for SZA = 58.7°, $\Delta\phi = 90°$, albedo A = 0.3 and stratospheric background aerosols.

contamination (panel a) and the spectral dependence of the contamination (panel b).

To estimate the baffle scattering contamination at 532 nm, 602 nm, and 672 nm at THs of 25 km, 40 km, and 70 km a log-polynomial fit of the contamination at the wavelengths of *Llewellyn and Gattinger* was used. Then, the TH dependence of the contamination at those wavelengths was approximated by a exponential function.

Similar to the normalized cloud and polarization correction factors (C^n_{cloud} and C^n_{pol}) a normalized baffle scatter correction factor $C^n_{baffle}(TH, \lambda)$ was defined. Its TH dependence at the three wavelengths used is shown in panel c of Fig. 5.7. For the longest wavelength ($\lambda = 672$ nm), where the contamination is the largest, significant deviations from the ideal, no contamination value of 1.0 occur. At shorter wavelengths the contamination is smaller. Panel c also shows the baffle scatter correction vector ζ_{baffle}(TH). Due to the wavelength pairing its deviation from the ideal value 1.0 is significantly smaller than for $C^n_{baffle}(TH, \lambda)$ at each of the wavelengths.

The baffle scatter contamination based on the assumptions made here leads to non-negligible retrieval errors (panel d) and to a systematic underestimate of the actual profile. The obtained retrieval errors are unrealistically large, and are not consistent with the excellent agreement of (a) OSIRIS ozone density profiles with POAM III ozone profiles (Chapter 6) an (b) OSIRIS stratospheric columns with EP-TOMS total ozone columns (section 7.2 of Chapter 7).

The analysis indicates that the actual in-flight baffle scatter contamination is smaller than suggested by *Llewellyn and Gattinger* [1998]. This is consistent with the findings of *S. Petelina* (personal communication).

5.1.10 Pointing errors

Inaccurate knowledge of the satellite's pointing direction will lead to systematic errors in the retrieved ozone densities. At best, these errors occur because the retrieved ozone density profile is simply shifted vertically by the error in TH assignment. Above and below the ozone density peak, where the ozone density gradients are large, this will lead to relatively large errors (*i.e.*, tens of percent).

Generally, the retrieved profile will not only be shifted vertically with respect to the true profile, but also distorted in non-trivial ways. For example, retrievals of aerosol density or extinction profiles based on absolute limb radiance profiles, can be very sensitive to pointing errors, with limb radiance gradients (in the optically thin regime) on the order of 15%/km (with 7.5 km scale height). The resulting difference between observed and modelled limb radiance profiles will be wrongly attributed to aerosols.

Due to the use of normalized and paired limb radiance profiles the ozone retrieval method applied here is very insensitive to an incorrect background density (see section 5.1.4). This insensitivity to neutral density means that pointing errors of up to several kilometers will merely result in a vertical shift of the retrieved profile, but not in a additional distortion of the profile.

Odin's nominal pointing accuracy in limb scanning mode is $\pm$ 1.2 minutes of arc [*Berge et al.*, 1997] corresponding to approximately $\pm$ 1 km in terms of tangent height. In staring mode the nominal pointing accuracy is 15 seconds of arc (*i.e.*, 200

m in tangent height). The analysis of in-flight attitude data after the initial phase indicates that the pointing accuracy is higher than expected: generally within ± 15 seconds of arc in limb scanning mode (*U. Frisk*, personal communication). It can therefore be concluded that the effect of the actual pointing errors on the retrieved ozone density profiles is negligible.

The excellent agreement between individual OSIRIS and POAM III ozone density profiles discussed in Chapter 6 also indicates that the attitude accuracy does not negatively affect the ozone profile retrievals.

5.2 Random errors

5.2.1 Instrument noise

The main sources of random measurement error are shot noise, detector dark current correction noise, and detector readout noise. The determination of the errors in the limb radiance profiles employed for the ozone retrievals is based on the Level 0 to 1 processing described by *Haley* [2001c]. The relative measurement errors (standard deviations) associated with the Chappuis retrieval vector are on the order of 2.0 - 3.0 $\times 10^{-3}$ at all THs, and show only little dependence on SZA and $\Delta\phi$. Fig. 5.8 shows an example of the absolute (panel a) and relative (panel b) measurement noise in the Chappuis retrieval vector.

The effect of random measurement error on the ozone profile retrievals was de-

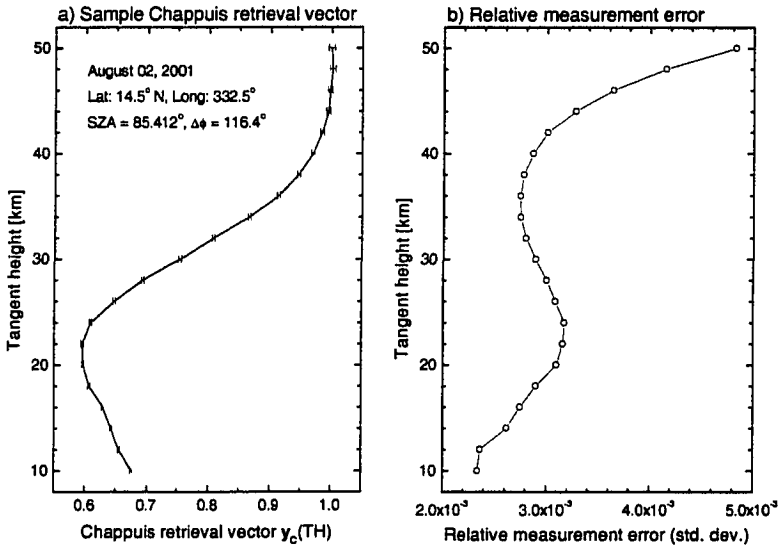

Figure 5.8: Example of the Chappuis retrieval vector error due to random measurement errors.

termined in the following way. A Gaussian random number generator was written (based on the central limit theorem [*e.g.*, *Bronstein and Semendjajew*, 1991]) to create realistic random noise with a TH dependent standard deviation. The standard deviation profile employed for this purpose is the mean observed standard deviation profile for August 20, 2001. The simulated measurement errors $\sigma(TH)$ were added to a simulated Chappuis retrieval vector $\mathbf{y}_C(TH)$ and a retrieval was carried out. This was performed N = 100 times, and the mean difference between the true and retrieved ozone density profiles was determined to estimate the retrieval error due to random measurement errors. The resulting retrieval errors are listed in Table 5.2. The retrieval errors due to random measurement errors could

be reduced by co-adding several pixels near the chosen wavelengths when determining the limb radiance profiles used for the retrievals. For this work only single pixel values were used.

5.3 Summary

A summary of the systematic and random errors in the retrieved ozone density profiles caused by the different geophysical and instrumental parameters discussed in the previous sections of this Chapter is given in Table 5.2.

Altitude	15 km	20 km	25 km	30 km	35 km
Ground albedo[†]	< 3.5%	< 1.5%	< 1 %	< 1 %	< 0.8 %
# of SZAs[§] (see section 5.1.2)	< 1 %	< 0.8%	< 1.2 %	< 0.5 %	< 0.06 %
Stratospheric aerosols[‡] (background)	< 5 %	< 5%	< 5 %	< 0.2 %	< 0.1 %
Stratospheric aerosols[*] (mod. volcanic)	< 25 %	< 16%	< 14 %	< 0.5 %	< 0.4 %
Background atmosphere	< 2 %	< 2%	< 2.5 %	< 2 %	< 2 %
T-dependence of O_3 X-section	< 1%	< 1%	< 1%	< 1%	< 1%
Clouds[&]	< 2.5 %	< 3%	< 3.5 %	< 4 %	< 5 %
Internal scattering[◇]	< 0.5 %	< 0.7%	< 0.7 %	< 0.4 %	< 0.4 %
Polarization [#]	< 0.15 %	< 0.15%	< 0.2 %	< 0.2 %	< 0.1 %
Instrument noise	< 2 %	< 1.3 %	< 1.5 %	< 3 %	< 5%

Table 5.2: Summary of the sensitivity studies.

[†] for SZA $\geq$ 60 °, if albedo known to $\pm$ 0.2

[‡] relative difference between retrieval with 2 × POAM and 1 × POAM

[§] 3 SZAs used for interpolation, SZA $\leq$ 85°

[*] relative difference between retrieval with 5 × POAM and 1 × POAM

[&] if not appearing in FOV

[#] for stratospheric background aerosol, no polarization correction

[◇] if no correction is applied, with correction: < 0.1 %

The total retrieval error can certainly not be considered a simple linear superposition of the errors introduced by the different error sources studied. A more

comprehensive study investigating the combined effects of different error sources would involve a large number of possible combinations and is beyond the scope of the present work. The error budget of the method would be improved if

- global data sets of measured and season-dependent ground albedo values were employed, instead of a constant value of A = 0.3
- daily maps of the global reflectivity as provided by EP-TOMS, for example, were used to identify clouds and the ozone profile retrievals were performed including clouds in the forward model
- daily background atmospheres as determined with the UKMO or ECMWF models, for example, were used
- co-added pixel data were used to determine limb radiance profiles at the required wavelengths

Concluding, it must be noted that the ozone density profile retrieval method described here has been shown to be quite insensitive to all disturbing parameters and processes discussed. Based on the sensitivity studies described here the overall accuracy of the ozone densities in the 15 to 35 km altitude range is estimated to be 10 % or better. Comparisons with EP-TOMS and POAM III ozone measurements (see following Chapters) suggest that this is a very realistic estimate.

Chapter 6

Cross-validation of OSIRIS ozone profiles with POAM III

6.1 The POAM III instrument

The Polar Ozone and Aerosol Measurement III [*Lucke et al.*, 1999], a satellite remote sensing instrument employing the solar occultation technique, was launched in March 1998 into a polar, sun-synchronous orbit on the French SPOT-4 spacecraft. The satellite's orbit has an inclination of 98.9° and the local time of the descending node is 10:30. In the northern hemisphere POAM III makes sunrise observations and in the southern hemisphere sunset observations. Note that POAM orbital sunrises are local sunsets. The latitudes of the POAM III tangent point vary between about 54°N and 70°N in the northern hemisphere and between about 62°S

and 87°S in the southern hemisphere. POAM III has 9 spectral channels between wavelengths of 353.4 nm and 1018 nm, varying in FWHM between 2.1 and 17.7 nm. Its main purpose is the observation of O_3, NO_2, H_2O, and stratospheric aerosols.

Lucke et al. [1999] reported the first validation results, and POAM III was found to overestimate ozone densities between 10 and 35 km in the northern hemisphere (NH) relative to HALOE. In the 15 to 35 km altitude range POAM was systematically 5 % higher than HALOE, and below 15 km the difference increased to $>$ 10 %. Above 30 km the discrepancy decreased with increasing altitude and reached 0 % at 35 km.

More recently, *Rusch et al.* [2001] presented a comprehensive validation study that compared POAM III ozone profiles with profiles derived from both HALOE and SAGE II occultation measurements, as well as from ozone sondes. For the northern hemisphere the agreement with HALOE, SAGE II and the ozone sondes is better than 10 % from 10 - 60 km. Both HALOE and SAGE II comparisons indicate a slope in the POAM bias between 15 and 25 km, increasing from -5 % at 15 km to +5 % at 25 km. According to *Rusch et al.* the POAM III ozone densities are systematically lower than HALOE ozone densities between 20 and 30 km by up to 7 %, as well as SAGE II densities between 20 and 40 km, by 5 %. The number of coincidences in the comparison with HALOE is 183 and with SAGE II it is 122.

Although there are differences between the *Lucke et al.* [1999] and the *Rusch et al.* [2001] assessments (and between comparisons with other instruments), a

general characteristic of all comparisons is that POAM III overestimates the ozone densities by approximately 5 % at least in the 20 - 30 km altitude range, and possibly up to 40 km. Below 15 km, the POAM III ozone densities are significantly higher (> 20 %) than measurements with the other occultation instruments and ECC sondes.

The POAM III data (Version 3) used for the comparison with OSIRIS was taken from the POAM III website (http://www.cpi.com/products/poam/download.html).

6.2 Coincidence criteria

The OSIRIS/POAM coincidence criteria employed in this study are that the measurements were coincident to within 4° in latitude, 6° in longitude and 3 hours in terms of UTC. This is more restrictive than the criteria applied to the early validation of POAM III (5° in latitude, 12° in longitude, 12 hours in time) [*Lucke et al.*, 1999]. The latitudes of the POAM III ozone observations increased from about 57.8°N on August 2, 2001 to about 63.1°N on August 25, 2001, the last day of OSIRIS data collection in August. In total 43 coincidences were found, including 43 OSIRIS ozone profiles and 35 POAM III ozone profiles. Since OSIRIS completes an up or down scan approximately every 5° in terms of latitude at a latitude of 60°, more than one OSIRIS scan may fulfill the coincidence criteria for a given POAM observation. In this case all OSIRIS scans are considered in

the comparison. This explains the larger number of OSIRIS ozone profiles compared to the POAM ozone profiles. The UTC difference of the OSIRIS and POAM III measurements varies slightly around 2.5 hours. The application of the *trajectory hunting* technique [*Danilin et al.*, 2001] in the near future [*A. Tang*, personal communication, 01/2002] will provide many more "effective" coincidences between OSIRIS and other satellite or balloon-borne remote sensing experiments. A trajectory analysis has already been performed at the Free University of Berlin (*Katja Grunow*, personal communication, 2002) for the LPMA/DOAS [*Ferlemann et al.*, 2000] balloon flight that was part of the Odin validation campaign BALODIN in August 2001.

6.3 Comparison

Fig. 6.1 shows the comparison of mean OSIRIS and POAM III ozone density profiles for all coincidences considered (panel a). Also shown is the mean relative difference (OSIRIS - POAM)/POAM (panel b), as well as the standard deviations of all profiles used for both POAM III and OSIRIS (panel c). Obviously the general agreement is excellent, and better than suggested through the sensitivity analysis presented in Chapter 5. Between 15 and 35 km the agreement is better than approximately 5 %. The ozone densities inferred from OSIRIS observations are systematically lower than the POAM ozone profiles at all altitudes between 15 and 40 km.

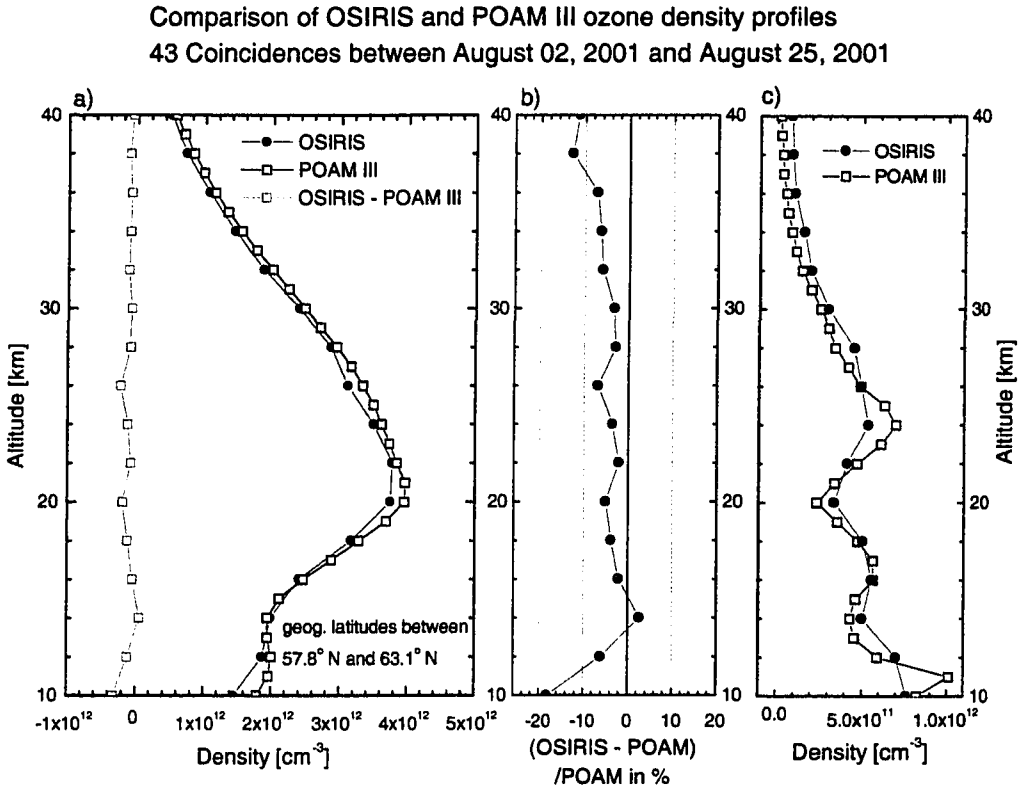

Figure 6.1: Comparison between averaged OSIRIS and POAM III stratospheric ozone density profiles for all coincidences in August 2001. Panel b shows the relative difference as a percentage and in panel c the standard deviation of both the OSIRIS (43) and POAM III (35) profiles are shown).

Due to the different vertical resolution of the two instruments the mean POAM III ozone density profile was convolved with a Gaussian with FWHM = 2 km. Note that convolving the mean is identical to taking the average of individually convolved profiles, since convolution is a linear operation. The correct way to perform comparisons between instruments with different vertical resolution is to convolve the profile of the instrument with the higher resolution with the averaging kernels (see section 4.2.4) of the instrument with the lower resolution [*e.g.*, *Hasekamp and*

Landgraf, 2001]. In the case of OSIRIS the actual vertical resolution is better than 2 km, but due to the vertical undersampling, the instrument is not used to its full capability, and further smoothing occurs. Using a 2 km FWHM Gaussian is somewhat arbitrary, but (a) smoothing is justified, since POAM's vertical resolution is better than OSIRIS'; (b) using a Gaussian with slightly altered FWHM (or even a box-car with variable width) has been found to have little impact on the relative difference between OSIRIS and POAM III.

Note that for comparisons of individual profiles the differences between OSIRIS and POAM can be significantly greater. This is illustrated in Fig. 6.2 showing comparisons of individual ozone density profiles for coincidences on different days in August. 20 coincidences between OSIRIS and POAM III were randomly picked. In most cases the general agreement is very good, indicating that the ozone profile retrieval method described in Chapter 4 is reliable and robust. In some cases the fine structures and laminae present in the POAM III ozone profiles (*e.g.*, panels k, n, o and q) are not recovered in the OSIRIS ozone profiles. This disagreement is not unexpected and may be due to:

- Horizontal variability of the ozone field which can be significant [*e.g.*, *Tuck et al.*, 1999]. This is most likely at mid-latitudes, i.e. about 60°, where the observations were made. Here the zonal and meridional variability of ozone density is greater than at tropical and polar latitudes. In terms of meridional variation, 60°N is close to the latitude with the greatest gradient of

the ozone peak height and latitude (around 55° N for August; see Figs. 7.5 and 7.4). In terms of longitudinal variability 60° N falls within the highly structured transition regime between tropical and polar latitudes, with longitudinal variations of up to 100 DU, and longitudinal gradients of up to 70-80 DU/30°.

- OSIRIS has a vertical resolution that is better than 2 km, yet the limb radiance spectra are sampled only every 2.5 km in stratospheric mode. A direct consequence of this is that small scale features cannot be accurately recovered. It would be desirable to increase the vertical sampling of OSIRIS.

Since POAM III seems to overestimate ozone densities in the 20 - 35 km range by up to 5 - 7 %, according to the comparisons with both HALOE and SAGE II, OSIRIS would seem to agree even better with HALOE and SAGE II. In other words, we might expect the "agreement" of OSIRIS with HALOE and SAGE II to be as good or better than that between OSIRIS and POAM.

It is also noteworthy that the agreement between other satellite instruments measuring stratospheric ozone density profiles is usually in the 5 - 10 % range, and larger differences of mean profiles are not uncommon. For example, ILAS, the Improved Limb Atmospheric Spectrometer [*Suzuki et al.*, 1999], a solar occultation instrument on board the Advanced Earth Observing Satellite (ADEOS), yields stratospheric ozone densities that are up to 20 % lower than HALOE's in the 20 to 40 km altitude range for high southern latitudes with no-ozone-hole conditions.

Moreover, HALOE (Version 17) ozone densities are systematically 5 - 10 % lower when compared to SAGE II data, whereas MLS values are 5 % larger, CLAES densities are 15 % higher and ISAMS values are much more variable [*Cunnold et al.*, 1996].

The comparison of mean ozone density profiles including all coincidences within 4° latitude, 6° longitude and 3 hours of UTC indicates that the OSIRIS ozone density profiles are in excellent agreement with ozone density profiles obtained from POAM III.

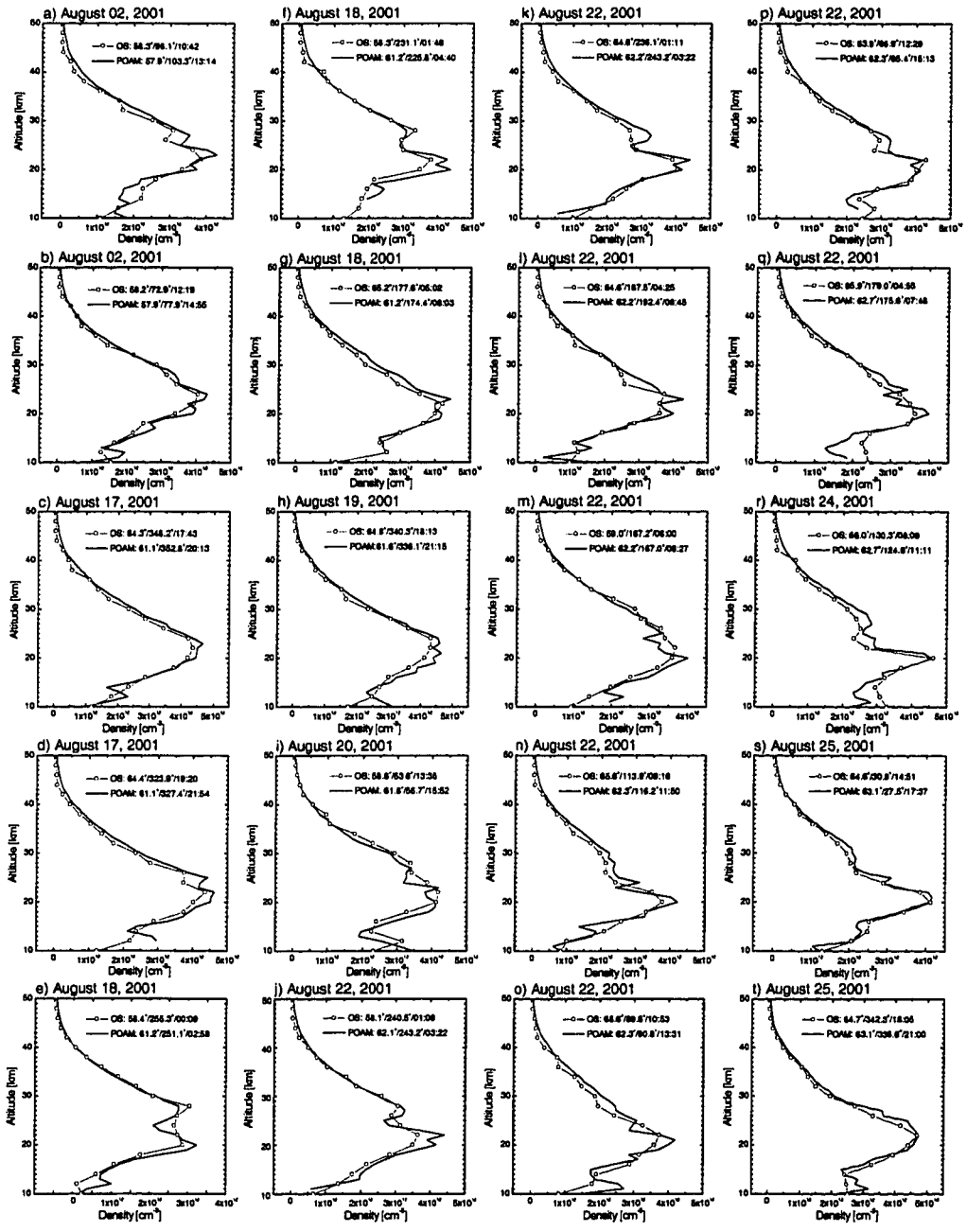

Figure 6.2: The figure shows 20 randomly chosen coincidences of OSIRIS and POAM III northern hemisphere observations during August 2001. Coincidence criteria are 4° in latitude, 6° in longitude, and 3 hours in UTC. The numbers in the legend of each panel correspond to latitude, longitude and UTC. The POAM III profiles are not smoothed.

Chapter 7

A preliminary analysis of OSIRIS observations

This Chapter describes the main characteristics of the stratospheric ozone density fields obtained from OSIRIS observations during August 2001 (northern hemisphere summer) and November 2001 (southern hemisphere spring). The stratospheric ozone column densities determined from the ozone profiles are also compared to total ozone columns measured with the EP-TOMS spectrometer [*McPeters et al.*, 1998].

7.1 A priori ozone profiles

The impact of the *a priori* $\mathbf{x}_0$ on the retrieved ozone density profile was found to be generally negligible. Simulations showed that even if a high latitude ozone profile

for non-ozone hole conditions is used as the *a priori* profile for the recovery of an ozone profile inside the ozone hole, the impact is only on the order of a few percent. This insensitivity is a consequence of the large *a priori* covariance chosen to be 100 % of the *a priori*. For the analyses in the case of non-ozone hole conditions the *a priori* was the zonally averaged 10 year mean August ozone profile from the Canadian Middle Atmosphere Model (CMAM) [*de Grandpré et al.*, 2000]. The *a priori* is latitude dependent and was binned into 5° latitude bins. For recoveries under ozone hole conditions a POAM III ozone hole profile was used.

7.2 NH summer observations and comparison with EP-TOMS

Due to early problems with Odin's attitude control system routine limb scanning did not begin until late July 2001. Most of the northern hemisphere data that can be used for ozone profile retrievals was collected during August 2001. As a consequence of Odin's orbit parameters only the northern hemisphere was observed between July 2001 and the fall terminator day, *i.e.* October 12, 2001 (see Chapter 3).

All data obtained during August 2001 have been analyzed - this represents nearly 3900 individual scans. Table 7.1 gives an overview of the data availability for the days, when OSIRIS was operating. The retrieval of 200 scans (with 3 SZAs

Date mm/dd/yyyy	observation mode	Scan rate [km/s]	Nominal scan range [km]	Number of scans
08/02/2001	stratosph†	0.75	0-10 to 60-70	118
08/03/2001	summermes‡	0.75	70-80 to 90-100	58
08/04/2001	summermes	0.75	70-80 to 90-100	51
08/05/2001	stratosph	0.75	0-10 to 60-70	270
08/06/2001	stratmeso*	0.75	0-10 to 90-100	228
08/07/2001	summermes	0.75	70-80 to 90-100	263
08/08/2001	stratosph	0.75	0-10 to 60-70	219
08/09/2001	stratmeso	0.75	0-10 to 90-100	54
08/11/2001	stratosph	0.75	0-10 to 60-70	28
08/12/2001	stratmeso	0.75	0-10 to 90-100	106
08/14/2001	stratosph	0.75	0-10 to 60-70	108
08/15/2001	stratmeso	0.75	0-10 to 90-100	225
08/17/2001	stratosph	0.75	0-10 to 60-70	109
08/18/2001	stratmeso	0.75	0-10 to 90-100	118
08/19/2001	stratosph	0.75	0-10 to 60-70	108
08/20/2001	stratosph	0.75	0-10 to 60-70	398
08/21/2001	stratosph	0.75	0-10 to 60-70	343
08/22/2001	stratosph	0.75	0-10 to 60-70	342
08/23/2001	stratosph	0.75	0-10 to 60-70	236
08/24/2001	stratosph	0.75	0-10 to 60-70	279
08/25/2001	stratosph	0.75	0-10 to 60-70	372
08/26/2001	stratosph	0.75	0-10 to 60-70	0

Table 7.1: Compendium of data availability for August 2001.

†Stratospheric mode

‡Summer mesospheric mode, particularly observation of PMCs

*Combined stratospheric/mesospheric mode

used in the interpolation (see sections 4.3 and 5.1.2) and 4 iterations of the OE algorithm (section 4.2)) takes about one day on York University's "windcd", a 2 processor (Intel Pentium III, 933 MHz, SMP kernel) machine with 1 GB RAM.

7.2.1 August 20, 2001

August 20 is given special attention, since Odin was scanning almost continuously on this particular day, introducing only a few gaps in the geographical coverage of the observations. 398 limb scans were performed on this day.

Selected orbits

8 orbits on August 20 were chosen, *i.e.*, orbits 2, 3, 5, 6, 8, 10, 11, and 14. The variation of the stratospheric ozone profiles along the orbit tracks is shown in the panels a - h of Fig. 7.1. The segments of the orbits shown begin at a latitude of about 30°N on the upleg, and, going through a westward arc, reach the northernmost point at about 82°N latitude. The tangent point trajectories for all 8 orbits of Fig. 7.1 are shown in Fig. 7.2, superimposed on the NH total ozone column field measured by EP-TOMS on the same day. Each orbit consists of 21 individual profiles. 30°N was chosen as the lowest latitude, since for all orbits shown a 15° latitude gap in Odin data exists south of the scan at about 30°N. The positions of the markers (*i.e.*, circles, squares etc.) in Fig. 7.2 correspond to the average location of the tangent point between tangent heights of 10 and 50 km, and thus

are the locations of the tangent point at a tangent height of 30 km.

The individual orbits in Fig. 7.1 have several common features: (a) the low latitude profiles (profiles 1 and 21 of each orbit correspond to latitudes of about 30°N as indicated in Fig. 7.2) have relatively high ozone peak altitudes (26 - 27 km) and the peak ozone densities are generally higher than at mid- and high-latitudes; (b) going to higher latitudes the peak altitude decreases, reaching about 20 km at the highest latitudes. These features are in excellent agreement with the global morphology of the stratospheric ozone field [*Warneck*, 1988; *Wayne*, 1991].

It is instructive to examine whether the areas with extremely high (around 60°N/30°W) and very low total ozone columns (around 75°N/75°E) in the EP-TOMS data are reflected in the OSIRIS ozone profiles. The area with elevated total ozone columns is crossed by orbit 5 (scan 16), orbit 6 (scans 15 - 17), and orbit 8 (scans 14 - 15). For all three orbits the corresponding cases are associated with local minima in the height of the 2.5×10^{12} cm^{-3} isopleth and also with maxima in the total stratospheric ozone column. These findings are consistent with the known correlation between total ozone column and tropopause pressure [*e.g.*, *Hoinka et al.*, 1996] (see also section 7.2.1). The area with extremely low total ozone columns is crossed by orbit 2 (scans 13 - 14), orbit 3 (scan 13), orbit 6 (scans 8 - 9), and orbit 8 (scan 9). In case of orbits 2 and 3 the low total ozone manifests itself as an increase in the height of the 2.0×10^{12} cm^{-3} isopleth below the ozone peak. For orbits 6 and 8 correlation with the ozone isopleth heights is

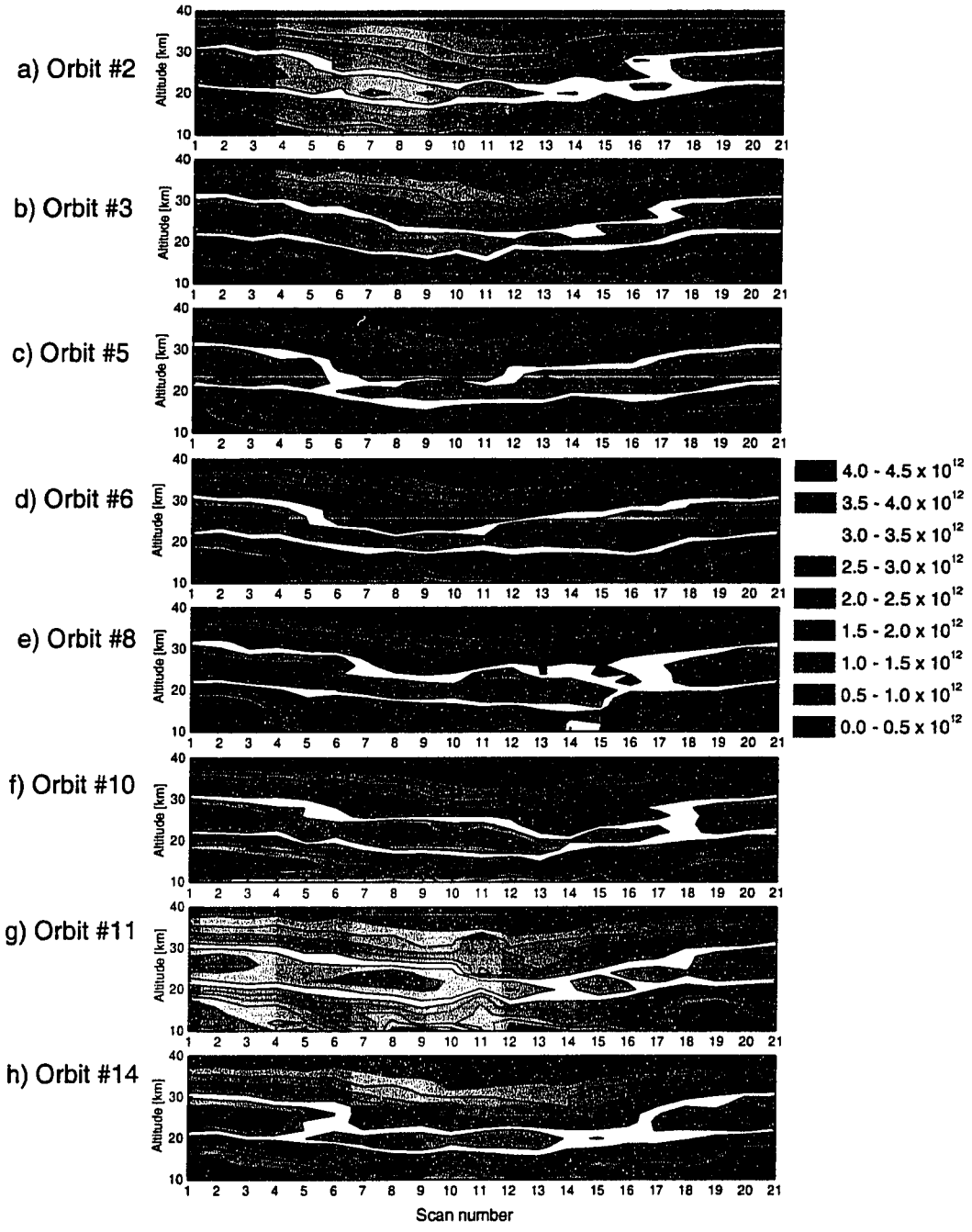

Figure 7.1: The stratospheric ozone field (in molecules cm^{-3}) along the tangent point trajectory for 8 orbits on August 20, 2001, and latitudes north of about 30°N. The tangent point trajectory ground tracks are shown in Fig. 7.2.

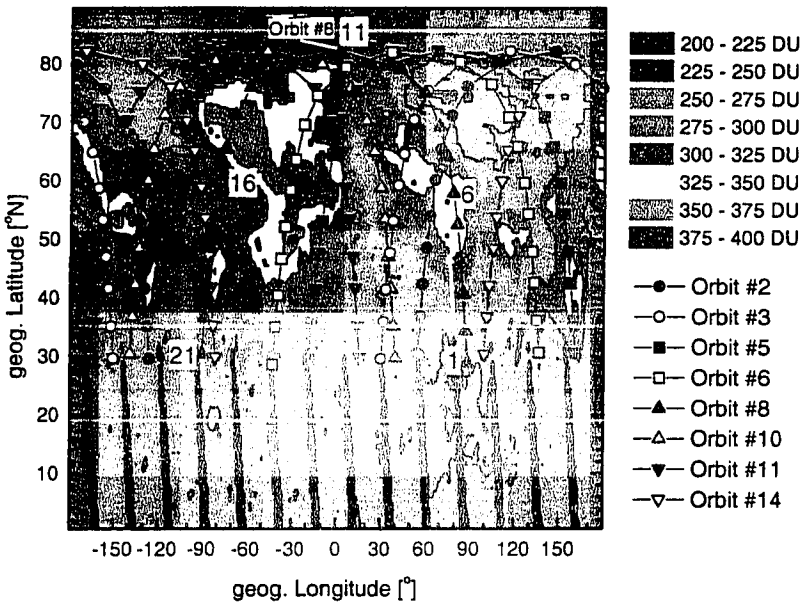

Figure 7.2: The total ozone column distribution on August 20, 2001, for the northern hemisphere as measured by EP-TOMS. Superimposed are the tangent point trajectory ground tracks of the 8 orbits on August 20, 2001 shown in Fig. 7.1.

not obvious, but in case of orbit 6 a narrowing of the ozone peak and a slightly elevated 2.5×10^{12} cm^{-3} isopleth height is discernible.

Longitudinal variation of ozone

A correlation is known to exist between tropopause pressure and the total vertical ozone column [*e.g.*, *Hoinka et al.*, 1996]. Tropospheric low pressure systems are associated with lower than average tropopause heights, and higher than average total ozone columns [*e.g.*, *Warneck*, 1988]. Strictly speaking, the upper tropospheric troughs are displaced westward from the centre of the surface low pressure

system. Tropospheric low pressure systems induce a convergence and subsidence in the mid-stratosphere, forcing ozone rich air downward to the lower stratosphere leading to increased total ozone columns.

Fig. 7.3 shows the longitudinal variation of ozone profiles binned into 15° latitude and 30° longitude bins for August 20, 2001. The figure also shows a comparison of the longitudinal variation of OSIRIS strato-mesospheric ozone columns (a detailed description of how these columns are determined is given in section 7.2.2) with EP-TOMS total ozone columns. The EP-TOMS ozone columns were also binned into 15° latitude bins. Between the equator and 40°N the longitudinal variation of the recovered ozone profiles and also the ozone columns is quite small. At higher latitudes, particularly between 60°N and 75°N, the peak altitude of the ozone layer varies with longitude. The ozone columns from both EP-TOMS and OSIRIS exhibit two local minima and 3 local maxima (wave number 3 pattern) associated with the polar front between mid and polar latitudes. The local minima appear at 90°E - 120°E, and at 240°E. The 2.0×10^{12} cm^{-3} ozone isopleth anti-correlates with the ozone columns, although it should be pointed out that it assumes altitudes as low as 12 km where the retrieval method is less reliable. The 2.5×10^{12} cm^{-3} and 3.0×10^{12} cm^{-3} ozone isopleths anti-correlate with the ozone column as well, but the longitudinal variation is smaller.

It is concluded that the observed anti-correlation of ozone columns and ozone isopleth heights is consistent with the known correlation between tropopause pres-

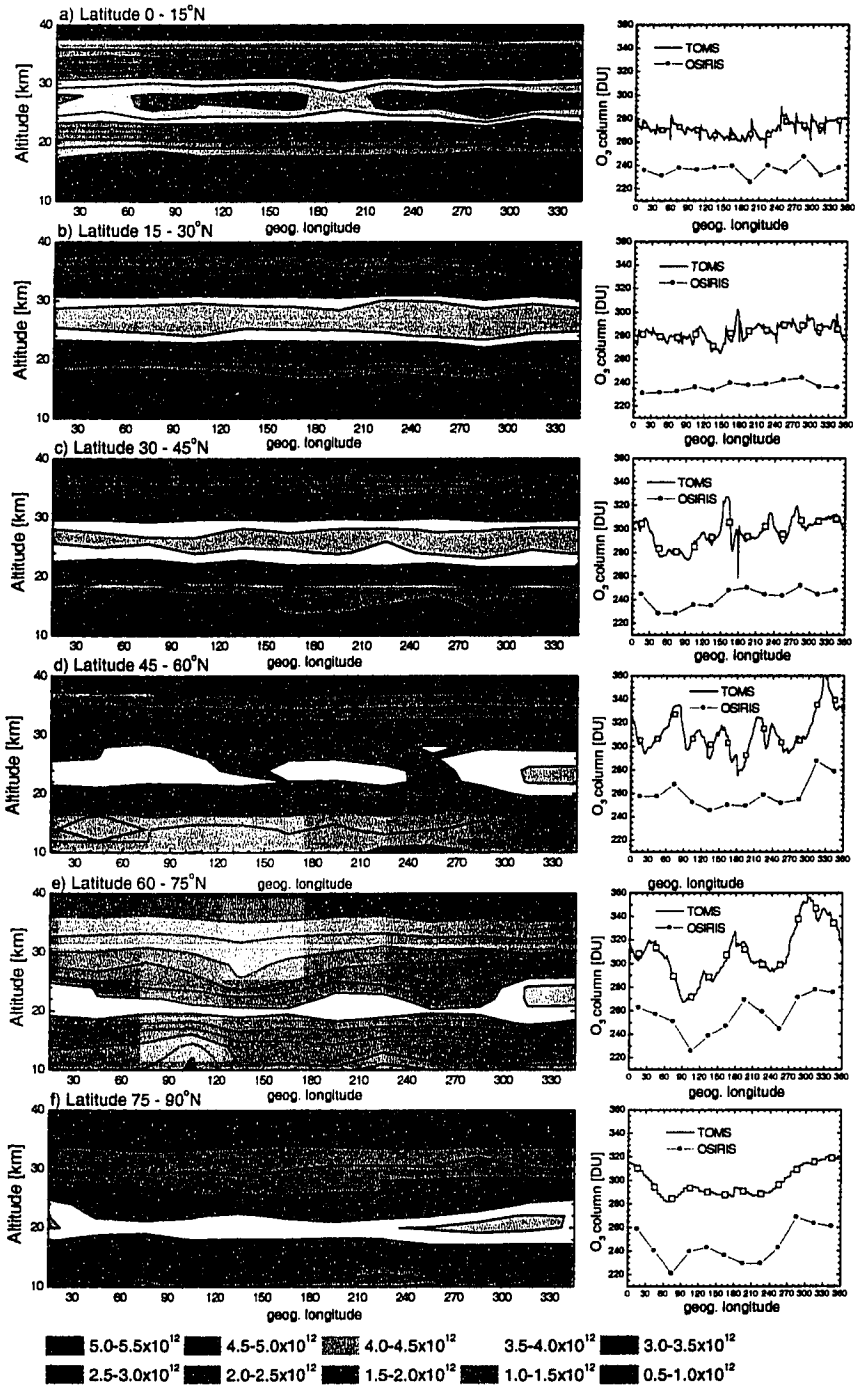

Figure 7.3: Longitudinal variation of latitudinally binned ozone profiles for August 20, 2001.

sure and the total ozone column.

7.2.2 August 2001

Fig. 7.4 shows zonally averaged ozone fields for six consecutive days in August 2001 and Fig. 7.5 shows the latitudinal variation in the zonally averaged ozone profiles derived from the entire August 2001 data base of OSIRIS limb measurements. Clearly, all of the known main features of the stratospheric ozone layer and its dependence on latitude are reproduced: (a) the tropical peak is sharper and appears at an altitude of about 27 km, (b) with increasing latitude the peak descends and widens, and (c) the peak altitude at high latitudes appears at about 20 km.

Fig. 7.4 also shows comparisons of stratospheric and mesospheric ozone columns (inferred from OSIRIS zonally averaged partial stratospheric columns) and total ozone columns measured with EP-TOMS. The difference between the strato-mesospheric and the total ozone columns should correspond to the residual tropospheric ozone column. The EP-TOMS zonally averaged vertical ozone columns were determined from data sets of EP-TOMS ozone columns available from the EP-TOMS website[1]. The strato-mesospheric columns were determined based on the following assumptions:

- OSIRIS ozone profiles are used between the tropopause (TP) and 40 km altitude. Climatological TP heights were obtained from NCEP model anal-

[1]http://toms.gsfc.nasa.gov/

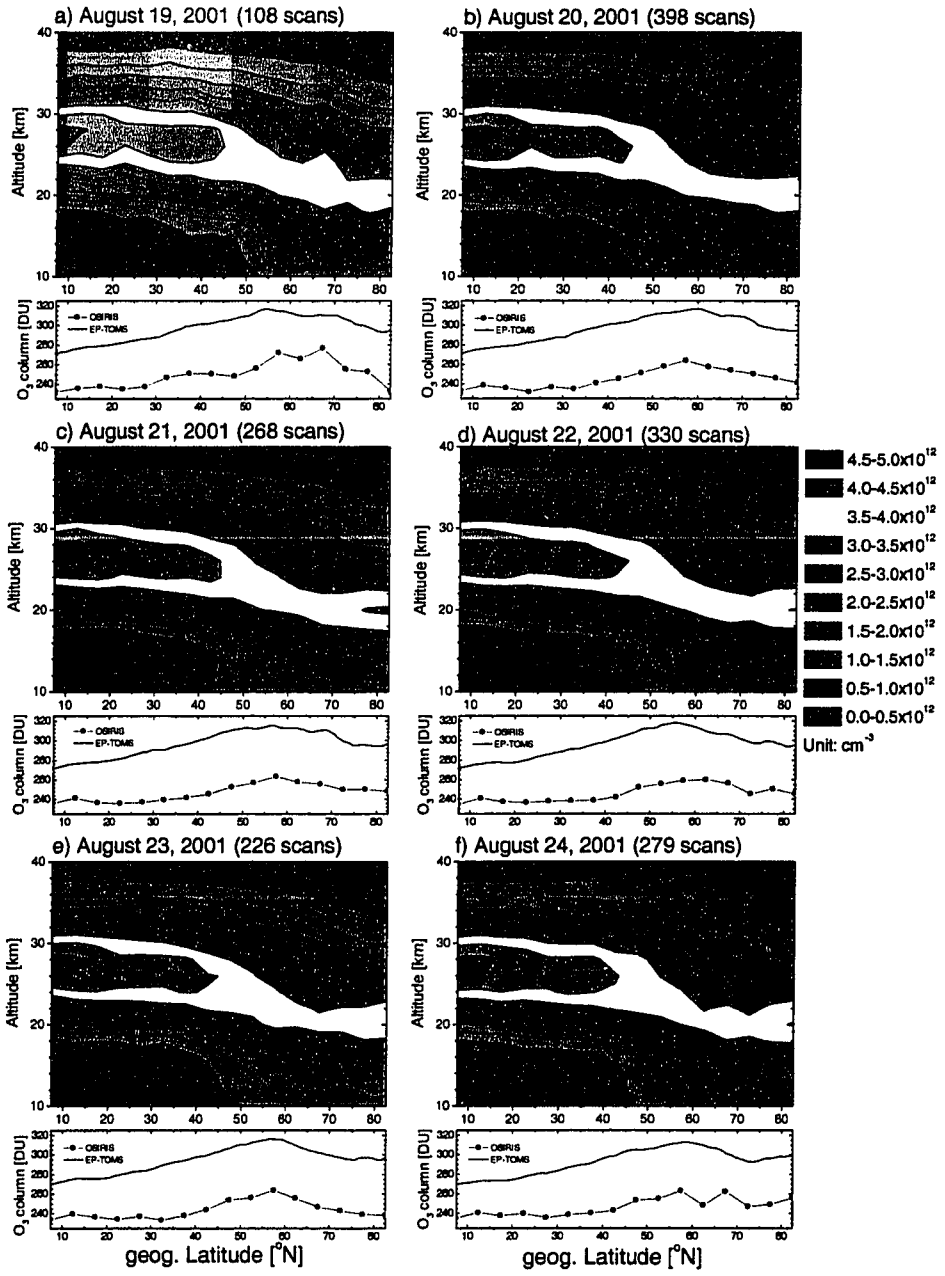

Figure 7.4: Contour plots of the zonally averaged ozone field on six consecutive days in August, 2001. Also shown is a comparison of the latitude dependence of the OSIRIS stratospheric ozone column (plus CMAM mesospheric ozone columns) with total ozone column as measured with EP-TOMS.

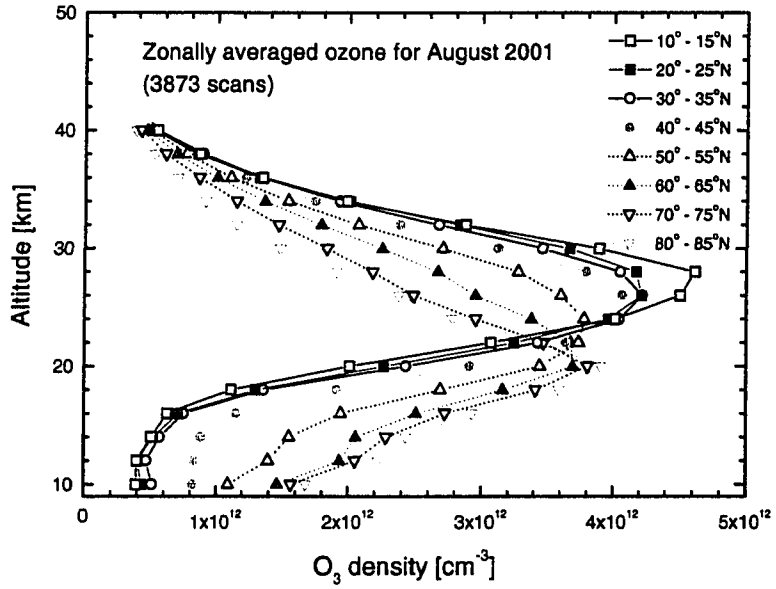

Figure 7.5: Latitude dependence of the zonally and temporally averaged ozone density profile for the August 2001 OSIRIS data set.

yses (40 year August average, from 1958 to 1997) [*Randel et al.*, 2000]. TP heights were determined from TP pressure assuming a ground pressure of p_0 = 1013.25 hPa, and a scale height of H = 7 km, as recommended by *Bill Randel* (NCAR, personal communication). The TP heights used, are listed in Appendix C as a function of latitude. For altitudes below 10 km (the TP height is less than 10 km for latitudes > 60°N) an ozone density of 1.0 × 10^{12} cm^{-3} was assumed.

- Above 40 km CMAM ozone densities are used (note that ozone is not highly variable at these altitudes, and only about 1.5 % or less of the total ozone column occurs above 40 km, including the secondary ozone peak in the meso-

sphere[2])

The retrieval method has been shown to work extremely well in the 15 to 35 km altitude range, with agreement with POAM III to within approximately 5 %. Above 35 km (up to 40 km) the method becomes more insensitive to ozone and the differences between OSIRIS and POAM increase to 10 %. Because the ozone density above 35 km is quite low (5×10^{11} cm^{-3} at 40 km and a scale height of $H_{O_3} \approx 4.5$ km), retrieval errors at those altitudes will have little effect on the partial stratospheric ozone columns. For example, for latitudes between 80°N to 85°N the partial ozone column between 35 and 40 km corresponds to only 4.6 % ($\approx$ 11 DU) of the column between 10 and 40 km for the entire August 2001 NH data set. Between 10°N and 15°N the fraction is about 6.8 % ($\approx$ 16 DU), which is slightly higher due to the higher tropical ozone layer. The figures indicate that a 20 % error in the densities at altitudes between 35 and 40 km will lead to only a 2 - 4 DU difference.

Although the quality of the retrieved ozone densities below 15 km has not yet been established, OSIRIS ozone densities were used if the TP height was less than 15 km. As discussed in Chapter 6 the OSIRIS ozone densities between 10 and 15 km are very realistic, justifying their use for the determination of ozone columns with lower boundaries of less than 15 km. Because the bulk of the atmospheric

[2]This estimate is based on 10 year averages of August ozone profiles determined with CMAM [*de Grandpré et al.*, 2000]

ozone column is above 15 km only small errors should arise if the OSIRIS ozone densities below 15 km are incorrect. Between 10°N and 15°N less than 1 % ($\approx$ 1 DU) of the 10 to 40 km ozone column occurs between 10 and 15 km (based on the August 2001 OSIRIS data set). At 80°N to 85°N this fraction is 17 % ($\approx$ 40 DU). At high latitudes a 20 % error in the ozone densities between 10 and 15 km would lead to column density errors of about 8 DU, which is less than 4 % of the 10 to 40 km ozone column. At low latitudes the error is negligible.

7.2.3 Estimation of tropospheric ozone columns: the residual approach

The idea of determining tropospheric column densities of trace constituents from satellite measurements of stratospheric profiles and total vertical column densities, was first proposed by *Fishman et al.* [1986] and is known as the "residual method". Enhanced tropospheric ozone columns caused by biomass burning in the tropics [*Fishman et al.*, 1986] and large scale air pollution episodes at mid-latitudes [*Fishman et al.*, 1987] are difficult to measure but can be identified using the residual method.

Tropospheric ozone columns have been determined with this method using the OSIRIS strato-mesospheric ozone columns described in the previous section and the EP-TOMS total ozone columns. When clouds are present, EP-TOMS is only able to measure the vertical ozone column above the cloud tops. The EP-TOMS

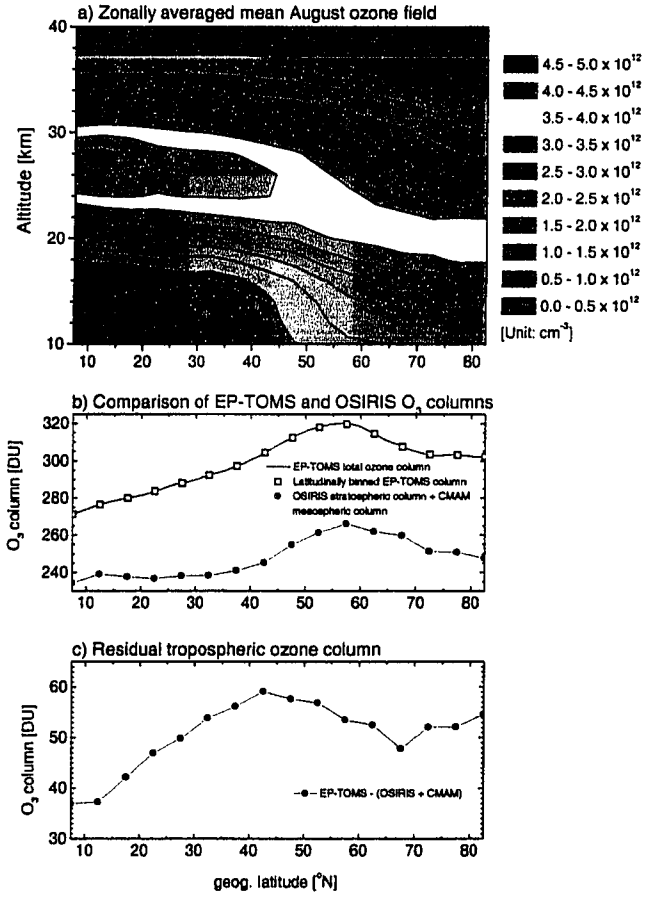

Figure 7.6: Panel a Contour plot of the zonally averaged August 2001 ozone field retrieved from OSIRIS limb radiance profiles. Panel b shows a comparison of EP-TOMS total ozone columns (averaged over all days in August, when OSIRIS was observing) with OSIRIS stratospheric ozone columns (CMAM mesospheric ozone columns added). Panel c shows the residual tropospheric ozone column obtained from TOMS - (OSIRIS + CMAM).

data analysis algorithm estimates cloud top height from the visible reflectance and below this height it uses a climatological distribution to correct for the column of air not observed [*McPeters et al.*, 1998]. *Fishman et al.* [1990] note that a comparison of TOMS data sets with and without cloud screening revealed that cloud screening is not required for the determination of tropospheric ozone column.

Therefore cloud screening is not implemented in the present study.

Fig. 7.6 shows the zonally averaged ozone density field determined from all OSIRIS limb observations performed in August 2001 (panel a), the latitude dependence of the strato-mesospheric ozone column compared to EP-TOMS total columns (panel b) and the inferred tropospheric residual (panel c). The tropospheric residual is approximately 35 DU at 10°N and increases almost linearly to 55 - 60 DU at 40°N. At higher latitudes the tropospheric residuals are between 45 and 55 DU. The lower tropospheric columns at low latitudes reflect the ozone-poor upward branch of the Hadley cell with ozone densities of $< 0.5 \times 10^{12}$ cm^{-3}. At higher latitudes larger tropospheric ozone columns occur as a result of the downward transport of ozone rich air from the stratosphere.

Fishman et al. [1990] report that NH tropospheric ozone columns for the months of June to August are about 20 to 30 DU at the equator and increase to greater than 45 DU at 50°N. These values are based on the analysis of 22,000 TOMS (Nimbus-7) observations coincident with SAGE I (1979 - 1981) and SAGE II (1984 - 1987) measurements. It should be noted that *Fishman et al.* [1990] could only comment on latitudes between 50°S and 50°N. Clearly, the inferred OSIRIS tropospheric ozone column densities are quite consistent with the *Fishman et al.* [1990] value trends up to 50°N and provide important new information on the tropospheric ozone columns at higher latitudes.

It can be concluded therefore that:

(a) the latitude dependence of the derived tropospheric columns between 5°N and 50°N is in excellent agreement with *Fishman et al.* [1990]

(b) the absolute tropospheric columns deduced from OSIRIS and EP-TOMS observations are about 10 - 15 DU higher than the tropospheric ozone columns reported by *Fishman et al.* [1990]

(c) OSIRIS provides reliable information on the trend for latitudes above 50°

It should be noted that the relative errors in the inferred OSIRIS tropospheric ozone columns are quite large, since the tropospheric columns comprise only 10 - 15 % of the total ozone column. The expected errors in the OSIRIS stratospheric ozone profiles and columns are of the same order of magnitude.

7.3 SH Spring observations: the Antarctic Ozone Hole

An integral part of the Odin Aeronomy Mission is to monitor the evolution of stratospheric ozone in polar regions, particularly in the Antarctic ozone hole region. After the mid-October terminator day the southern hemisphere segment of Odin's orbit is sunlit and this makes OSIRIS limb scatter observations possible. Two days of OSIRIS observations towards the end of November 2001 (*i.e.*, 11 orbits on November 24/25 and 13 orbits on November 27/28) have been analyzed in some

detail.

7.3.1 November 24/25, 2001

Fig. 7.7 shows the tangent point trajectories of 11 OSIRIS orbits made on November 24/25, 2001, superimposed on the EP-TOMS total ozone column map. Clearly, the ozone hole is asymmetric in longitude. Also indicated (with blue solid circles) are the locations of POAM III observations for November 24 and 25, when POAM III was measuring at a latitude of 67°S.

Fig. 7.7 also shows how POAM III and OSIRIS observations compare for selected coincidences in both the ozone hole region (POAM observations 160, 161, 167, 170 and 171) and the "collar" region (POAM observations 162 and 163), where ozone densities are enhanced and the total column values exceed 350 DU. This comparison shows that even under "ozone hole" conditions the retrieval method employed here seems to be capable of recovering valid ozone density profiles. More comprehensive validation studies will be required to confirm this conclusion.

Fig. 7.8 shows cross sections through the stratospheric ozone density field along the tangent point trajectories for the 11 orbits of Fig. 7.7. The highest latitude measurements (*i.e.*, $\approx$ 82°S) are marked with black arrows. It is interesting to note the regions of enhanced ozone density in the collar area measured during the up-legs of orbits 5 and 6, and during the down-legs of orbits 10 and 11.

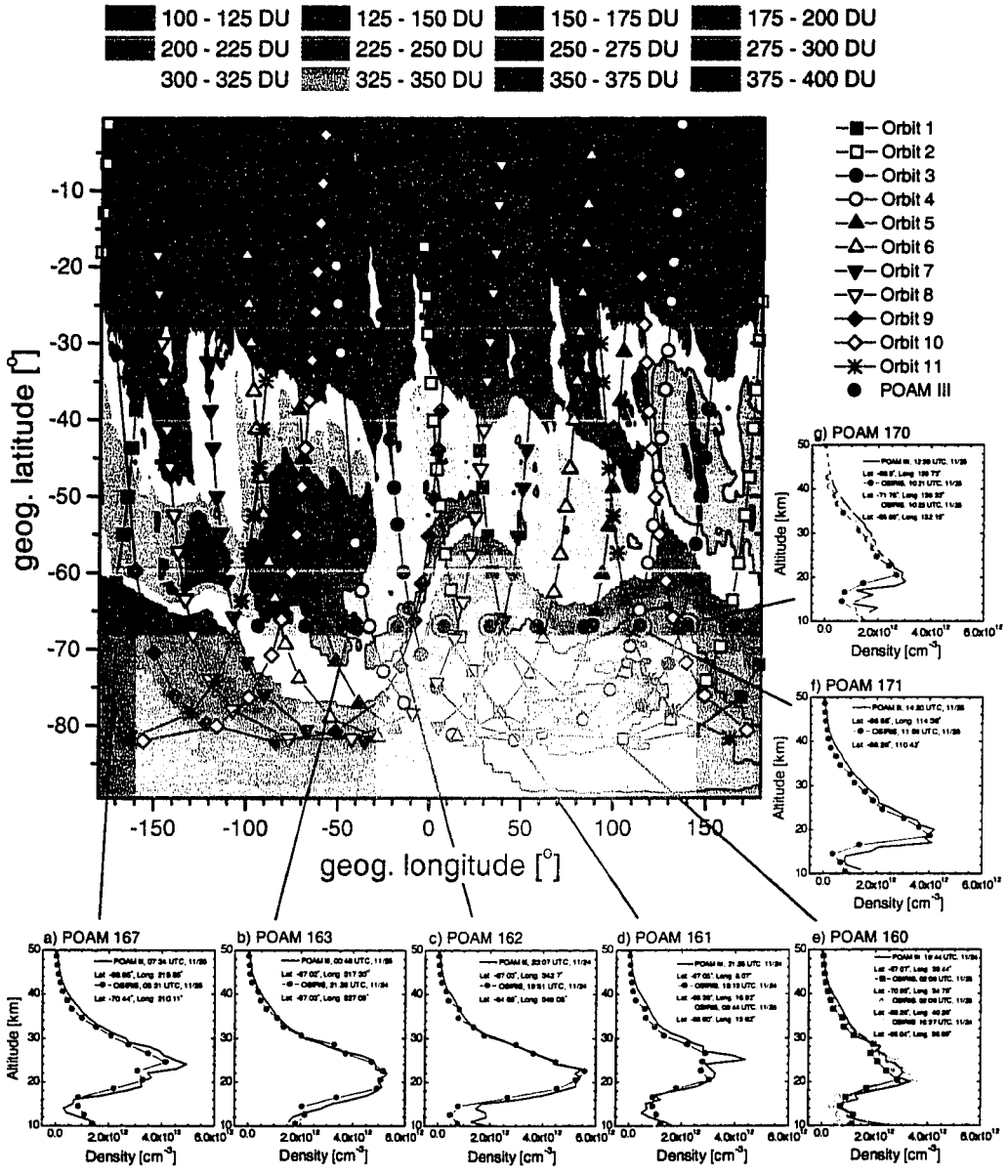

Figure 7.7: The tangent point trajectories of the 11 orbits shown in Fig. 7.8 superimposed to the EP-TOMS total ozone column map are shown. Panels a to g show comparisons of individual OSIRIS ozone density profiles with POAM III profiles.

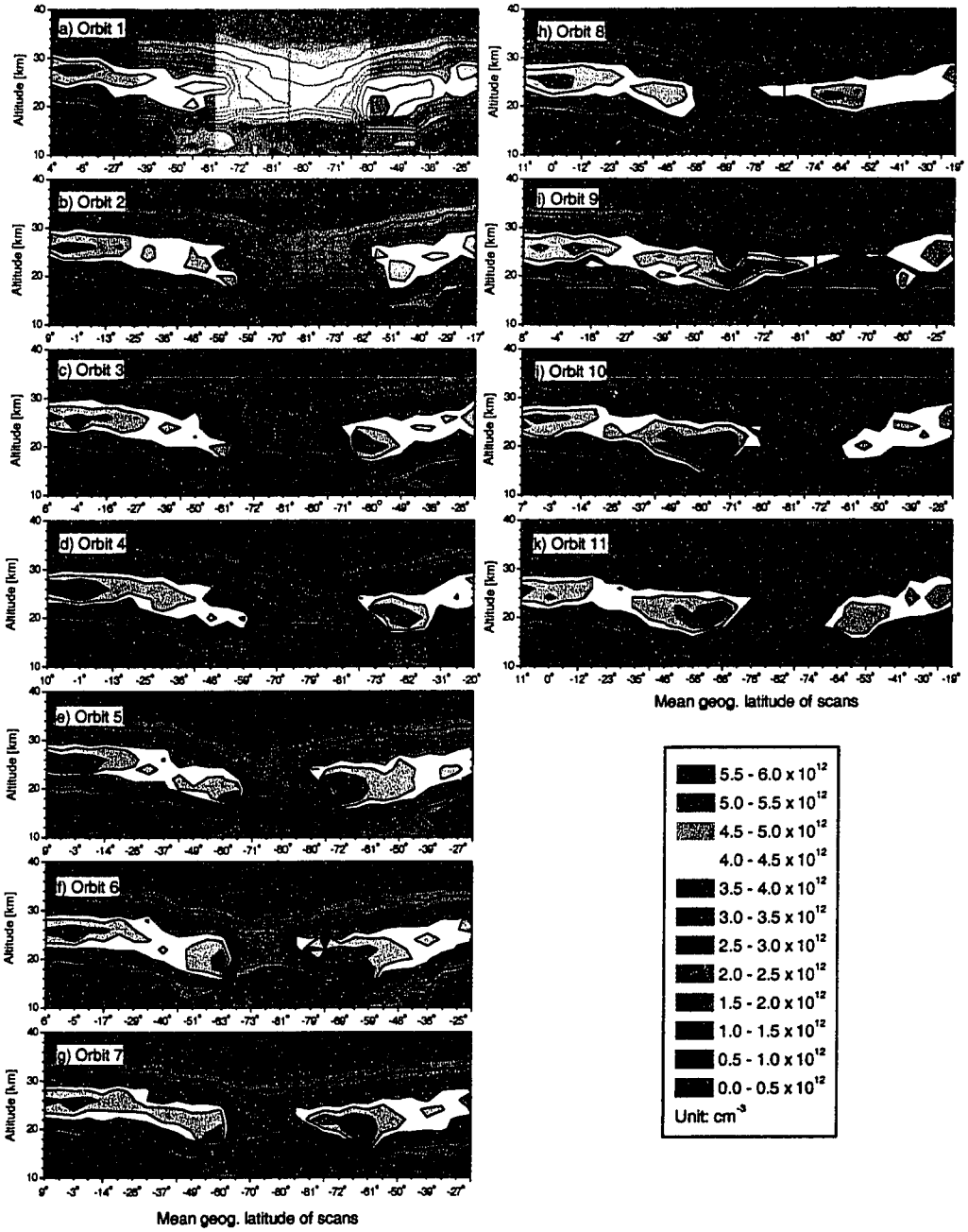

Figure 7.8: 11 orbits measured by OSIRIS in the SH on November 24/25, 2001 are shown. The highest latitude scans (82°S) are indicated by arrows. The antarctic ozone hole is clearly visible.

7.3.2 November 27/28, 2001

Fig. 7.9 shows the tangent point locations for 13 orbits made on November 27 and 28 and the corresponding EP-TOMS total ozone map. Obviously, the location and the shape of the ozone hole have changed somewhat since the previous observations on November 24/25. The ozone hole is elongated and it is approximately oriented along the 60° and -120° meridians. The ozone hole rotates clockwise (viewed from above) with a period on the order of 20 days [*Stolarski et al.*, 1986].

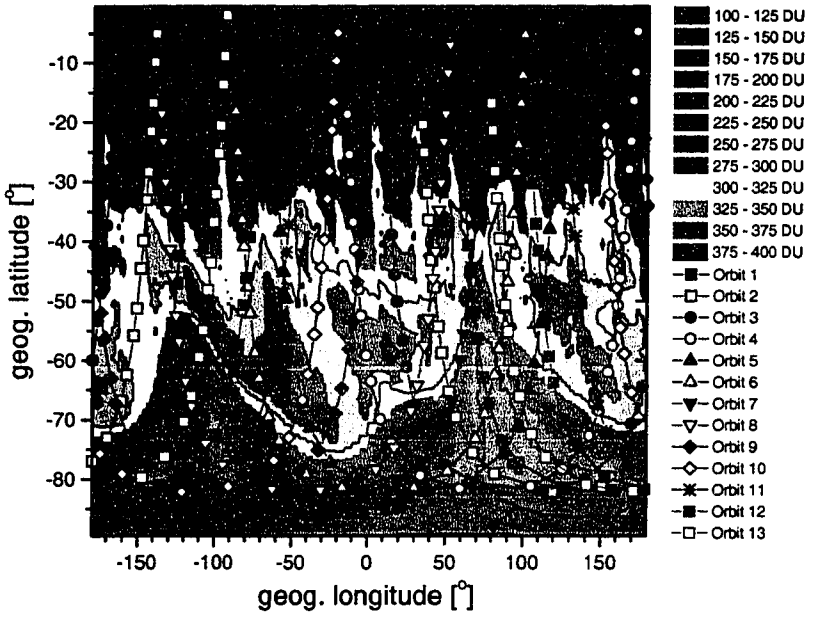

Figure 7.9: Same as Fig. 7.7, but for November 27/28.

Interesting features occur during orbits 10 ($\diamond$) and 11 ($*$) on November 27/28. Between 40°S and 70°S on the down-leg the profiles exhibit sharp peaks and

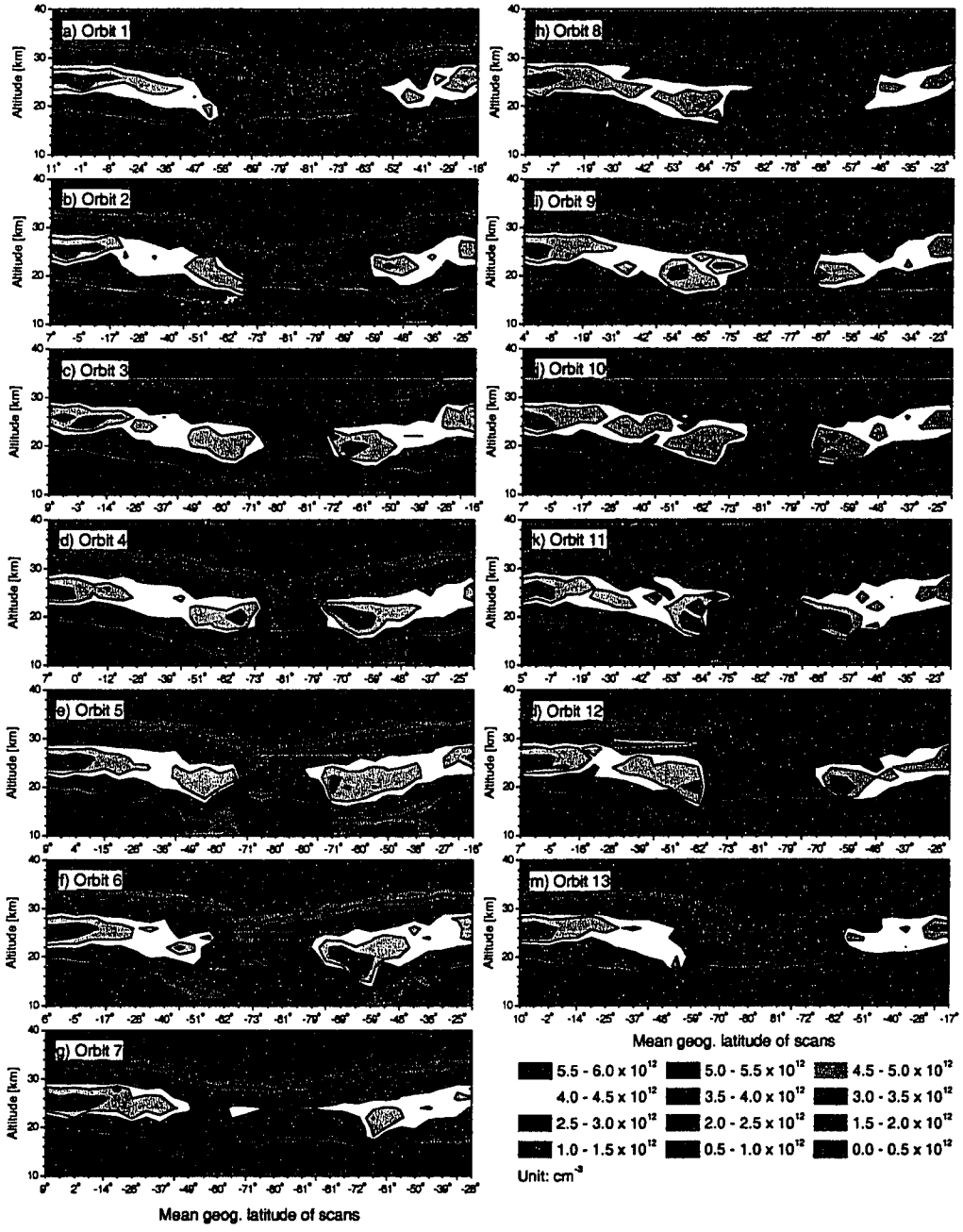

Figure 7.10: 13 orbits measured by OSIRIS in the SH on November 27/28, 2001 are shown. The noisy profiles between 40°S and 70°S for the orbits 10 and 11 were taken when Odin was flying through the South Atlantic Anomaly.

troughs, and the profiles are noisier than the others. For orbit 10 the longitude changes from -30° at a latitude of 40°S to -50° at a latitude of 70°S. In the case of orbit 11 the longitudes are shifted by about 25° westward. Note that the angular difference in the orbit plane between Odin and the tangent point is approximately 23° (22.1° for TH = 100 km, and 24.2° for TH = 0 km). Taking this difference into account, it is clear that Odin was flying right through the South Atlantic Anomaly (SAA) when these noisy limb observations were made. The SAA region which extends from the equator down to 50°S and from -90° to +40° in longitude is associated with enhanced energetic particle fluxes at Odin's altitude arising from the offset of the nominal Earth magnetic dipole.

Chapter 8

Comparison of OSIRIS and CMAM for NH summer

A comparison of the August 2001 NH (northern hemisphere) ozone density field recovered from OSIRIS limb scatter measurements with simulations performed with the Canadian Middle Atmosphere Model (CMAM) has been carried out.

CMAM [*Beagley et al.*, 1997; *de Grandpré et al.*, 2000] is a vertically extended version (0 - 95 km) of the general circulation model (GCM) of the Canadian Centre for Climate Modelling and Analysis (CCCma) [*McFarlane et al.*, 1992]. The model atmosphere consists of 50 levels, with about 3 km vertical resolution in the middle atmosphere. Tracers (species and families) are transported throughout the model atmosphere, and chemistry of shorter-lived species is solved on-line from about 6 km to the upper boundary. The model accommodates 127 photochemical reactions,

including 34 photolysis reactions. It contains 44 chemical species including odd-hydrogen, odd-nitrogen, odd-chlorine, and odd-bromine families, N_2O, CFC-11, CFC-12, CH_3Br, CH_4 and CH_4 oxidation products including CO. Several heterogeneous reactions occurring on stratospheric sulphate aerosols are also included, but heterogeneous PSC chemistry was not included in the version used for the comparison.

The CMAM ozone climatology with interactive chemistry has been described by *de Grandpré et al.* [2000].

8.1 Comparison of ozone density profiles

Fig. 8.1 panel b shows the zonally averaged OSIRIS northern hemisphere ozone field averaged over all days in August 2001, when OSIRIS was operating (*i.e.*, a total of nearly 3900 limb scans obtained over 21 days in August). Panel a of Fig. 8.1 shows a 10 year mean zonally averaged northern hemispheric ozone field for the same altitude range from the CMAM. In panel c of Fig. 8.1 the ratio of the OSIRIS and the CMAM ozone fields is also shown.

A visual comparison of the Figure leads to the following conclusions:

8.1.1 CMAM overestimation below 30 km

Apparently, the CMAM ozone densities around the stratospheric ozone peak are about 15 to 20 % higher than the OSIRIS densities. Previously, CMAM was found [see *de Grandpré et al.*, 2000] to produce ozone densities that were 20 % higher than the COSPAR International Atmosphere (CIRA) ozone reference model [*Keating et al.*, 1990] between about 10 hPa and 20 hPa.

According to *de Grandpré et al.*, part of the discrepancy between CMAM and CIRA in the lower and middle stratosphere may be explained by an underestimation of ozone densities in the upper stratosphere. This underestimation may be caused by a CMAM stratospheric chlorine background that is higher than the background value in the 1980s, when the measurements used for the CIRA compilation were made. An underestimation of the upper stratospheric ozone density will lead to enhanced lower and mid-stratospheric ozone densities since more UV radiation will be able to penetrate into the lower stratosphere, producing more O_x. Another reason for the discrepancy may be related to the 11 year solar cycle which is neglected for the photolysis rate determinations in CMAM.

In terms of the discrepancy between OSIRIS and CMAM at the ozone peak altitudes, the Cl background argument can certainly not be invoked. The fact that the discrepancy between the OSIRIS and the CMAM at the ozone peak altitudes is consistent with the discrepancy between CIRA and CMAM indicates that differences in the stratospheric Cl background are not the main cause for the

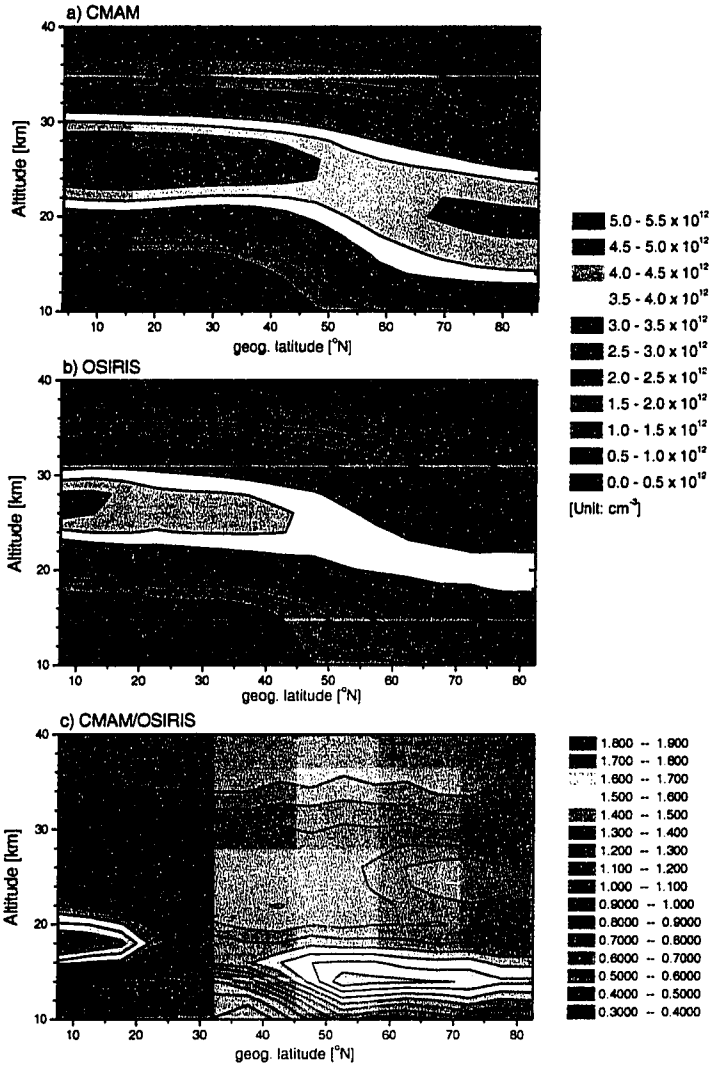

Figure 8.1: Panel a shows the CMAM 10 year mean zonally averaged ozone contours for August. The zonally and temporally averaged ozone field, as measured with OSIRIS from August 2 to 25, 2001, is shown in panel b. Panel c shows the CMAM/OSIRIS ratio.

differences between CIRA and CMAM.

The good agreement between OSIRIS and both POAM III (Chapter 6) and EP-TOMS (Chapter 7) indicates that CMAM must overestimate ozone densities between about 20 and 30 km as well as the total ozone column (discussed in section

8.2).

Inter-annual variability can be ruled out as the cause for the apparent discrepancy between OSIRIS and CMAM. One could argue that the OSIRIS data shown in Fig. 8.1 represent only one year, and the CMAM data a 10 year mean. However, *de Grandpré et al.* [2000] show that the modelled variability in the ozone densities throughout the altitude range covered by OSIRIS is less than about 5 % for northern latitudes in summer and fall. In this context it is interesting that the monthly mean ozone column at certain locations may experience significant inter-annual variations. For example, February means of total ozone over Arosa (Switzerland) varied between about 325 DU and 415 DU during the period from 1957 to 1971 [*Warneck*, 1988]. In particular, the total ozone column changed by up to 50 DU between two consecutive years.

At 18 km at tropical latitudes, and 14 km at mid and high latitudes, the ratio CMAM/OSIRIS reaches values > 1.5. However, this discrepancy may not be significant, since small altitude misalignments between OSIRIS and CMAM will lead to relatively large differences at altitudes with large vertical ozone gradients. The zonally and temporally averaged ozone density profiles between 10 and 35°N latitude shown in Fig. 7.5 exhibit vertical gradients of more than 0.5×10^{12} cm^{-3}/km or 50 %/km.

8.1.2 CMAM underestimation above 35 km

Above 35 km the CMAM ozone densities are approximately 15 % lower than OSIRIS ozone densities. This is again consistent with the comparison of CMAM and CIRA, showing that CMAM ozone densities are about 20 % lower than CIRA at 40 km and low latitudes. At high northern latitudes the discrepancy increased to more than 30 %.

Drawing quantitative conclusions from this relationship between OSIRIS and CMAM is difficult for several reasons:

(a) small altitude misalignments may easily cause differences on the order of 15 % (in fact, a systematic upward shift of the OSIRIS profiles relative to the CMAM profiles may explain CMAM's underestimation in the upper stratosphere as well as part of its overshooting below the peak)

(b) the ozone profile retrieval method becomes less sensitive to ozone and therefore less reliable at altitudes > 35 km and the comparison with POAM III indicates increasing discrepancy for altitudes > 35 km.

Regarding (b) it must be noted that if the OSIRIS ozone densities really underestimate the true densities by 10 % at 40 km altitude, the disagreement with CMAM becomes even worse.

8.1.3 Shape of Ozone isopleths

Fig. 8.1 also shows differences in the shape of the ozone isopleths between OSIRIS and CMAM. Below the stratospheric ozone peak the ozone isopleths as measured by OSIRIS are monotonically decreasing with increasing latitude, whereas the CMAM isopleths assume a local minimum in altitude for latitudes of about 10°N - 15°N and their altitude increases slightly with increasing latitude and reaches a maximum at 30°N - 35°N latitude.

Another important difference between the OSIRIS and CMAM August ozone fields is the steeper decrease of the ozone isopleths above the stratospheric ozone peak in the OSIRIS data set compared to CMAM for latitudes north of 50°N. This behaviour leads to the maximum in the ratio of CMAM and OSIRIS ozone densities at 70°N and 25 km altitude present in Fig. 8.1. This is a greater difference than between CMAM and CIRA [*de Grandpré et al.*, 1997]. Fig. 2 b) of *de Grandpré et al.* [1997] also indicates a widening of the altitude range where the ratio CMAM/CIRA exceeds 1.2 with increasing latitude, but the ratios do not reach 1.3. The comparison of OSIRIS and POAM III ozone profiles at latitudes around 60°N (see Chapter 6) does not indicate any significant underestimation of ozone densities retrieved by OSIRIS for the altitude range 20 - 30 km.

We conclude that the difference between CMAM and OSIRIS at mid and high latitudes between altitudes of 20 and 30 km is significant and consistent with the previous comparison between CMAM and CIRA.

8.2 Comparison of ozone columns

The overshooting of CMAM ozone densities at the ozone peak altitude also manifests itself in the stratospheric ozone columns. Fig. 8.2 compares CMAM and OSIRIS partial stratospheric columns between (a) 10 to 40 km and (b) 15 to 40 km.

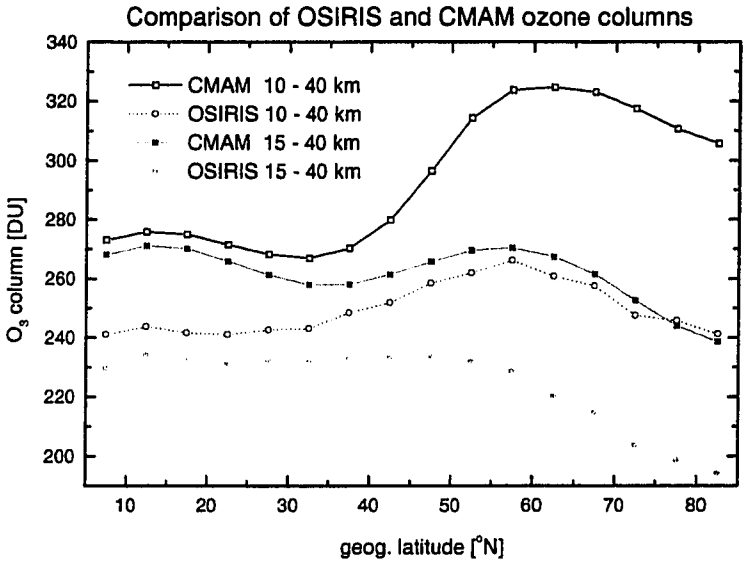

Figure 8.2: OSIRIS and CMAM ozone columns for different altitude ranges. Clearly, CMAM ozone columns are systematically higher than the OSIRIS columns.

It must be mentioned that CMAM's monthly mean total vertical ozone columns agree within about 3 % with the CIRA reference atmosphere [*de Grandpré et al.*, 2000], whereas CMAM partial stratospheric ozone columns are systematically between 10 % and 20 % higher than OSIRIS columns.

It should also be noted that despite the differences between OSIRIS and CMAM ozone densities mentioned above, the general agreement is very good. The model is able to capture the latitude dependence of the stratospheric ozone density peak, and the widening of the peak with increasing latitude very well. Furthermore, the shape of the latitude dependence of the partial stratospheric ozone column (Fig. 8.2) predicted by CMAM compares very well with OSIRIS observations.

Chapter 9

Conclusions and Future work

It has been demonstrated, through both extensive modelling and the analysis of actual satellite measurements, that observations of scattered sunlight limb radiance spectra, coupled with state-of-the-art radiative transfer models, provide a powerful new tool for the remote sensing of stratospheric ozone profiles. These profiles can be obtained globally with high vertical resolution (1 - 2 km). The stratospheric ozone density profiles retrieved from the OSIRIS observations made during August 2001 are in excellent agreement with the current knowledge of the global morphology of ozone. The analysis of the OSIRIS observations made from the Odin satellite in the vicinity of the Antarctic ozone hole have provided the first set of high resolution ozone profiles in the ozone hole region. The observation and analysis technique represents a new capability that should be of great value for the future development of atmospheric models used in ozone research. In addition, the

analysis of observations made on several orbits during selected days in November 2001 has indicated that the scattered sunlight technique is also capable of accurately monitoring the 3-dimensional evolution of the Antarctic ozone hole. These measurements will also provide a new database for both atmospheric models and ozone trend studies. While the derived ozone profiles are in good agreement with those obtained from the POAM-III solar occultation measurements there is still a need for formal validation of the retrieved ozone profiles within the stratospheric ozone hole.

The ozone profiles derived from the OSIRIS measurements have been compared with those calculated with CMAM model. Above 35 km the CMAM calculated ozone densities are systematically lower than the measured OSIRIS densities by as much as 15 %. The CMAM overestimation of the ozone density in the vicinity of the peak altitude and the underestimation in the upper stratosphere have been previously noted from a comparison of CMAM results and the CIRA reference atmosphere [*de Grandpré et al.*, 2000].

9.1 Future work

It is suggested that while the present work has made significant advances in the remote sensing of the atmosphere there is still a need for new and on-going work that is much more than simply collecting and analyzing OSIRIS data.

- There should be a comparative evaluation of the different methods that are available to retrieve ozone density profiles from OSIRIS limb scans (*i.e.*, limb DOAS (section 2.4.1) [*McDade et al.*, 2002; *Haley et al.*, 2001b] and MOP (section 2.4.2) [*Auvinen et al.*, 2001a; 2001b]).

- There should be a comprehensive validation of the OSIRIS ozone profiles for different observing conditions (particularly for high SZAs and within the Antarctic ozone hole).

- The extension of the present technique to higher altitudes using the both Huggins and Hartley absorption bands of ozone should be investigated in detail and the results compared with the ozone densities derived from the IR Imager component of OSIRIS. This is particularly interesting in light of the recent discovery of a third ozone maximum in the middle mesosphere at high latitudes during spring [*Marsh et al.*, 2001].

- There should be a detailed comparison of the OSIRIS ozone density profiles with those derived from the Odin SMR observations.

- The possible flight in the near future of an improved version of the OSIRIS instrument should be considered and the concept of including three vertical imagers operating at the three wavelengths used in this study should be investigated.

Appendix A

Derivation of the optimal estimation equations

In the following the optimal estimation equations:

$$\hat{\mathbf{x}} = \mathbf{x_0} + \mathbf{S_x K^T} \left(\mathbf{K S_x K^T} + \mathbf{S_\epsilon} \right)^{-1} (\mathbf{y} - \mathbf{K x_0}) \tag{A.1}$$

and

$$\hat{\mathbf{S}} = \mathbf{S_x} - \mathbf{S_x K^T} \left(\mathbf{K S_x K^T} + \mathbf{S_\epsilon} \right)^{-1} \mathbf{K S_x} \tag{A.2}$$

are derived from

$$\hat{\mathbf{x}} = \left(\mathbf{S_x^{-1}} + \mathbf{K^T S_\epsilon^{-1}} \right)^{-1} \left(\mathbf{S_x^{-1} x_0} + \mathbf{K^T S_\epsilon^{-1} y} \right) \tag{A.3}$$

and

$$\hat{\mathbf{S}} = \left(\mathbf{S_x^{-1}} + \mathbf{K^T S_\epsilon^{-1}} \right)^{-1} \tag{A.4}$$

Begin with the identity

$$\mathbf{K^T S_\epsilon^{-1}} \left[\mathbf{S_\epsilon + K S_x K^T}\right] = \left[\mathbf{S_x^{-1} + K^T S_\epsilon^{-1} K}\right] \mathbf{S_x K^T} \tag{A.5}$$

The inverse of the right hand side of this equation is given by

$$\left(\left[\mathbf{S_x}^{-1} + \mathbf{K^T S_x K}\right] \mathbf{S_x K^T}\right)^{-1} = \mathbf{K^{T-1}} \mathbf{S_x}^{-1} \left[\mathbf{S_x}^{-1} + \mathbf{K^T S_\epsilon}^{-1} \mathbf{K}\right)^{-1} \tag{A.6}$$

Multiplying the left side of eqn. (A.5) by the right side of eqn. (A.6) yields

$$\mathbf{K^T S_\epsilon}^{-1} \left[\mathbf{S_\epsilon + K S_x K^T}\right] \mathbf{K^{T-1}} \mathbf{S_x}^{-1} \left[\mathbf{S_x}^{-1} + \mathbf{K^T S_\epsilon}^{-1} \mathbf{K}\right]^{-1} = \mathbf{1} \tag{A.7}$$

$$\iff \quad \mathbf{K^{T-1}} \mathbf{S_x}^{-1} \left[\mathbf{S_x}^{-1} + \mathbf{K^T S_\epsilon}^{-1} \mathbf{K}\right]^{-1} = \left[\mathbf{S_\epsilon + K S_x K^T}\right]^{-1} \mathbf{S_\epsilon K^{T-1}} \tag{A.8}$$

$$\iff \quad \left[\mathbf{S_X}^{-1} + \mathbf{K^T S_\epsilon}^{-1} \mathbf{K}\right]^{-1} \mathbf{K^T S_\epsilon}^{-1} = \mathbf{S_x K^T} \left[\mathbf{S_\epsilon + K S_x K^T}\right]^{-1} \tag{A.9}$$

Now consider

$$\mathbf{S_x - S_x K^T} \left[\mathbf{S_\epsilon + K S_x K^T}\right]^{-1} \mathbf{K S_x} \tag{A.10}$$

$$\overset{eqn.(A.9)}{=} \mathbf{S_x} - \left[\mathbf{S_x}^{-1} + \mathbf{K^T S_\epsilon}^{-1} \mathbf{K}\right]^{-1} \mathbf{K^T S_\epsilon}^{-1} \mathbf{K S_x} \tag{A.11}$$

$$= \left[\mathbf{S_x}^{-1} + \mathbf{K^T S_\epsilon}^{-1}\mathbf{K}\right]^{-1} \left(\left[\mathbf{S_x}^{-1} + \mathbf{K^T S_\epsilon}^{-1}\mathbf{K}\right]\mathbf{S_x} - \mathbf{K^T S_\epsilon}^{-1}\mathbf{K S_x}\right) \qquad \text{(A.12)}$$

$$= \left[\mathbf{S_x}^{-1} + \mathbf{K^T S_\epsilon}^{-1}\mathbf{K}\right]^{-1} = \hat{\mathbf{S}}, \quad \text{i.e., eqn.(A.2)} = \text{eqn.(A.4)} \qquad \text{(A.13)}$$

Then eqn. (A.2) is inserted into eqn.(A.3) to give

$$\hat{\mathbf{x}} = \mathbf{x_0} - \mathbf{S_x K^T}\left[\mathbf{K S_x K^T} + \mathbf{S_\epsilon}\right]^{-1}\mathbf{K x_0} + \hat{\mathbf{S}}\mathbf{K^T S_\epsilon}^{-1}\mathbf{y} \qquad \text{(A.14)}$$

Furthermore

$$\hat{\mathbf{S}} = \left[\mathbf{S_x}^{-1} + \mathbf{K^T S_\epsilon}^{-1}\mathbf{K}\right]^{-1} = \left[\mathbf{S_x}^{-1} + \mathbf{K^T S_\epsilon}^{-1}\mathbf{K}\right]^{-1}\mathbf{K^T S_\epsilon}^{-1}\mathbf{S_\epsilon K^{T-1}} \qquad \text{(A.15)}$$

$$\overset{eqn.(A.9)}{=} \mathbf{S_x K^T}\left[\mathbf{S_\epsilon} + \mathbf{K S_x K^T}\right]^{-1}\mathbf{S_\epsilon K^{T-1}} \qquad \text{(A.16)}$$

Insert eqn. (A.16) into eqn. (A.14)

$$\hat{\mathbf{x}} = \mathbf{x_0} + \mathbf{S_x K^T}\left(\mathbf{K S_x K^T} + \mathbf{S_\epsilon}\right)^{-1} = (\mathbf{y} - \mathbf{K x_0}) \qquad \text{(A.17)}$$

Appendix B

Catalytic ozone destruction cycles

This appendix graphically summarizes the chemical cycles important for stratospheric chemistry discussed in chapter 2. Photochemical reactions are denoted by $h\nu$, and thermal decomposition by Δ. The Nicolet diagrams are adapted from *Wayne* [1991].

B.0.1 The HO_x cycle

B.0.2 The NO_x cycle

B.0.3 The ClO_x cycle

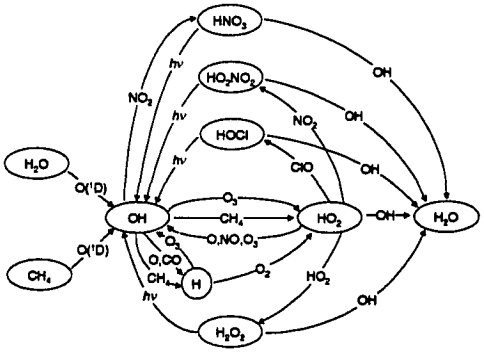

Figure B.1: Nicolet diagram of the chemical reactions of the HO_x family in the stratosphere.

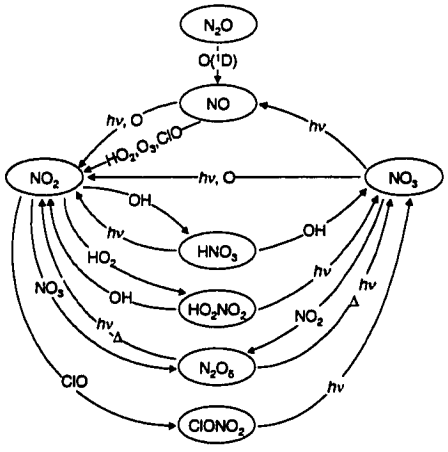

Figure B.2: Nicolet diagram of the chemical reactions of the NO_x family.

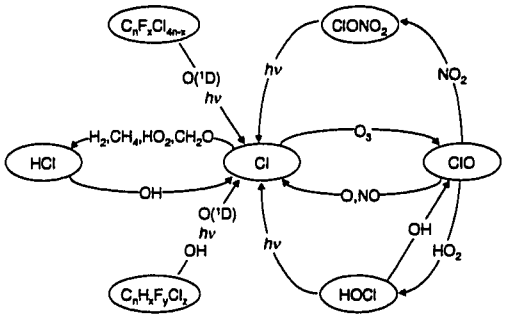

Figure B.3: Nicolet diagram of the chemical reactions of the ClO_x family.

Appendix C

NCEP tropopause heights

Geog. latitude	Tropopause height in km
2.5°N	15.38
7.5°N	15.38
12.5°N	15.36
17.5°N	15.33
22.5°N	15.25
27.5°N	15.10
32.5°N	14.83
37.5°N	14.31
42.5°N	13.19
47.5°N	11.59
52.5°N	10.64
57.5°N	10.11
62.5°N	9.81
67.5°N	9.55
72.5°N	9.25
77.5°N	9.00
82.5°N	8.79

Table C.1: Tropopause height as a function of latitude obtained from the NCEP tropopause pressure climatology [*Randel et al.*, 2000] for the month of August. Tropopause heights are obtained from NCEP tropopause pressure assuming a scale height of $H = 7$ km and a surface pressure of 1013.25 hPa (recommendation of Bill Randel (NCAR), January 2002). The NCEP climatology comprises an 40 year average (1957-1997).

Appendix D

Upper stratospheric Ozone from Huggins band observations

A code has been written using a similar methodology as for the ozone retrieval from Chappuis band absorption to retrieve ozone densities in the upper stratosphere from OSIRIS limb scatter observations. Due to the greater absorption cross sections within the Huggins bands compared with the Chappuis bands, UV radiances between 300 nm and 340 nm are more sensitive to ozone in the upper stratosphere. Lower stratospheric ozone concentrations can not be inferred from these wavelengths since the atmosphere is optically thick causing limb radiances at TH below about 25 km and wavelengths shorter than about 340 nm to be almost completely insensitive to ozone. The normalized limb radiance profiles at 4 different wavelengths within the Huggins bands are simultaneously used to retrieve ozone.

Those wavelengths are $\lambda_1 = 306$ nm, $\lambda_2 = 316$ nm, $\lambda_3 = 322$ nm and $\lambda_4 = 355$ nm, and they have been chosen as a compromise to minimize the combined sensitivity to (a) the temperature dependence of the ozone absorption cross section, and (b) Rotational Raman Scattering (RRS) [*C. Sioris, personal communication*, 2001].

The limb radiance profiles at these four wavelengths are combined to form a vector - similar to the Chappuis retrieval vector - that is used by the OE algorithm:

$$y_H(i) = \frac{LR_N(TH_i, \lambda_1)}{LR_N(TH_i, \lambda_4)} \quad ; i = 1, m \tag{D.1}$$

$$= \frac{LR_N(TH_{i-m}, \lambda_2)}{LR_N(TH_{i-m}, \lambda_4)} \quad ; i = m+1, 2m \tag{D.2}$$

$$= \frac{LR_N(TH_{i-2m}, \lambda_3)}{LR_N(TH_{i-2m}, \lambda_4)} \quad ; i = 2m+1, 3m \tag{D.3}$$

The recoveries are done in a similar way as described for the Chappuis band retrieval in section 4.1.5.

References

Aben, I., F. Helderman, D. M. Stam, and P. Stammes, Spectral fine-structure in the polarization of skylight, *Geophys. Res. Lett., 26, 591-594,* 1999.

Auvinen, H., L. Oikarinen, and E. Kyrölä, Inversion algorithms for limb scatter measurements in UV-visible wavelengths, *submitted to J. Geophys. Res.,* 2001a.

Auvinen, H., L. Oikarinen, E. Kyrölä, and the Odin team, Retrieval of Trace Gas and Aerosol Densities from Limb Scatter Measurements by OSIRIS on Odin Using Modified Onion Peeling Method, *Eos Trans. AGU, 82*(47), Fall Meet. Suppl., Abstract A21B-0066, 2001b.

Bacis, R., A, J. Bouvier, and J. M. Flaud, The ozone molecule: electronic spectroscopy, *Spectr. Acta, 54, 17-34,* 1998.

Beagley, S. R., J. de Grandpré, J. N. Koshyk, N. A. McFarlane, and T. G. Shepherd, Radiative-dynamical climatology of the first-generation Canadian Middle Atmosphere Model, *Atmos. Ocean, 35,* 293-331, 1997.

Beagley, S. R., C. McLandress, V. I. Fomichev, and W. E. Ward, The extended

Canadian Middle Atmosphere Model, *Geophys. Res. Lett., 27,* 2529-2532, 2000.

Berge, S., O. Jirlow, P. Rathsman, F. V. Schéele, Advanced Attitude Control on Swedish Small Satellite Odin, *Proceedings, 48th International Astronautical congress*, October 6-10, Turin, Italy, 1997

Berk, A., L. S. Bernstein, and D. C. Robertson, MODTRAN: A Moderate Resolution Model for LOWTRAN 7, *AFGL Tech. Rep. F19628-86-C-0079*, 38 pp., Air Force Geophys. Lab., Hanscom AFB, Mass., 1989.

Bertaux, J. L., G. Megie, T. Widemann, E. Chassefiere, R. Pellinen, E. Kyrölä, S. Korpela, and P. Simon, Monitoring of ozone trend by stellar occultations: The GOMOS instrument, *Adv. Space Res., 11, 237-242,* 1991.

Bingen, C., and D. Fussen, Structure and spectral features of the stratospheric aerosol extinction profiles in the UV-visible range from SAGE II data, *J. Geophys. Res., 105, 4767-4776,* 2000.

Bovensmann, H., J. P. Burrows, M. Buchwitz, J. Frerick, S. Noel, V. V. Rozanov, K. V. Chance, and A. P. H. Goede, SCIAMACHY: Mission objectives and measurement modes, *J. Atmos. Sci., 56, 127-150,* 1999.

Bronstein, I. N, and K. A. Semendjajew, Taschenbuch der Mathematik, Verlag Nauka, Moscow and B. G. Teubner, Stuttgart 1991.

Burrows, J. P., M. Weber, M. Buchwitz, V. V. Rozanov, A. Ladstättermann, M.

Eisinger, and D. Perner, The Global Ozone Monitoring Experiment (GOME): Mission Concept, and First Scientific Results, *J. Atmos. Sci., 56, 151-175,* 1999.

Chu, W. P., M. P. McCormick, J. Lenoble, C. Brogniez and P. Pruvost, SAGE II Inversion Algorithm, *J. Geophys. Res., 94, 8339-8351,* 1989.

Chubachi, S., A special ozone observation at Syowa Station, Antarctica from February 1982 to January 1983, Quadrennial Ozone Symposium, Greece, 1984.

Coffey, M. T., W. G. Mankin, and A. Goldman, Airborne Measurements of stratospheric constituents over Antarctica in the Austral spring 1987, 2, Halogen and nitrogen trace gases, *J. Geophys. Res., 94*, 16597-16613, 1989.

Cunnold, D. M., C. R. Gray, and D. C. Merritt, Stratospheric aerosol layer detection, *J. Geophys. Res., 78*, 920-931, 1973.

Cunnold, D. M., L. Froidevaux, J. M. Russell, B. Connor, and A. Roche, Overview of UARS ozone validation based primarily on intercomparison among UARS and SAGE II measurements, *J. Geophys. Res., 101*, 10,335-10,350, 1996.

Crutzen, P. J., Ozone production rates in an oxygen-hydrogen-nitrogen oxide atmosphere, *J. Geophys. Res., 76*, 7311 - 7327, 1971.

Danilin, M. Y., M. K. W. Ko, R. M. Bevilacqua, L. V. Lyjak, L. Froidevaux, M. L. Santee, J. M. Zawodny, K. W. Hoppel, E. C. Richard, J. R. Spackman, E. M. Weinstock, R. L. Herman, K. A. McKinney, P. O. Wennberg, F. L. Eisele, R.

M. Stimpfle, C. J. Scott, J. W. Elkins, T. V., Bui, Comparison of ER-2 Aircraft and POAM-III, MLS, and SAGE-II Satellite Measurements during SOLVE Using Traditional Correlative Analysis and Trajectory Hunting Technique, *J. Geophys. Res.*, in press, 2002.

de Grandpré, J., S. R. Beagley, V. I. Fomichev, E. Griffioen, J. C. McConnell, and A. S. Medvedev, Ozone climatology using interactive chemistry: Results from the Canadian Middle Atmosphere Model, *J. Geophys. Res., 105*, 26,475-26,491, 2000.

Degenstein, D., Atmospheric Volume Emission Tomography from a Satellite Platform, *Ph. D. Thesis, University of Saskatchewan, Saskatoon,* 1999.

Dobson, G. M. B., Forty Years Research on Atmospheric Ozone at Oxford: a History, *Applied Optics, 7, 387-405*, 1968.

Dobson, G. M. B., The laminated structure of the ozone in the atmosphere, *Q. J. R. Meteorol. Soc., 99,* 599-607, 1973.

Eisinger, M., A. Richter, A. Ladstätter-Weissmayer, and J. P. Burrows, DOAS zenith sky observations: 1. BrO measurements over Bremen (53°N) 1993-1994, *J. Atm. Chem., No. 26*, pp. 93-108, 1997.

Evans, W. F. J., and E. J. Llewellyn, Measurements of mesospheric ozone from observations of the 1.27 μm band, *Radio Science, 7,* 45-50, 1972.

Evans, W. F. J., and E. J. Llewellyn, Atomic Hydrogen concentrations in the

mesosphere and the hydroxyl emissions, *J. Geophys., Res., 78,* 323-326, 1973.

Evans, W. F. J., and J. M. Alfred, Algorithm for Correction of Internal Scattering and Spectral Cross-Talk in the UV/VIS band of the OSIRIS Instrument Flight Model, *OSIRIS internal report*, Trent University, Peterborough, Ontario, Canada, 2001.

Evans, W. F. J., C. Sioris, S. Petelina, E. J. Llewellyn, L. R. Chardon and the Odin Team, The Validation Inter-comparison of Polar Mesospheric Clouds from OSIRIS with WINDII, *Eos Trans. AGU, 82*(47), Fall Meet. Suppl., Abstract SA41B-0740, 2001.

Farman, J. C., B. G. Gardiner, and J. D. Shanklin, Large Losses of Total Ozone in Antarctica Reveal Seasonal ClO_x/NO_x Interaction, *Nature, 315, 207-210,* 1985.

Farmer, C. B., G. C. Toon, P. W. Shaper, J. F. Blavier, and L. L. Lowes, Stratospheric trace gases in the spring 1986 Antarctic Atmosphere, *Nature, 329*, 126-130, 1987.

Ferlemann, F., N. Bauer, R. Fitzenberger, H. Harder, H. Osterkamp, D. Perner, U. Platt, M. Schneider, P. Vradelis, and K. Pfeilsticker, Differential Optical Absorption Spectroscopy Instrument for Stratospheric Balloon-borne Trace-Gas Studies, *Appl. Opt., 39,* 2377-2386, 2000.

Fishman, J., P. Minnis, and H. G. Reichle, The use of satellite data to study tropospheric ozone in the tropics, *J. Geophys. Res., 91,* 14,451-14,465, 1986.

Fishman, J., F. M. Vukovich, D. R. Cahoon, and M. C. Shipam, The characterization of an air pollution episode using satellite total ozone measurements, *J. Clim. Appl. Meteorol., 26*, 1638-1654, 1987.

Fishman, J., C. E. Watson, J. C. Larsen, and J. A. Logan, Distribution of Tropospheric Ozone Determined From Satellite Data, *J. Geophys. Res., 95*, 3599-3617, 1990.

Flittner, D. E., P. K. Bhartia, and B. M. Herman, O_3 profiles retrieved from limb scatter measurements: Theory, *Geophys. Res. Lett., 27*, 2061-2064, 2000.

Frieß U., Otten C., M. Chipperfield, Wagner T., Pfeilsticker K., and Platt U., Intercomparison of measured and modelled BrO slant column amounts for the Arctic winter and spring 1994/95, *Geophys. Res. Lett., 26*, 1861-1864, 1999.

Griffioen, E., and L. Oikarinen, LIMBTRAN: A Pseudo Three-Dimensional Radiative Transfer Model for the Limb-Viewing Imager OSIRIS on the ODIN Satellite, *J. Geophys. Res., 105*, 707-730, 2000.

Haley, C. S., C. von Savigny, and C. Sioris, Internal Scattering Correction for the Optical Spectrograph, *OSIRIS internal report*, York University, 2001a.

Haley, C. S., C. E. Sioris, C. von Savigny, I. C. McDade, E. Griffioen, C. A. McLinden, E. J. Llewellyn, and the Odin Team, Retrieval of Stratospheric O_3 and NO_2 Density Profiles From a DOAS Analysis of UV-Visible Limb Scatter Measured by OSIRIS, *Eos Trans. AGU, 82*(47), Fall Meet. Suppl., Abstract A42A-0097,

2001b.

Haley, C., OS Level 0 $\longrightarrow$ 1 Processing and Error Approximation, *OSIRIS internal report*, York University, 2001c.

Hartley, W. N., On the absorption of solar rays by atmospheric ozone, *J. Chem. Soc., 39*, 111, 1881.

Hasekamp, O. P., and J. Landgraf, Ozone profile retrieval from backscattered ultraviolet radiances: The inverse problem solved by regularization, *J. Geophys. Res., 106*, 0877-8088,2001.

Heath, D. E., A. J. Krueger, H. R. Roeder, and B. D. Henderson, The Solar Backscatter Ultraviolet and Total Mapping Spectrometer (SBUV/TOMS) for Nimbus G, *Opt. Eng.*, 323-331, 1975.

Hedin, A. E., Extension of the MSIS Thermospheric Model into the Middle and Lower Atmosphere, *J. Geophys. Res., 96, 1159,* 1991.

Hoinka, K. P., H. Claude, U. Köhler, On the Correlation Between Tropopause Pressure and Ozone Above Central Europe, *Geophys. Res. Lett., 23, 1753-1756*, 1996.

Hoogen, R., V. V. Rozanov, and J. P. Burrows, Ozone profiles from GOME satellite data: Algorithm description and first validation, *J. Geophys. Res., 104*, 8263-8280, 1999.

Houzeau, A., Preuve de la présence dans l'atmosphere d'un nouveau principe gazeux l'oxygéne naissant, *C. R. Acad. Sci. Paris, 46*, 89, 1958.

Infante, G. M., Nonlinear Effects in Retrieval of Ozone Density Profiles from Satellite Measurements of Scattered Sunlight, *M. Sc. Thesis, York University, Toronto, Canada*, 2001.

Janz, S. J., E. Hilsenrath, D. Flittner, and D. Heath, Rayleigh Scattering Attitude Sensor, *SPIE Proc., 2831*, 146-153, 1996.

Johnston, H. S., Reduction of stratospheric ozone by nitrogen oxide catalysts from supersonic transport exhaust, *Science, 173*, 517-522, 1971.

Keating, G. M., M. C. Pitts, and D. F. Young, Ozone reference models for the middle atmosphere, *Adv. Space Res., 10, No. 12*, 12,317-12,355, 1990.

Lee, K.-M., J.M. McInerey, Y. Sasano, J. H. Park, W. Choi, and J. M. Russell III, Intercomparison of ILAS and HALOE ozone at high latitudes, *Geophys. Res. Lett., 26*, 835-838, 1999.

Llewellyn, E. J., and R. L. Gattinger, Estimated OSIRIS UVIS Baffle On-Orbit Performance, *OSIRIS Internal report*, University of Saskatchewan, Saskatoon, 1998.

Llewellyn, E. J., D. A. Degenstein, I. C. McDade, R. L. Gattinger, R. King, R. Buckingham, E. H. Richardson, D. P. Murtagh, W. F. J. Evans, B. H. Solheim,

K. Strong, and J. C. McConnell, OSIRIS - An Application of Tomography for Absorbed Emissions in Remote Sensing, *Appl. Phot. Techn., 2, 627-632,* 1997.

Lucke, R. L., D. Korwan, R. M. Bevilacqua, J. S. Hornstein, E. P. Shettle, D. T. Chen, M. Daehler, J. D. Lumpe, M. D. Fromm, D. Debrestian, B. Neff, M. Squire, G. König-Langlo, and J. Davies, The Polar Ozone and Aerosol Measurement (POAM) III instrument and early validation results, *J. Geophys. Res., 104,* 18785-18799, 1999.

Marsh, D., A. Smith, G. Brasseur, M. Kaufmann, K. Grossman, The existence of a tertiary ozone maximum in the high-latitude middle mesosphere, *Geophys. Res. Lett. 28,* 4531-4534, 2001.

Marshall, G., Two Ground-Based Testing Procedures for the ODIN Satellite/OSIRIS Spectrograph Development Model, *Internal report, University of Saskatchewan, Saskatoon,* 1996.

Matthews, E., Global vegetation and land use: new high-resolution data bases for climate studies, *J. Clim. Appl. Meteor., 22,* 474-487, 1983.

Maudlin, L. E., N. H. Zaun, M. P. McCormick, J. H. Guy, and W. R. Vaughn, Stratospheric Aerosol and Gas Experiment II Instrument: A Functional Description, *Opt. Eng., 24, 307-312,* 1985.

McDade, I. C., Haley, C., Sioris, C., Solheim, B., von Savigny, C., and the Odin team, OSIRIS on Odin: Initial Observational Results From the UV/visible Spec-

trograph, *Eos Trans. AGU, 82*(47), Fall Meet. Suppl., Abstract SA22A-0708, 2001.

McDade, I. C., K. Strong, C. S. Haley, J. Stegman, D. P. Murtagh, and E. J. Llewellyn, A method for recovering stratospheric minor species densities from the Odin OSIRIS scattered sunlight measurements, *Can J. Phys, 80*, S1, 2002.

McFarlane, N. A., G. J. Boer, J.-P. Blanchet, and M. Lazare, The Canadian climate Centre second generation GCM and its equilibrium climate, *J. Clim., 5*, 1013-1044, 1992.

McLinden, C. A., Observations of Atmospheric Composition from NASA ER-2 Spectroradiometer Measurements, *Ph. D. Thesis*, York University, 1996.

McLinden, C. A., J. C. McConnell, E. Griffioen, and C. T. McElroy, A vector radiative transfer model for the ODIN/OSIRIS project, *Can. J. Phys., 80*, S1, 2002a.

McLinden, C. A., J. C. McConnell, K. Strong, I. C. McDade, R. L. Gattinger, R. King, B. Solheim, E. J. Llewellyn, and W. J. F. Evans, The Impact of the OSIRIS grating efficiency on radiance and trace-gas retrievals, *Can. J. Phys., 80*, S1, 2002b.

McPeters, R. D, P. K. Bhartia, A. J. Krueger, and J. R. Herman, Earth Probe Total Ozone Mapping Spectrometer (TOMS) Data Product User's Guide, *NASA/IP-1998-206895*, 1998.

McPeters, R. D., S. J. Janz, E. Hilsenrath, and T. L. Brown, The retrieval of O_3 profiles from limb scatter measurements: Results from the Shuttle Ozone Limb Sounding Experiment, *Geophys. Res. Lett., 27, 2601-2604,* 2000.

Molina, M. J., and F. S. Rowland, Stratospheric Sink for chlorofluoromethanes: chlorine atom catalyzed destruction of ozone, *Nature, 249, 810-812*, 1974.

Mount, G. H., D. W. Rusch, J. F. Noxon, J. F., J. M. Zawodny, and C. A. Barth, Measurements of stratospheric NO_2 from the SME Satellite, *J. Geophys. Res., 89*, 1327-1340, 1984.

Murtagh, D. P., G. Witt, R. Mewe, H. van der Woerd, N. Kämpfer, P. Taalas, J. Askne, and A. Winnberg, Odin aeronomy science, A phase-A report by the aeronomy science working group for the Odin satellite, *Report AP-31*, Department of Meteorology, Stockholm University, 1993.

Murtagh, D. P., U. Frisk, F. Merino, M. Ridal, A. Jonsson, J. Stegman, G. Witt, P. Eriksson, C. Jiménez, G. Megie, J. de la Nöe, P. Ricaud, P. Baron, J. R. Pardo, A. Hauchcome, E. J. Llewellyn, D. A. Degenstein, R. L. Gattinger, N. D. Lloyd, W. F. J. Evans, I. C. McDade, C. S. Haley, C. Sioris, C. von Savigny, B. H. Solheim, J. C. McConnell, K. Strong, E. H. Richardson, G. W. Leppelmeier, E. Kyrölä, H. Auvinen, and L. Oikarinen, An overview of the Odin atmospheric mission, *Can J. Phys, 80*, S1, 2002.

Newman, P., Stratospheric Ozone, Chapter 5,

http://see.gsfc.nasa.gov/edu/SEES/, 2000.

Oikarinen, L., E. Sihvola, and E Kyrölä, Multiple scattering radiance in limb-viewing geometry, *J. Geophys. Res., 104*, 31261-31274, 1999.

Oikarinen, L., Polarization of light in UV-visible limb radiance measurements, *J. Geophys. Res., 106, 1533-1544,* 2001a.

Oikarinen, L., Griffioen, E., Loughman, R., Postyliakov, O., and Rozanov, A., Comparison of Radiative Transfer Models for Limb-Viewing Scattered Sunlight Measurements, *Eos Trans. AGU, 82*(47), Fall Meet. Suppl., Abstract A21B-0067, 2001b.

Oikarinen, L., Averaging of surface albedo in atmospheric UV-visible limb scatter measurements, *J. Geophys. Res.,* in press, 2002.

Petelina, S. V., E. J. Llewellyn, N. D. Lloyd, C. Sioris, W. F.J. Evans, and the Odin Team, Polar Mesospheric Clouds Observed by the Optical Spectrograph on Odin in July-August, 2001, *Eos Trans. AGU, 82*(47), Fall Meet. Suppl., Abstract SA41B-0744, 2001.

Peter, T., B. P. Luo, C. Kiemler, S. Borrmann, F. Cairo, I Stefanutti, V. Santacesaria, and A. R. MacKenzie, Subvisible Clouds at the Tropical Tropopause, *presented at the IAMAS meeting, July 10-18, Innsbruck, Austria,* 2001.

Platt, U., Differential Optical Absorption Spectroscopy, In: Air Monitoring by

Spectroscopic Techniques, *edited by M. W. Sigrist, Wiley, New York,* 1994.

Press, W. H., S. A. Teukolsky, W. T. Vetterling, and B. P. Flannery, Numerical Recipes in FORTRAN, The art of scientific computing, *Clarendon Press, Oxford,* 1992.

Randel, W. J., W. Wu, and D. Gaffen, Interannual variability of the tropical tropopause derived from radiosonde data and NCEP reanalyses, *J. Geophys. Res., 105,* 15509-15523, 2000.

Rodgers, C. D., Retrieval of Atmospheric Temperature and Composition From Remote Measurements of Thermal Radiation, *Rev. Geophys. & Space Phys., 14, 609-624,* 1976.

Rödel, W., Physik unserer Umwelt: Die Amsphäre, 457 pp., Springer Verlag, Berlin, 1992.

Rowland, F. S, and M. J. Molina, Chloroflouromethanes in the environment, *Rev. Geophys. & Space Phys., 13,1,* 1975.

Rusch, D. W., G. H. Mount, C. A. Barth, R. J. Thomas, and M. T. Callan, Solar mesosphere explorer ultraviolet spectrometer: measurements of ozone in the 1.0-0.1 mbar region, *J. Geophys. Res., 89,* 11677-11678, 1984.

Rusch, D. W., C. E. Randall, R. M. Bevilacqua, K. W. Hoppel, J. D. Lumpe, and E. Shettle, Validation of POAM III Ozone, *Eos Trans. AGU, 82*(47), Fall Meet.

Suppl., Abstract A42A-0092, 2001.

Russell, J. M. III, L. L. Gordley, J. H. Park, S. R. Drayson, D. H. Hesketh, R. J. Cicerone, A. F. Tuck, J. E. Frederick, J. E. Harries, and P. J. Crutzen, The Halogen Occultation Experiment, *J. Geophys. Res., Vol. 98, No. D6*, 10,777-10,797, June 20, 1993.

Savigny, C. von, I. McDade, E. Griffioen, C. Haley, C. McLinden, C. Sioris, E. Llewellyn, and the Odin Team, Ozone Profiles Retrieved From Odin/OSIRIS Observations of Limb-Radiance Spectra, *Eos Trans. AGU, 82*(47), Fall Meet. Suppl., Abstract A42A-0085, 2001.

Schönbein, C. F., Recherches sur la nature de l'odeur qui se manifeste dans certaines actions chimiques, *C. R. Acad. Sci. Paris, 10*, 706, 1840.

Sioris, C. E., C. von Savigny, R. L. Gattinger, J. C. McConnell, I. C. McDade, E. J. Llewellyn, and the Odin Team, Attitude determination for limb-scanning satellites: The "KNEE" at 305 nm, *Eos Trans. AGU, 82*(47), Fall Meet. Suppl., Abstract A32B-0056, 2001.

Siskind, D. E. and J. M. Russell III: Coupling Between Middle and Upper Atmospheric NO: Constraints from HALOE Observations, *Geophys. Res. Lett., Vol. 23, No. 2*, 137-140, 1996.

Solomon, S. C., S. M. Bailey, C. A. Barth, R. L. Davis, J. A. Donnelly, T. E. Holden, M. S. Kelley, R. A. Kohnert, M. T. McGrath, A. W. Merkel, H. L. Reed,

S. M. Ryan, M. A. Salada, S. R. Steg, G. A. Tate, J. C. Westfall, J. J. Westphal, and P. R. Withnell, The SNOE Spacecraft Integration, Test, Launch, Operation, and On-orbit Performance, *Proc. 12th AIAA/USU Conference on Small Satellites,* 1998.

Solomon, S., Stratospheric ozone depletion: A review of concepts and history, *Reviews of Geophysics, 37,* 275-316, 1999.

Stephens, G. L., Remote Sensing of the Lower Atmosphere, *Oxford University Press, New York, Oxford,* 1994.

Stolarski, R. S., and R. J. Cicerone, Stratospheric Chlorine: A Possible Sink for Ozone, *Can. J. Chem., 52,* 1974.

Stolarski, R. S., A. J. Krueger, M. R. Schoeberl, R. D. McPeters, P. A. Newman, and J. C. Alpert, Nimbus-7 satellite measurements of the springtime Antarctic ozone decrease, *Nature, 322,* 808-811, 1986.

Strong, K., B. M. Joseph, R. Dosanjh, I. C. McDade, C. A. McLinden, J. C. McConnell, J. Stegman, D. P. Murtagh, and E. J. Llewellyn, Retrieval of vertical Concentration Profiles from OSIRIS UV-Visible Limb Spectra, *Can. J. Phys, 80,* S1, 2002.

Strutt, R. J., Ultraviolet transparency of the lower atmosphere and its relative poverty in ozone, *Proc. R. Soc., A, 94,* 260-268, 1918.

Suzuki, M., A. Matsuzaki, T. Ishigaki, N. Kimura, N. Araki, T. Yokota, and Y. Sasano, ILAS, the Improved Limb Atmospheric Spectrometer on the Advanced Earth Observing Satellite, *IEICE TRANS. Commun.*, E78-B, 12, 1560-1670, 1995.

Thomason, L., Lower Stratosphere aerosol variability during clean periods, *8th assembly of the International Association of Meteorology and Atmospheric Sciences*, Innsbruck, Austria, July 10-18, 2001.

UNEP, United Nations Environment Programme, Ozone Secretariat, The Montreal Protocol on Substances that Deplete the Ozone Layer, Nairobi, Kenya, Po Box 30552, http://www.unep.org/ozone, 2000.

Wang, P.-H., P. Minnis, M. P. McCormick, G. S. Kent, and K. M. Skeens, A 6-year climatology of cloud occurrence frequency from Stratospheric Aerosol and Gas Experiment II observations, *J. Geophys. Res., 101*, 29407-29429, 1996.

Warneck, P., Chemistry of the natural atmosphere, *International Geophysics Series, Volume 41, Academic Press, San Diego*, 1988.

Warshaw, G. D., D.-L. Desaulniers, and D. Degenstein, Optical design and performance of the Odin UV/visible spectrograph and infrared imager instrument, *Proc. 10th Annual AIAA/USU Conference on Small Satellites*, 1996.

Wayne, R. P., The Photochemistry of Ozone, *Atmosp. Env., 21,* 1683-1694, 1987.

Wayne, R. P., Chemistry of Atmospheres, *Oxford University Press, Oxford*, 1991.